Master Thesis

Installation and Optimisation of a Test Stand for Solid Oxide Fuel Cells and Solid Oxide Electrolyser Cells

Klaus Klamminger

Supervisors

assoc.Prof. Dipl.-Ing. Dr.mont. Edith Bucher

Dipl.-Ing. Dr.mont. Andreas Egger

Chair of Physical Chemistry, Montanuniversitaet Leoben

September 2018

Eidesstattliche Erklärung

Ich erkläre an Eides statt, dass ich die vorliegende Arbeit selbstständig verfasst, andere als die angegebenen Quellen/Hilfsmittel nicht benutzt, und die den benutzten Quellen wörtliche und inhaltlich entnommene Stellen als solche kenntlich gemacht habe.

Statutory Declaration

I declare that I have authored this thesis independently, that I have not used other than the declared sources/resources, and that I have explicitly marked all material which has been quoted either literally or by content from the used sources.

Leoben, 26. Sept. 2018

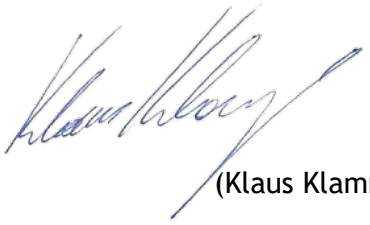

(Klaus Klamminger)

Kurzfassung

Wasserstoff gewinnt als einer der potentiell wichtigsten Energieträger der Zukunft immer mehr an Bedeutung, da er sowohl nachhaltig produziert, als auch emissionsarm zur Energiegewinnung eingesetzt werden kann. Hochtemperaturbrennstoff- bzw. -elektrolysezellen (SOFC bzw. SOEC) stellen hocheffiziente Technologien für die Verstromung bzw. Erzeugung von Wasserstoff dar. Allerdings führen Betriebstemperaturen von 600-850 °C zu Degradationseffekten der eingesetzten Materialien, was im Langzeitbetrieb in einer kontinuierlichen Verschlechterung der Zellperformance resultiert.

Ziel dieser Arbeit sind der Aufbau, die Inbetriebnahme und die Optimierung eines Teststandes für die Untersuchung von SOFC- und SOEC-Knopfzellen. Damit können wertvolle Erkenntnisse über die Eignung von neuartigen Verbindungen als Elektrodenmaterialien erzielt und Studien zur Langzeitstabilität durchgeführt werden, ohne dabei aufwändig hergestellte Zellen im industrierelevanten Maßstab zu benötigen.

Nach dem erfolgreichen Aufbau des experimentellen Setups wurden umfangreiche Vorversuche und Parameterstudien hinsichtlich Gasdichtheit und Temperaturverteilung durchgeführt. Weiters wurden Untersuchungen an neun Knopfzellen durchgeführt, die mithilfe von elektrochemischer Impedanzspektroskopie sowie Strom-Spannungs-Kennlinien, im Speziellen bei unterschiedlichen Feuchtegehalten im Brenngasstrom, charakterisiert wurden. Post-Test-Analysen der Zellen mittels Rasterelektronenmikroskopie und energiedispersiver Röntgenspektroskopie liefern Informationen über die Mikrostruktur und chemische Zusammensetzung der einzelnen Materialschichten, welche als Feedback in die Optimierung des Messaufbaus und die Materialentwicklung eingehen.

Die Ergebnisse zeigen, dass für sämtliche untersuchte Zellen der Polarisationswiderstand mit steigender Temperatur und steigendem Wassergehalt im Brenngasstrom abnimmt, unabhängig vom verwendeten Luftelektrodenmaterial. Zellen mit gemischt ionisch-elektronisch leitenden $La_{1-x}Sr_xCoO_{3-\delta}$ Luftelektroden erzielen aufgrund niedriger flächenspezifischer Widerstände und geringer Degradation die beste Leistung. Mit dem neu entwickelten Luftelektrodenmaterial $La_{0.8}Ca_{0.2}FeO_{3-\delta}$ wird derzeit die Performance von Zellen mit Standardmaterialien ($La_{1-x}Sr_xMnO_{3\pm\delta}$, $La_{1-x}Sr_xCoO_{3-\delta}$) nicht erreicht. Anhand der Ergebnisse der Post-Test-Analysen kann der Betrieb mit hohen Feuchtegehalten im Brennstoffstrom über einen längeren Zeitraum als besonders kritischer Faktor identifiziert werden, welcher zur Delamination und damit zum Versagen der Zellen führen kann.

Abstract

Hydrogen attracts more and more interest, since it is considered as one of the most promising future energy carriers owing to the possibility of its sustainable production as well as its application as fuel for low-emission power generation. Solid oxide fuel and electrolyser cells (SOFC and SOEC) are highly efficient technologies for the conversion and generation of hydrogen, respectively. However, the high operating temperatures of 600-850 °C cause significant degradation effects of the materials used, resulting in a continuous deterioration of cell performance during long-term operation.

The aim of this work is the installation and optimisation of a test stand for the investigation of SOFC and SOEC button cells. With this setup, valuable information about the suitability of novel compounds as electrode materials may be obtained and long-term studies can be performed, without requiring elaborately produced cells with industry-relevant dimensions.

After the successful implementation of the experimental setup, extensive tests and parameter studies were performed, focusing on the gas tightness and temperature distribution at the cell. Further, nine button cells were characterized by means of electrochemical impedance spectroscopy and current-voltage curves, with focus on the influence of different water contents in the fuel feed. Moreover, post-test analyses using scanning electron microscopy and energy-dispersive X-ray spectroscopy give information about the microstructure and chemical composition of the different cell layers, which is used as feedback for optimisation of the test setup and materials development.

The results show that for all investigated cells, the polarisation resistance decreases with increasing temperature and increasing water content in the fuel feed. Cells with air electrodes fabricated from the mixed ionic-electronic conductor $La_{1-x}Sr_xCoO_{3-\delta}$ exhibit the best performance due to small area-specific resistances and low degradation. Cells with the novel air electrode material $La_{0.8}Ca_{0.2}FeO_{3-\delta}$ do currently not achieve the high cell performance observed with standard materials ($La_{1-x}Sr_xMnO_{3\pm\delta}$, $La_{1-x}Sr_xCoO_{3-\delta}$). Based on the results of post-test analyses, operation with high water contents in the fuel feed during an extended period of time, is identified as an especially critical factor, which may lead to delamination and thus to failure of the cells.

Acknowledgements

I would like to take this opportunity to express my gratitude to all persons who made it possible to draw up this master thesis which has been an essential part of my master programme *Industrial Energy Technology*.

At first, I am extremely grateful to my supervisors Edith Bucher and Andreas Egger who always supported me with valuable suggestions and useful contributions to my work. Thank you for your helpful assistance during the laboratory work and for carefully proofreading this thesis.

Special thanks go to Professor Werner Sitte, who made it possible for me to write my master thesis at the Chair of Physical Chemistry at the Montanuniversitaet Leoben.

Moreover, I also wish to thank Christian Berger, Nina Schrödl, Peter Gsaxner, Karin Stanglauer and the rest of the team for your assistance in practical works and your well-founded expertise. All your help cannot be overestimated.

I would also like to extend my sincere thanks to my whole family, who always encouraged me during my studies. I very much appreciate that you made it possible for me to attend university.

Finally, financial support by the Austrian “Klima- und Energiefonds” within the “Energieforschungsprogramm 2015” (project no. 853626, project title SOFC-SALT) is gratefully acknowledged.

Table of Contents

List of Figures

List of Tables

List of Abbreviations

General Abbreviations

ac	alternating current
AFC	alkaline fuel cell
ASC	anode-supported cell
BSE	backscattered electrons
CE	counter electrode
CHP	combined heat and power system
CPE	constant phase element
dc	direct current
DMFC	direct methanol fuel cell
ECM	equivalent circuit model
EDX	energy-dispersive X-ray spectroscopy
EIS	electrochemical impedance spectroscopy
HGL	heated gas line
i.e.	id est
ID	inner diameter
I-U	current-voltage
MCFC	molten carbonate fuel cell
MUL	Montanuniversitaet Leoben
OD	outer diameter
PAFC	phosphoric acid fuel cell
PEMFC	proton exchange membrane fuel cell
RE-	negative reference electrode
RE+	positive reference electrode
RSOC	reversible solid oxide cells
SEM	scanning electron microscopy
SOEC	solid oxide electrolyser cell
SOFC	solid oxide fuel cell
TPB	triple phase boundary
WE	working electrode
XRD	X-ray diffraction

Chemical Formulae

8-YSZ	YSZ with 8 mol% Y_2O_3
Bi_2O_3	bismuth(III) oxide
CeO_2	cerium dioxide, ceria
CGO	gadolinium-doped CeO_2
CO	carbon monoxide
CO_2	carbon dioxide
CO_3^{2-}	carbonate ion
CoO	cobalt oxide
H^+	hydrogen ion
H_2	hydrogen
H_2O	water
$LaMnO_3$	lanthanum manganite
LCF82	$La_{0.8}Ca_{0.2}FeO_{3-\delta}$
LSC	$La_{1-x}Sr_xCoO_{3-\delta}$
LSF	$La_{1-x}Sr_xFeO_{3-\delta}$
LSM	$La_{1-x}Sr_xMnO_{3\pm\delta}$
N_2	nitrogen
Ni/YSZ	cermet consisting of nickel and YSZ
NiO	nickel oxide
O_2	oxygen
O^{2-}	oxide ion
OH^-	hydroxide ion
PEEK	polyether ether ketone
SDC	samarium-doped ceria
Y_2O_3	yttrium oxide, yttria
YSZ	yttria stabilised zirconia
Zr^{4+}	zirconium ion
ZrO_2	zirconium dioxide, zirconia

Formula symbols and units

°C	degree Celsius
µm	micrometer
A	Ampere
Å	Ångström
ASR	area-specific resistance
C	Coulomb
e^-	electron
E^0	EMF at standard pressure
EMF	electromotive force
F	Faraday constant (96485 C mol^{-1})
g	gram
h	hour
Hz	Hertz
J	Joule
K	Kelvin
L	inductance
min	minutes
ml_n	millilitre at standard conditions
mol%	mole percent
N	Avogadro constant (6.022×10^{23} mol^{-1})
OCV	open circuit voltage
p_x	partial pressure of x
R	universal gas constant (8.314 J mol^{-1} K^{-1})
R_p	polarisation resistance
R_s	series resistance
S	Siemens
V	Volt
vol%	volume percent
V_{th}	thermoneutral voltage
W	Watt
Z	impedance
ΔG	Gibbs free energy
ΔG_r	Gibbs free energy of reaction
Ω	Ohm

1 Motivation

Today, our global society has to face serious man-made ecological challenges in order to preserve a liveable environment for future generations. Growing problems with polluted air and a global warming caused by a constantly increasing carbon footprint of mankind, make the decarbonisation of our energy systems one of the most necessary issues to curb the non-deniable climate change. In order to solve this problem, the Paris agreement on climate change was signed by 195 nations in 2015 with the main objective to keep the global temperature rise below 2 °C above the pre-industrial age. The agreement includes, inter alia, the funding of enhanced green technologies which play an essential role in the reduction of the greenhouse gases emitted [1].

Lowering the CO_2 emission levels is one step towards a sustainable energy revolution. Substituting fossil fuels with hydrogen is a promising approach if it is produced from renewable resources such as hydropower, wind energy or photovoltaic systems. One way to effectively use the energy content in the hydrogen is the fuel cell, which is widely considered as a key technology in carbon-free energy systems because of its possible application in future propulsion systems and further increasing distributed on-site power generation. Another advantage of hydrogen is that it can be utilised as storage medium for the fluctuating electricity production of renewable energies. But there are still technical challenges for hydrogen-based applications, which need to be solved in order to become a mature technology. Compared to fossil energies, the environmentally compatible production of hydrogen is too cost-intensive to be competitive. Storage difficulties still pose a problem as well. Moreover, the costs of fuel cell systems must be cut to get fully established in the field of energy [2].

The benefit of continuous power generation without emitting any other substances than water, make fuel cells an attractive alternative to combustion engines. Especially high-temperature fuel cells such as the solid oxide fuel cell (SOFC) are in the focus of interest as they can be used in cogeneration systems, which simultaneously generate heat and electricity [2]. The high operating temperatures, which are required to achieve sufficient ionic conductivity of the ceramic electrolyte, lead to the need of sophisticated materials able to withstand the high material stresses prevailing during operation for a long time. Although major advances have been made in the last years, further improvements must be delivered until commercialisation can take place [3].

1.1 Research topic and definition of objectives

The research at the Chair of Physical Chemistry (LPC) at the Montanuniversitaet Leoben focuses on the material properties of new SOFC and SOEC air electrode materials, particularly with regard to the charge and mass transport mechanisms of ceramics. The manufacturing process of these electrode materials is complex and time-consuming. In order to reduce the amount of material needed, small button cells with a diameter of 20 mm are useful for first investigations of full cells at real operating conditions.

The aim of this thesis is the installation, start-up, and optimisation of a measurement setup for the electrochemical characterisation of button cells, with special focus on the influence of different humidity levels in the fuel feed. A variety of cell tests should be performed, including tests with commercially available state-of-the-art materials, as well as with novel materials manufactured in-house. The task involves measurements applying electrochemical impedance spectroscopy and current-voltage characteristics, as well as the analysis of the test results based on preliminary considerations (gas-tightness, temperature control). A further objective is the post-test analysis of the button cells by means of XRD and SEM, including sample preparation.

2 Theoretical background

The use of fuel cells enables an efficient and largely pollution-free generation of energy. A fuel, such as hydrogen, flows continuously into the cell where an electrochemical reaction with an oxidant, such as oxygen, takes place. In comparison to conventional energy systems, where first of all heat is generated from the chemical energy of a combustible, fuel cells convert the exergy of a fuel directly into electrical energy. Since fuel cells are therefore not limited by the Carnot efficiency, this technology is very attractive, especially for decentralised energy systems [4].

The rates of the chemical reactions within a fuel cell are determined by the corresponding activation energies and can be accelerated either by catalysts or higher operating temperatures. Moreover, the microstructure and the specific surface area of the electrodes have a huge impact on the performance of the cell. As an increased surface area of the electrode leads to a higher overall flow of ions and electrons, large surface areas are in practice achieved by highly porous electrode microstructures. Until now, a remarkable number of different fuel cell types has been developed, which are optimised for different operating conditions [5].

A common way to classify fuel cells is the electrolyte employed in the system. The most commonly applied type is the proton exchange membrane fuel cell (PEMFC) which consists of a polymeric solid electrolyte with mobile protons. Highly developed materials are necessary due to the low operating temperatures (less than 100 °C) causing slow reaction rates. Expensive platinum is the state-of-the-art catalyst utilised in PEMFC, but technical advances could already reduce the required amount of the precious metal. The PEMFC operates with pure H_2 as fuel, but it can be replaced by methanol which is, unlike hydrogen, easily available. Such types of cells are called direct methanol fuel cells (DMFC) and are also operated at temperatures below 90 °C. As methanol can be conveniently stored in a small tank, portable electronic devices are a huge possible market for DMFC, although these cells supply very low power [5].

The first commercially produced cell type was the phosphoric acid fuel cell (PAFC). The mobile ion is H^+, as well as in PEMFC and DMFC systems. The PAFC consists of an electrolyte of phosphoric acid integrated in a silicon carbide matrix and electrodes made of platinum-coated carbon paper. Typical temperatures of 200°C in combination with Pt-catalysts are applied to run the reaction spontaneously. Due to the relatively high operating temperature, the utilization of waste heat is a benefit of this cell type. Recognised disadvantages are the mediocre electrolyte conductivity and the limited durability of the electrodes due to platinum sintering and coal burn-up [6,7].

Another promising technology is the alkaline fuel cell (AFC), where the highest cell voltage at pure gas conditions of all fuel cell types can be obtained. The AFC is moderate in price and operates at temperatures below 100°C. Their main problem is its intolerance against

carbon dioxide, which clogs the porous electrode owing to the formation of potassium carbonate [7].

Apart from these low-temperature fuel cells, two main varieties of high-temperature fuel cells operating up to 1000°C have to be mentioned. The molten carbonate fuel cell (MCFC) uses an eutectic molten carbonate as electrolyte, which allows carbonate ions (CO_3^{2-}) to pass from the cathode to the anode. For the formation of the carbonate ions, CO_2 is additionally needed at the air cathode. The cell is typically operated at 650°C with the beneficial possibility of using the waste heat at a higher temperature level than the PAFC. In contrast to the PEMFC, CO does not block the surface of the electrodes, because carbon monoxide can be oxidised by atomic oxygen. Owing to a low power density and high specific weight, the MCFC is not suitable for mobile applications. Technically feasible is the utilisation in small cogeneration units [6].

This thesis follows up with the last of the six most promising fuel cell systems which is the solid oxide fuel cell (SOFC). A detailed description of this type of fuel cell is given in the next chapter. Table 1 gives an overview of the most important fuel cell types.

Table 1: Basic data of the most important fuel cells [5].

Fuel cell type	Mobile ion	Operating temperature	Applications
PEMFC	H^+	30-100°C	Vehicles and mobile applications, low power CHP
DMFC	H^+	20-90°C	Portable electronic devices of low power
PAFC	H^+	~220°C	Large number of 200-kW CHP systems in use
AFC	OH^-	50-200°C	Used in space vehicles
MCFC	CO_3^{2-}	~650°C	Medium-to large-scale CHP
SOFC	O^{2-}	500-1000°C	All sizes of CHP systems

2.1 Solid oxide fuel cells (SOFC)

The fuel cell type that operates at the highest temperatures is the SOFC. At temperature levels up to 1000 °C, it supports various types of fuels such as hydrogen, carbon monoxide and hydrocarbons. Furthermore, it allows a good conversion of the fuel without using expensive catalysts, due to higher reaction rates at elevated temperatures. As already mentioned in the context of the MCFC, high-temperature fuel cells are capable of using a remarkable amount of the exhaust heat of the system. Especially SOFCs can be employed in combined heat and power systems (CHP) achieving high overall efficiencies. The basic

concept of the SOFC is simple, because when compared to other fuel cell types, all involved substances and materials are in solid or gaseous state [8].

2.1.1 Operating Principle

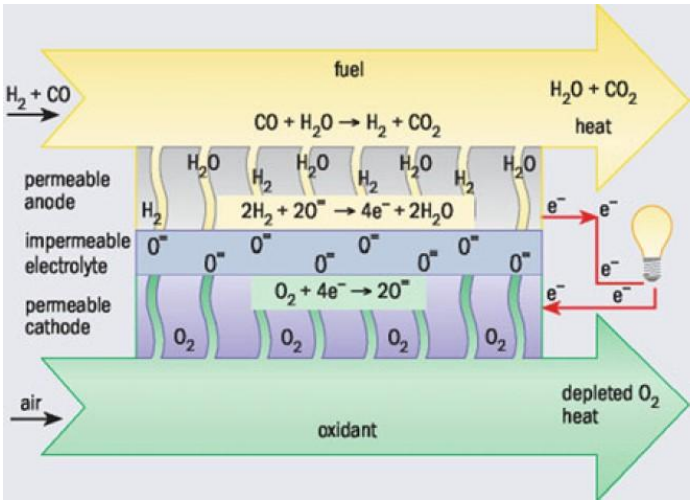

Figure 1: Operating principle of a solid oxide fuel cell [8].

A typical SOFC consists of three main parts: the anode on the fuel side, the cathode on the air side and the dense electrolyte. As it can be seen in Figure 1, air and fuel streams are continually entering a channel separately on each side of the electrolyte. Oxygen molecules diffuse through the porous cathode to the gas-tight electrolyte, reacting with electrons, which are conducted via an external circuit from the anode, to oxide ions O^{2-}. As the electrolyte is permeable for these oxide ions, they can pass through it towards the anode side where the fuel, which diffuses through the anode layer, is oxidised at the electrolyte and anode interface. The reaction products are water vapour and electrons if hydrogen is used as fuel, and additionally carbon dioxide if CO or hydrocarbons are supplied to the cell. The formed electrons leave the anode generating an electric current [8].

The following electrochemical reactions with the fuel H_2 can be expressed [9]:

$$\text{Anode:} \quad H_2 + O^{2-} \rightarrow H_2O + 2e^- \tag{1}$$

$$\text{Cathode:} \quad \frac{1}{2}O_2 + 2e^- \rightarrow O^{2-} \tag{2}$$

$$\text{Overall:} \quad H_2 + \frac{1}{2}O_2 \rightarrow H_2O \tag{3}$$

As it can be seen in the chemical equations, for one mole of hydrogen reacted, 2N electrons are released to the external circuit, where N is the Avogadro constant.

Considering that the charge of one electron is -e, the total charge flow results as:

$$-2\mathrm{Ne} \rightarrow -2\mathrm{F} \tag{4}$$

F is the Faraday constant, which represents the absolute value of the electric charge per mole of electrons. The electrical work done can be obtained by multiplying this charge with the voltage E of the fuel cell. Assuming that the system has no losses (reversible system), the electrical work done equals the Gibbs free energy ΔG_r:

$$\Delta G_r = -2F \times E \tag{5}$$

Dividing by -2F gives an equation for the electromotive force (EMF) of the SOFC:

$$E = \frac{-\Delta G_r}{2F} \tag{6}$$

For ideal conditions, this value is 1.23 V at 25°C, which is the maximum theoretical cell voltage. It has to be taken into account that the Gibbs free energy of reaction changes with temperature and state of the product water. Moreover, there is an important effect of pressure and gas concentration on ΔG_r. Since SOFCs operate at high temperatures it can be assumed that the water vapour (product of equation 3) acts as an ideal gas. Thus equation 6 can be extended by adding a term depending on the partial pressures $p_{r,p}$ of reactants and products:

$$E = E^0 + \frac{RT}{2F} ln\left(\frac{p_{H_2} \times p_{O_2}^{\frac{1}{2}}}{p_{H_2O}}\right) \tag{7}$$

Equation 7 is a simplified version of the Nernst equation where E^0 is the EMF at standard pressure and R is the universal gas constant. It can be seen that the cell voltage increases with higher partial pressures of hydrogen and oxygen [5].

Figure 2 contrasts the real behaviour of the cell voltage with the ideal performance. Theoretically, the voltage remains constant with increasing current density if all losses are neglected. In real performances, it is found that the voltage is less than the value determined from equation 7, owing to irreversible losses in the system. Furthermore, the temperature influences the curve shape, as the cell shows more linear behaviour at higher temperatures. There are four principal factors that influence the decrease of the voltage with increasing current densities: fuel cross-over, activation polarisation, ohmic losses and concentration polarisation. The total voltage drop always results as the sum of these four losses [10].

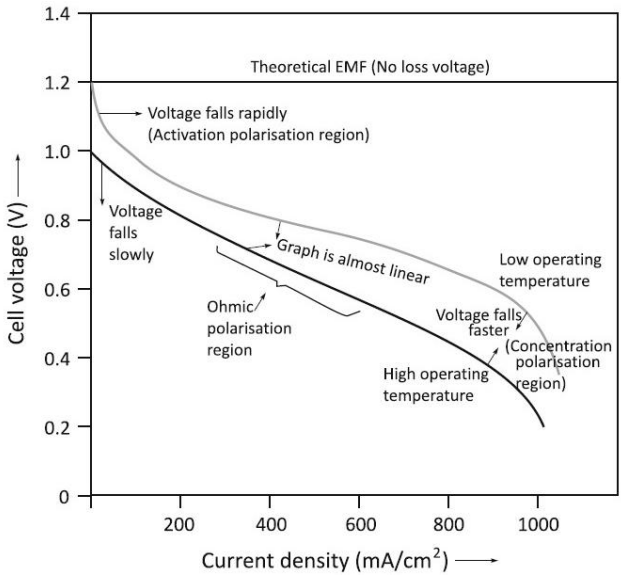

Figure 2: Characteristic voltage drop with increasing current density [10].

The fuel cross-over effect considers that the electrolyte is not completely impermeable for fuel molecules, so that a small amount of fuel diffuses from the anode to the cathode. As a consequence, direct reaction with oxygen will take place without generating electrons that can pass via the external electric circuit [5].

Activation losses predominate at low current densities and are responsible for the voltage drop primarily at the cathode. Due to slow electrode kinetics, including adsorption of oxygen molecules, dissociation, diffusion of the oxygen atoms to the triple phase boundary and formation of oxide ions, this is a limiting process for the electrochemical reaction [11]. The Tafel-equation or the more accurate Butler-Volmer equation can be applied to give a description of this process. Here, the exponential relationship between current density and overvoltage is expressed. The strong nonlinear influence on the working voltage can be traced back to the fact that reaction rates are very low at small current densities. There are not sufficient charge carriers available in order to uphold the current density, thus the cell voltage strongly decreases. Activation polarisation is especially present in low- and medium-temperature fuel cells [5,10].

Resistances of the electrolyte, electrodes and contacts mainly cause the ohmic losses in a fuel cell. A linear relationship depending on conductivity and geometrical data between voltage drop and current density is given in Ohm's law:

$$\Delta U_{Ohm} = \left(\rho_{electrolyte} * l_{electrolyte} + \rho_{anode} * l_{anode} + \rho_{cathode} * l_{cathode} + R_{contact}\right) * i \qquad (8)$$

where ρ is the specific resistance and l is the thickness of the respective components. The ionic resistance of the electrolyte is by far bigger than those of the electrodes, hence the resistive losses are mainly caused by the electrolyte. As a consequence, ΔU_{Ohm} has the highest impact on the cell performance in electrolyte supported cell types [12]. In case degradation takes place at the electrodes, the ohmic losses can change owing to the

formation of secondary compounds as a result of the reaction between adjacent cell components [11].

One of the most important parameters with respect to fuel cells is the area-specific resistance (ASR), which represents the internal areal resistance of the fuel cell. It is usually specified in Ωcm^2 since the electrical resistance is inversely proportional to the cross-section of the cell, and to allow comparison with the ASR of other cells or cell types. A simple way to obtain the ASR of a fuel cell is to determine the relation between overvoltage and current density in the operating point:

$$ASR = \frac{EMF - V}{i} \tag{9}$$

denoting EMF the reversible cell voltage at equilibrium and V the actual voltage at a certain current density i. As the achieved result for the ASR strongly depends on the current density applied for the calculation, it should always be specified which current density was utilised for the calculation of the ASR [11].

The migration of the educts (O_2 and H_2) through the porous electrodes to the triple-phase-boundary cannot progress at infinite rates. Likewise, on the anode side the removal of water requires time. This transport is proportional to the current that flows in the cell. The growing demand of educts at increasing current densities is no longer satisfied. Thus, the partial pressure at the TPB decreases and results in a depletion of educts and an accumulation of products, respectively. According to the Nernst equation, a variation of the partial pressures of the chemical species involved can lead to lower voltages, which decreases cell performance. This kind of loss is known as concentration polarisation and is mainly a function of the diffusivity of the gases, electrode microstructures, partial pressure and current density. Furthermore, if the electrode consists of a material with very small pore sizes, Knudsen and surface diffusion as well as adsorption/desorption processes can occur. In general, the concentration losses largely derive from the cathode for two reasons: Owing to the low molecular weight of hydrogen, the binary diffusivity of H_2 in H_2O is more than four times higher than that of O_2 in N_2. Moreover, the partial pressure of hydrogen in a fuel on the anode side usually exceeds the partial pressure of oxygen in the oxidant on the cathode side. For this reason, the current density is mainly limited by the cathode, wherefore the thickness of the cathode in cathode-supported systems can limit the overall cell performance. If pure hydrogen is used as fuel, anode-supported cells can be produced comparatively thick, without enhancing concentration polarisation, which is one of the main advantages of this cell configuration [12].

2.1.2 Fuel cell efficiency

The fuel cell efficiency is a meaningful and significant quantity to assess a fuel cell system. The overall fuel cell efficiency comprises mainly three parts, which are briefly explained in this chapter.

Since the electrical work done equals the Gibbs free energy ΔG, which can be described as the useful output of the chemical reaction, the thermodynamic efficiency η_{th} can be calculated with:

$$\eta_{th} = \frac{\Delta G}{\Delta H} \tag{10}$$

It is important to note that the product water can be either in liquid or gaseous state, hence ΔH is the higher heating value (HHV) or the lower heating value (LHV), respectively. For reaction (3), $|\Delta G|$ decreases and $|\Delta H|$ increases with rising temperatures, thus the thermodynamic efficiency declines when operating fuel cells at higher temperatures [13].

As already mentioned in the previous chapter, due to the polarisation losses, the voltage V measured in real fuel cells under load is always less than the voltage achieved at a current density of zero, the OCV. This voltage drop is considered in the voltage efficiency:

$$\eta_V = \frac{\mathrm{V}}{OCV} \tag{11}$$

A small amount of the fuel supplied to the fuel cell is not converted and leaves the cell without being oxidised. If no further steps, such as fuel recirculation, recovery or post-combustion of the unreacted fuel to preheat the inlet air, are taken, the fuel utilisation is given by:

$$u_F = \frac{\dot{\mathrm{n}}_{fuel,in} - \dot{n}_{fuel,out}}{\dot{n}_{fuel,in}} = 1 - \frac{\dot{n}_{fuel,out}}{\dot{n}_{fuel,in}} \tag{12}$$

with ṅ being the fuel flow per unit time. The determination of the unreacted fuel flow is quite difficult. Alternatively, it is possible to obtain u_F by the ratio of the actual current I and the maximum current, which can be gained from the number of electrons N, that are released from one fuel molecule and the Faraday constant F:

$$u_F = \frac{\mathrm{I}}{N * F * \dot{n}_{fuel,in}} \tag{13}$$

Neglecting the electronic current flow through the electrolyte, the overall fuel cell efficiency η_{FC} can be calculated by multiplying the mentioned partial efficiencies:

$$\eta_{FC} = \eta_{th} * \eta_V * u_F \tag{14}$$

Assuming that η_{th} and u_F are basically well defined, it can be seen that the overall efficiency depends primarily on the voltage efficiency η_V and thus on the attained voltage in the operating fuel cell. This aspect highlights the importance of minimizing the polarisation losses by applying materials that cause low overvoltages [13].

2.2 Solid oxide electrolyser cell (SOEC)

Water electrolysis is supposed to be one of the key factors in low-carbon sustainable energy systems in future scenarios. Since the power generation became more fluctuating in the recent years due to an increasing supply of renewables, the development of efficient energy storage systems came to the fore in order to balance electricity demand and production. Promising technologies like Power-to-Gas can use surplus electricity via the co-electrolysis of water and CO_2, subsequently converting the products hydrogen and CO into a storable gas like CH_4. The approach of integrating gas storages with renewably produced gases is considered to be the most cost-efficient concept for the indispensable inter-seasonal energy storage in our energy systems [14].

Solid oxide electrolyser cells are one possible technology to perform water electrolysis with higher efficiency than the already commercialised low temperature electrolysers such as alkaline and PEM systems. The structure of SOEC cells is similar to SOFC cells but they run in reverse operation, meaning that steam is supplied to the fuel electrode (SOEC cathode) which receives electrons from an external electricity source forming hydrogen (H_2) and oxide ions (O^{2-}). These oxide ions can pass through the electrolyte to the air electrode (SOEC anode) where the oxide ions react to oxygen molecules (O_2) releasing the electrons again [15]. Figure 3 illustrates the basic operational processes of a SOEC cell supplied with pure water vapour.

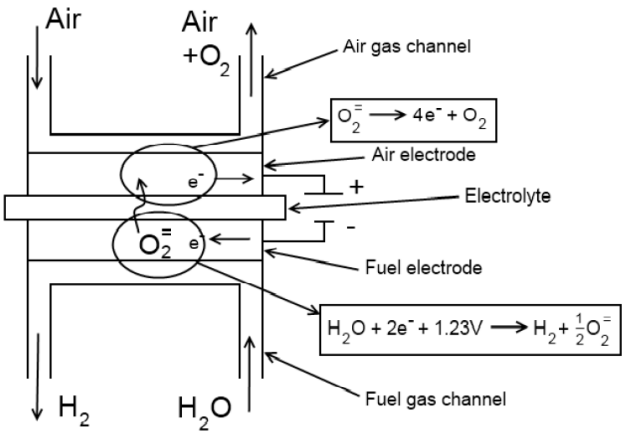

Figure 3: Operating principle of a solid oxide electrolyser cell with pure steam as a reactant on the fuel side [16].

An important parameter with respect to SOEC operation is the thermoneutral voltage V_{th}, which represents the operating voltage with equal inlet and outlet temperatures and thus no heat flow to or from the cell. It can be calculated using the following equation:

$$V_{th} = \frac{\Delta H}{nF} \tag{15}$$

denoting ΔH as the reaction enthalpy, n the number of electrons and F the Faraday constant. At this voltage, which is 1.287 V at 800 °C [17], the lowest local temperature differences and the minimal mechanical strains occur. Running steam electrolysis needs a lot of energy, in particular when compared to the heat capacities of the educts and products. For this reason, the adiabatic temperature strongly increases or decreases if the cell is operated at higher or lower voltages V_{op}, respectively. The efficiency η of a SOEC can be expressed with:

$$\eta = \frac{LHV}{W} = \frac{V_{th}}{V_{op}} \tag{16}$$

with LHV being the lower heating value of the product fuel and W the electrical energy input. It can be seen that an efficiency of 100% can be achieved if the cell is operated at the thermoneutral voltage, but in real operation it will be lower, owing to gas leakages, heat losses and non-perfect electronic insulation of the electrolyte [15].

SOEC systems can not only be supplied with pure H_2O but also with a gas mixture of steam and CO_2 in order to produce synthesis gas which consists of CO and H_2. This process is known as co-electrolysis. A particular advantage of co-electrolysis is that the reaction products (CO, H_2) can be converted into liquid hydrocarbons via the Fischer-Tropsch process which can be stored easily compared to hydrogen. Furthermore, it is a sustainable and environmentally friendly process, if CO_2 is captured from the ambient air [18], as it is depicted in Figure 4. Usually, the reaction heat from the exothermal Fischer-Tropsch process covers the energy demand needed for the SOEC steam production. These conditions allow to strongly harness the synergies between the SOEC system and the conversion of the resulting synthesis gas into liquid fuels.

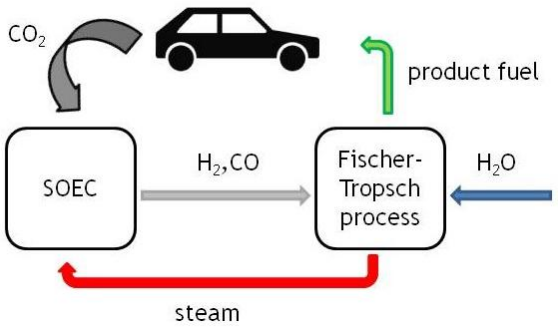

Figure 4: Possible combination of a SOEC system with downstream liquid fuel production and CO_2 capture.

It is also possible to operate so-called reversible solid oxide cells (RSOC) alternatively in SOFC or SOEC mode. This concept has received much attention in recent times due to the fact that either energy storage or energy production can be performed with high flexibility and with the use of only one device. But there are still some questions, for instance about the optimal fuel for such systems, the round trip efficiency, and enhanced degradation problems [15].

2.3 Materials for SOFC/SOEC

The high future potential of SOFC/SOEC systems with respect to green and sustainable energy technology is undisputed. The benefit of combining heat and power generation at high operation temperatures makes the SOFC a promising candidate to fulfil future needs in the field of energy supply. These high temperatures lead to higher material requirements for SOFCs than for low temperature fuel cell systems. One way to classify SOFC systems is by the type of electrolyte used. In the experimental part in chapter 4, only anode-supported planar cells with ZrO_2-based electrolytes are tested. This well-engineered system is the most advanced one of all systems developed in the history of solid oxide fuel cells [3]. The discussion below focuses on the materials used in the experimental investigations in the course of this thesis.

2.3.1 Electrolyte

The electrolyte acts as an electronic insulator between the two electrodes and is only conductive for oxide ions at elevated temperatures. Compounds with fluorite structure, which exhibit deficiency in oxygen, are well known materials for fast oxide-ion conduction. Besides CeO_2- and Bi_2O_3-based materials, compounds based on zirconium dioxide (ZrO_2) are the most prominent. For good ionic conduction the lattice structure must be cubic, which is the case for pure ZrO_2 only above 2370 °C. For this reason, Zr must be substituted by divalent or trivalent cations of alkaline-earth elements (Ca, Mg, Sr) or rare-earth elements (Sc, Y), which provoke oxygen vacancies in the Zr^{4+} lattice. According to the principle of charge compensation, this is a crucial factor for high O^{2-} conductivity [3].

Yttria stabilised zirconium oxide (YSZ) is the most commonly used material for SOFC electrolytes. Even though Figure 5 shows that the conductivity of YSZ is lower than for other electrolyte materials (gadolinium-doped CeO_2 (CGO), $(La,Sr)(Mg,Ga)O_3$), YSZ is the only compound that provides sufficient long-term stability under operating conditions for fuel cells [19]. The conductivity of YSZ increases with higher yttrium oxide (Y_2O_3) contents up to a maximum conductivity at 8 mol% dopant level [20], thus 8-YSZ is the electrolyte used in all performed button cell tests in chapter 4.

The electrolyte makes up approximately one half of the ohmic losses in a fuel cell, thus it is important to minimise the thickness of the YSZ layer in order to reduce the ASR of the cell. But as increasing oxygen leakage at thinner electrolyte layers decreases the electrolyte efficiency, there is an optimal thickness for every material at any temperature. For instance at 700 °C, the optimal YSZ layer thickness is 10 µm [12].

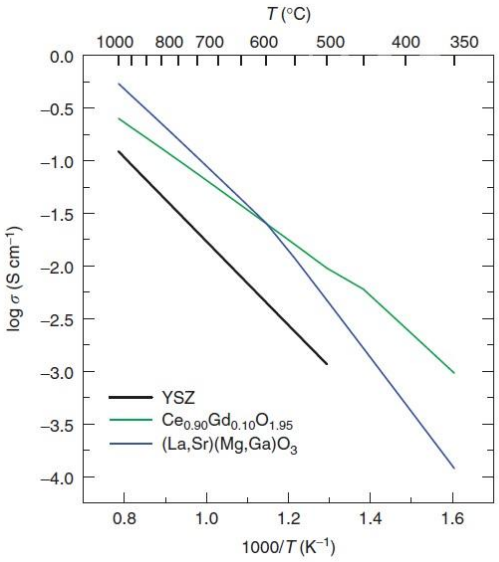

Figure 5: Conductivity of SOFC electrolytes as a function of temperature [19].

2.3.2 Fuel electrode

At the fuel electrode, fuel components are electrochemically oxidised in SOFC operation. The oxidation takes place at the triple phase boundary (TPB) which is the contact zone between electrode, electrolyte and a gaseous fuel [21]. In SOEC operation, the supplied H_2O is reduced at the TPB of the fuel electrode to H_2 forming oxide ions O^{2-} which can pass through the electrolyte to the air electrode. In order to quickly run the reaction, the electrode material must exhibit high catalytic activity for hydrogen oxidation, which decreases polarisation losses at the SOFC anode. Moreover, the SOFC anode polarisation is affected by the microstructure and the morphology of the material. Also important is a low mismatch of the thermal expansion coefficient in order to avoid high mechanical stresses at the interfaces which can cause cracks and in the worst case fatal damages [21].

In all performed tests within this thesis (see chapter 4), the anode support consists of a Ni/YSZ cermet which is the most commonly used material for the fuel electrode [22–24]. In this composite, the presence of YSZ leads to the formation of a highly porous ceramic network which provides an enlarged reaction zone and enables the mechanical stability of the entire fuel cell. By contrast, the Ni particles are consistently distributed over the whole ceramic network as they act as catalysts for the electrochemical oxidation of H_2 in SOFC mode [23]. Using Kröger-Vink notation, the oxidation reaction can be written as [24]:

$$H_2 + O^{x}_{O,YSZ} \rightarrow H_2O + 2e' + V^{\bullet\bullet}_{O,YSZ} \tag{17}$$

denoting $O^{x}_{O,YSZ}$ the oxygen ion in the YSZ lattice site and $V^{\bullet\bullet}_{O,YSZ}$ the oxygen vacancy in the YSZ electrolyte.

The YSZ addition reduces the thermal expansion coefficient of the cermet in comparison to pure Ni, which makes the fuel electrode thermally compatible with the electrolyte. Usually Ni/8-YSZ cermets consist of 40-50 vol% Ni and 50-60 vol% 8-YSZ, whereby the electrical

conductivity rises with increasing Ni content. Further important parameters for the performance of Ni/YSZ anodes are the particle size distribution of the starting powder with subsequent coarsening treatment, sintering temperature and degradation [24].

2.3.3 Air electrode

Oxygen reduction in a fuel cell takes place at the SOFC cathode, which is also known as air electrode. Here, the electrode has to be highly electronic conductive in order transport the electrons coming from an external circuit to the TPB and it needs to exhibit good catalytic activity for the reduction of the supplied oxygen. Furthermore, the SOFC cathode must facilitate the transportation of the generated oxide ions into the bulk of the electrolyte. Applying Kröger-Vink notation, the reaction at the fuel electrode can be written [19]:

$$\frac{1}{2}O_2 + 2e' + V_{O,YSZ}^{\bullet\bullet} \rightarrow O_{O,YSZ}^{x} \tag{18}$$

Among other properties, mechanical and chemical stability at elevated temperatures, non-reactivity with the electrolyte and interconnects, high electronic conductivity, good catalytic activity for the oxygen reduction and compatible thermal expansion coefficients with the electrolyte are essential requirements for air electrodes. Oxides with the perovskite structure ABO_3 are the state-of-the-art materials which best meet the former noted requirements for air electrodes [19]. The composition of the perovskite can be modified by substituting A or B-site cations in the lattice in order to improve certain properties of the material. This allows the creation of a variety of compounds which are potential materials for SOFC cathodes [25]. The cubic ABO_3 perovskite structure is illustrated for $La_{1-x}Sr_xMnO_3$ (LSM) in Figure 6.

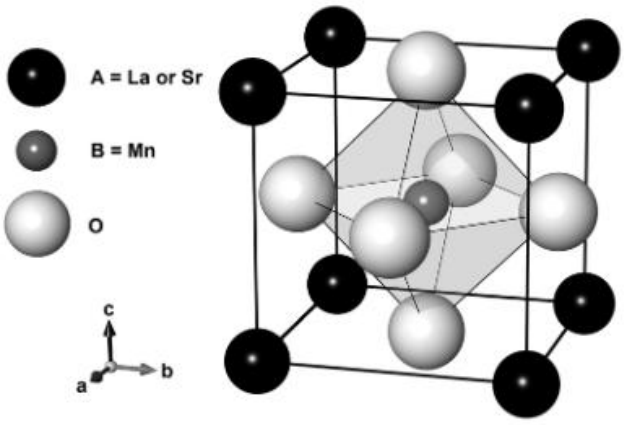

Figure 6: Cubic perovskite structure of $La_{1-x}Sr_xMnO_3$ [26].

In the following, three air electrode materials (LSM, LSC, LCF82) used in the button cell tests described in chapter 4 are further elucidated.

2.3.3.1 $La_{1-x}Sr_xMnO_{3\pm\delta}$ (LSM)

Oxides based on lanthanum manganite ($LaMnO_3$) exhibit poor electronic and ionic transport properties. Therefore, strontium (Sr) is often used as dopant as the electronic conductivity rises with increasing Sr concentration, and the oxygen nonstoichiometry (ionic charge compensation) leads to higher ionic conductivity [27].

At elevated temperatures, LSM has been the material of choice for many years owing to its good electronic conductivity of 200-300 S/cm at 900 °C. But as the trend in the field of SOFC is towards lower operating temperatures, the application of LSM as air electrode is limited due to its comparatively low ionic conductivity (10^{-7} S/cm at 900°C) and poor electrocatalytic activity. In order to be competitive to mixed ionic-electronic conductors, LSM is utilised in composite materials with a second phase which exhibits higher ionic conductivity [25]. LSM/CGO composites are promising SOFC cathode materials, which exhibit higher ionic conductivity due to the presence of CGO particles, and still show sufficient electronic conductivity. However, it has to be considered that the electrical conductivity decreases with increasing CGO content in the composite since the electronic conductivity of LSM forms the mayor part of the total electrical conductivity of the material [28,29].

2.3.3.2 $La_{1-x}Sr_xCoO_{3-\delta}$ (LSC)

Lanthanum cobaltates and in particular $La_{1-x}Sr_xCoO_{3-\delta}$ (LSC) are well studied materials for SOFC air electrodes. Due to the fact that it demonstrates high conductivity for O^{2-} ions and good electronic conductivity, LSC represents an important mixed ionic-electronic conductor. One disadvantage of LSC is the formation zirconates if YSZ is used as electrolyte, which results in low conductivity especially at the electrode-electrolyte interface. However, compared to LSM, LSC exhibits outstanding performance with ceria-based electrolytes such as CGO [30].

In order to prevent the formation of insulating phases, the use of a thin diffusion barrier layer of CGO is a possible, but not unproblematic, solution since solid-state reactions between YSZ and CGO can lead to the formation of phases with lower ionic conductivity as well, and thus lead to a higher ohmic resistance of the cell. As diffusion processes between YSZ and CGO take place at elevated temperatures above 1000 °C, interactions between these two layers can be avoided by the use of low-temperature techniques for the manufacturing processes of the fuel cell [31].

2.3.3.3 $La_{0.8}Ca_{0.2}FeO_{3-\delta}$ (LCF82)

Another novel material that seems to be eligible for the use as air electrode in SOFC and SOEC systems is $La_{0.8}Ca_{0.2}FeO_{3-\delta}$ (LCF82) which is a modification of the well-known $La_{1-x}Sr_xFeO_{3-\delta}$ (LSF) compounds. The idea behind the substitution of Sr with Ca is to reduce the mismatch of the ionic radii of the ions at position A in the ABO_3 perovskite lattice. For La^{3+} the ionic radius is 1.36 Å while it is larger for Sr^{2+} (1.44 Å) and smaller for Ca^{2+}

(1.34 Å) [32]. Due to its larger ionic radius, Sr^{2+} tends to segregate at the grain boundaries where it can react with contaminants in gaseous phase to secondary phases which impedes the reduction of oxygen. In contrast, the ionic radius of Ca^{2+} is closer to the one of La^{3+} which should result in alleviated segregation effects [33].

Characterisation of LCF82 was performed by Berger et al. [33] regarding its material properties. This investigation attests the suitability of LCF82 as electrode material since its kinetic parameters such as the chemical surface exchange coefficients and the chemical diffusion coefficients of oxygen are even higher than those of LSC. The electronic, and more particularly the ionic conductivity of LCF82, are sufficiently high to be considered as air electrode material in SOFC and SOEC systems, respectively. Moreover, the thermal expansion coefficients of LCF82 and the standard electrolyte material are in the same range [33].

2.4 Electrochemical impedance spectroscopy (EIS)

I-U characteristics can represent the influence of polarisation losses on the voltage drop of a fuel cell and enable determining the overall resistance and thus the overall losses of the system. In order to attribute the polarisation mechanisms to the different components of a cell, electrochemical impedance spectroscopy is the method of choice. It plays a fundamental role in the field of characterisation of electrochemical systems such as galvanic- or electrolysis cells because various processes, such as mass-transfer, oxygen reduction kinetic and resistance losses, can be identified [34].

EIS is based on the fact that the individual loss mechanisms occur at different frequencies with time constants deviating from each other. If an ac voltage $u(t) = U * sin\ (\omega t)$ (or current) is applied to the cell, an ac current $i(t) = I * sin\ (\omega t + \varphi)$ (or voltage) response can be measured, denoting φ as the phase shift between $i(t)$ and $u(t)$ and U and I as the amplitudes of voltage and current, respectively. The ac impedance $Z(\omega)$ can now be defined as [35]:

$$Z(\omega) = \frac{u(t)}{i(t)} \tag{19}$$

As it is a complex quantity, the impedance consists of a real part $Z'(\omega)$, known as resistance, and the imaginary part $Z''(\omega)$, the reactance.

$$Z(\omega) = Z'(\omega) + Z''(\omega) \cdot j \tag{20}$$

The plot of $Z''(\omega)$ versus $Z'(\omega)$ is known as the Nyquist or Cole-Cole plot. Since there is no information about the corresponding frequency in these kinds of diagrams, it is common to additionally present the measured data in a Bode plot. Here the frequency is displayed logarithmically on the abscissa whereas the modulus of the impedance $|Z(\omega)|$ and the phase-shift φ are both plotted on the ordinate. A frequency range of 10 mHz to 1 MHz is normally selected, whereby the high frequencies can give information about the

electrolyte resistance. The results obtained at low frequencies comply with the gradient of the I-U curve. The polarisation resistance R_P corresponds to the x-axis intercept between the impedance values at low and high frequencies and comprises all losses caused by polarisation-related mechanisms [36,37]. The broad range permits a concurrent analysis of various processes, for instance diffusion, reaction kinetics or adsorption [34].

In order to achieve truthful results, EIS measurements should be performed in the linear response regime of the system. In the SOFC, processes such as mass-transfer, electrochemical reactions and interfacial responses usually exhibit nonlinear behaviour [34]. To make EIS analysis of SOFC possible, the amplitude U of the applied voltage difference has to be less than the thermal voltage, $\mathrm{V_{th}} \equiv \mathrm{RT/F}$, with the gas constant R, the absolute temperature T and the Faraday constant F. At 25 °C the thermal voltage is about 25 mV. For this reason, in the field of SOFC research a voltage of 10-50 mV is applied to ensure the linearity of the investigated system [34,35].

Although EIS is a very effective technique for the comprehensive analysis of complex electrochemical systems, the influence of various experimental parameters has to be carefully considered. Variations of temperature, partial pressure, gas flow rates and sample preparation affect the measured impedance in different ways. However, if all parameters except one remain constant, single processes may be identified by characteristic changes in the impedance spectra [34,35].

2.4.1 Equivalent circuit model (ECM)

A frequently applied method to deconvolute the individual processes taking place in a SOFC, is the analysis with an equivalent circuit model (ECM). Complex chemical and physical processes, including mass- and electron transfer, electrolyte resistance and electrochemical reaction conductance in the cell, can be modelled using ideal electrical components, such as resistances, inductivities, and capacitors in the simplest case. Although this method offers an attractive way to describe the system, it has to be noted that there are always multiple electric circuits that represent the system in an equivalent way [34].

In order to model chemical reaction steps at the electrode or the bulk conductivity of the material, an electrical resistance can be applied in the circuit. Likewise, inductances and capacitors in general represent space charge polarisation regions or adsorption processes at the electrode. One should notice that these common elements are always assumed to show ideal behaviour. But as for instance a real resistor is not infinitely small, it additionally exhibits inductive and capacitive behaviour as well. Nevertheless, these characteristics can be neglected over a broad frequency range, thus the use of ideal elements allows a good approximation in equivalent circuits [35].

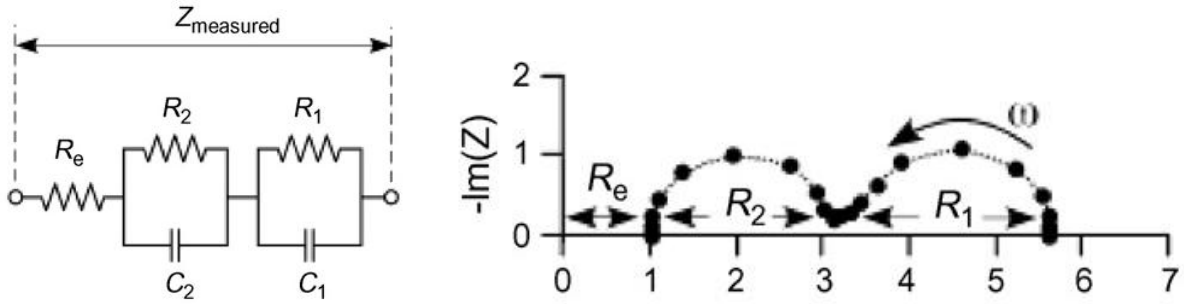

Figure 7: Simple possible depiction of an ECM to characterise the impedance Z (left) [34], associated Nyquist plot of Z (right) [34].

A simple equivalent circuit model for the description of a fuel cell is presented in Figure 7 (left) consisting of a resistance R_e which mainly represents the electrolyte (also known as series resistance R_s) and two RC elements connected in series (which each depict one ideal semicircle in the Nyquist diagram) (Figure 7 (right)) [34]. In this case the sum of R_1 and R_2 can also be denoted as the polarisation resistance R_p. The total ASR of the cell can now be obtained by adding up R_s and R_p.

In chapter 4.1, a constant phase element (CPE) is connected in parallel with the resistance in the ECM, instead of a capacitor, in order to calculate the values of the single elements. The definition of the impedance of a CPE allows setting any phase angle between a pure inductivity and a pure capacitor:

$$Z = \frac{1}{Q^0(j\omega)^n} \tag{21}$$

If Q^0 = C and n = 1, the impedance of a pure capacitor can be determined, while with Q^0 = L^{-1} and n = -1, the impedance of a pure inductivity is described. Moreover, it is also possible to depict the impedance of an ohmic resistance by the use of Q^0 = R^{-1} and n = 0. The CPE is mainly used in place of an ideal capacitor to describe inhomogeneous systems such as porous surfaces or capacitances at the grain boundaries owing to a distribution of relaxation times [38].

Analysing impedance plots in a physically meaningful way requires a lot of knowledge and experience, primarily because of the fact that it is quite difficult to separate the individual processes from each other. In order to distinguish different effects that contribute to the impedance of a full cell, a more detailed equivalent circuit was developed by Barfod et al. [39]. Based on results acquired from symmetric cell tests, the model shown in Figure 8 comprises five terms of R (ohmic resistance) and P (constant phase element, CPE) connected in parallel, and a separate term that represents the inductance (L) and the series resistance (R_s), respectively.

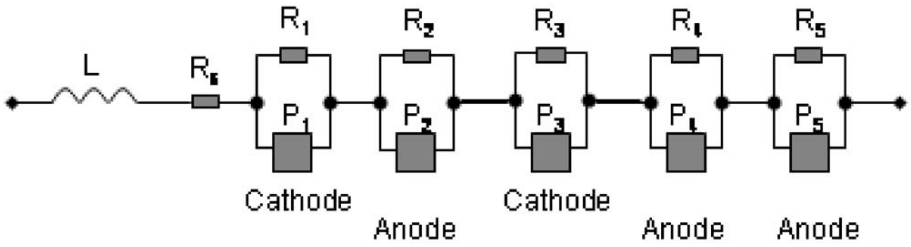

Figure 8: Equivalent circuit developed by Barfod et al. consisting of five R-P elements as well as serial and inductive elements [39].

In this model, L primarily depicts the inductance of the measuring cables, and R_s mainly the ohmic resistance of the electrolyte. The processes at the cathode are described by elements 1 and 3, which reflect the polarisation losses caused by the transfer of O^{2-} ions at the cathode/electrolyte interface on the one hand, and the dissociative adsorption of O_2 at the triple phase boundary on the other hand. With respect to the SOFC anode, element 2 represents the electrochemical polarisation losses, whereas sub-circuits 4 and 5 are applied to display gas diffusion and conversion processes. The peak frequency has the highest values for element 1 and decreases down to the lowest value for element 5 [39]. However, it has to be noted that this is only one proposal among many others for the nontrivial electrochemical description of a full cell with an equivalent circuit model.

3 Experimental setup

The aim of this chapter is to give a detailed description of the experimental setup used for all fuel cell tests performed during the course of this thesis. The setup is based on an earlier project work [40], whose aim was to put the *ProboStat* A-7 (device model without heated base unit) into operation. First, preliminary tests are described, which are essential for the development of this measurement setup. Furthermore, the overall concept and most important elements of the setup are presented. Finally, a recommendation for the assembling of the *ProboStat* and the test procedure is given. A picture of the developed measurement setup can be seen in Figure 9.

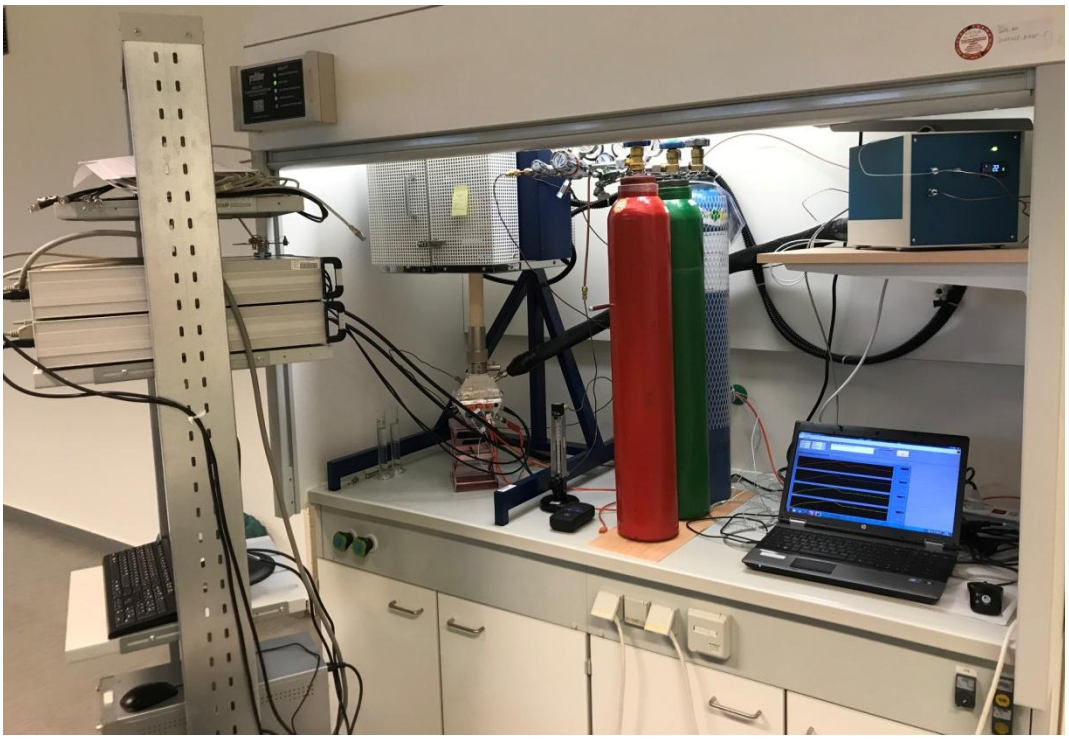

Figure 9: Measurement setup at the Chair of Physical Chemistry (MUL).

The centrepiece of the setup is the *ProboStat* with base unit heating system (NoreECs Norwegian Electro Ceramics AS) in which the button cell is mounted. The gas supply consists of three gas cylinders (H_2, Ar and 20% O_2/Ar) with a volume of ten litres each. The 20% O_2/Ar gas mixture is directly supplied to one compartment of the *ProboStat* (that means directly to the fuel cell) and can be regulated with a rotameter (Vögtlin V-100). H_2 and Ar stream through a humidification system, the *HumiStat,* where H_2O can be added to the gas flow. The gas mixture leaves the *HumiStat* via a heated gas line (maximum temperature 150 °C) to the other compartment of the *ProboStat*.

The top part of the *ProboStat,* where the cell is mounted, is placed inside a furnace (Elite Vertical Split Tube Furnace) with temperature controller (Eurotherm 2216e). In case that elevated temperatures are required at the top box of the heated base unit, an adjustable

resistive heating unit can be connected. Six thermocouples are installed to monitor the temperature at different positions of the system (see section 3.1.1). Four coaxial measuring cables connect the electrical output of the *ProboStat* with the potentiostat/galvanostat (Novocontrol POT/GAL 15V/10A) and the impedance frequency analyser (Novocontrol Alpha-A). A sketch of the experimental setup is depicted in Figure 10.

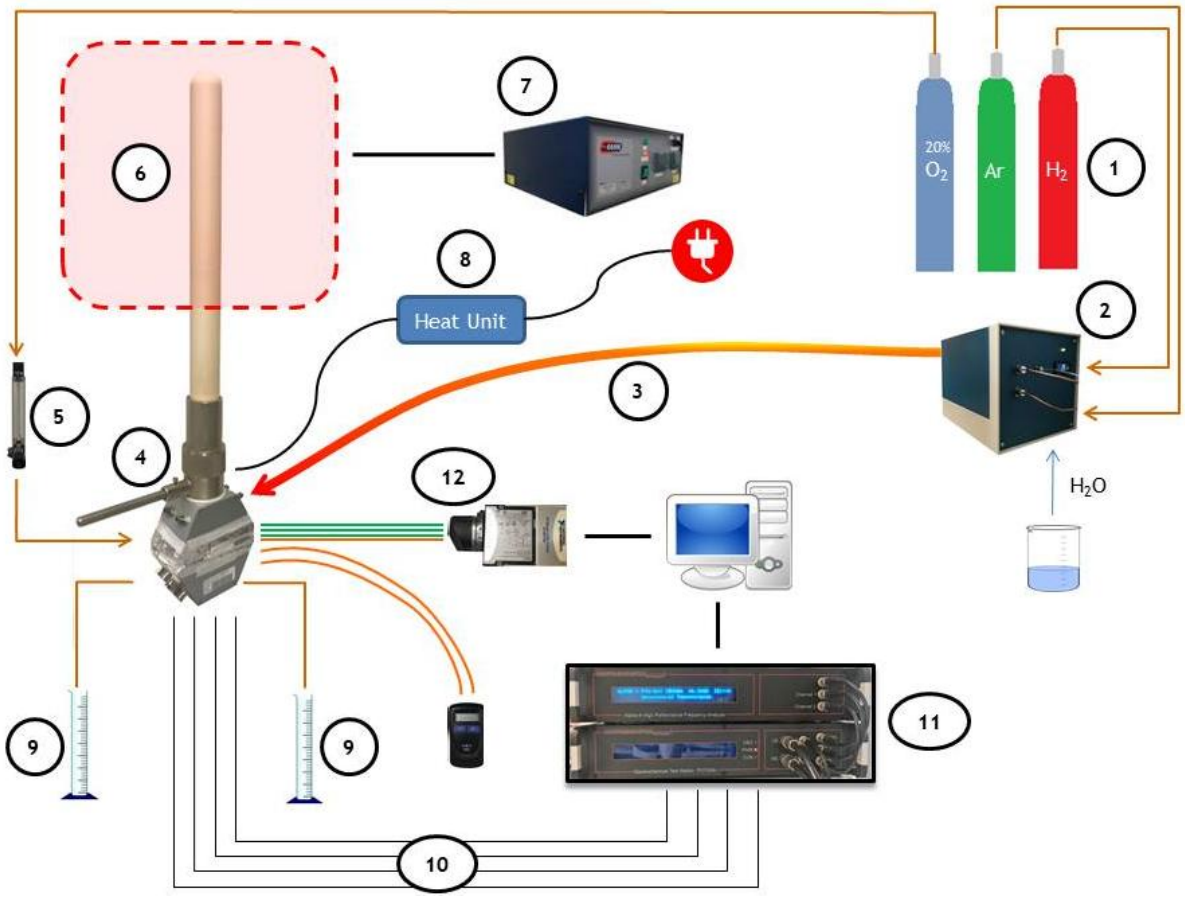

Figure 10: Experimental setup for measurements with Probostat
1… gas supply (20% O_2/80% Ar (blue), Ar (green), H_2 (red)), 2… HumiStat, 3… heated gas line, 4… Probostat, 5… rotameter, 6… furnace, 7… furnace temperature controller, 8…power source for heating unit, 9… measuring cylinder, 10… coaxial cables, 11… impedance frequency analyser + potentiostat/galvanostat, 12… thermocouple test leads + USB-connector.

3.1 Preliminary considerations

Before the first cells were mounted and tested in the *ProboStat*, it was crucial to take a closer look on possible problems reported in [40].

3.1.1 Temperature

The temperature is one of the most important parameters to be considered in fuel cell tests. For this reason a thermocouple is always placed close to the button cell in order to precisely monitor the cell temperature. The first tests already affirmed that the control

temperature of the furnace concurs with the temperature measured at the button cell for temperatures higher than 600 °C. For this reason, the control temperature can always be set directly without any temperature deviation appearing at the cell. Accordingly, there is no significant temperature difference in any of the experiments described in chapter 4.

Humid gas feeds are supplied to the cell entering the *ProboStat* via the heated gas line through the base unit. Therefore, the temperature must not fall below 100 °C during operation to prevent water condensation in the gas lines. For this reason, five thermocouples are installed to monitor the temperatures at different positions of the base unit which are marked in Figure 11 (left). The signals from the three K-type thermocouples are recorded and saved on the measuring computer while the two S-type thermocouples can only be monitored with a handheld display.

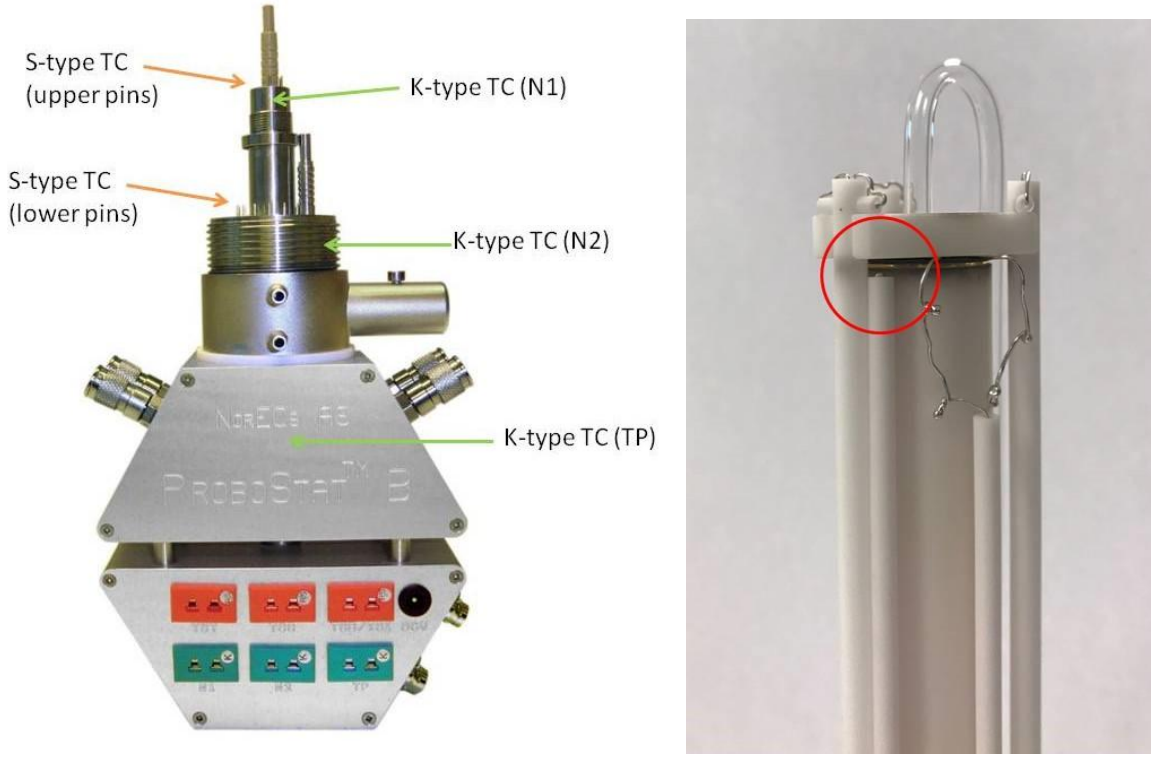

Figure 11: Installed K-type and S-type thermocouples in the base unit of the ProboStat (left), position of the cell thermocouple (right).

A resistance heater installed inside the top box can heat the crossing gas lines. The heat unit is supplied with direct current from an adjustable dc power source that allows setting the output voltage in 1 V steps by inserting chips with different ohmic resistances. According to the manufacturer, the top box is rated for a maximum temperature of 165 °C which has to be considered when applying high output voltages [41]. The temperature in the top box should be as high as possible to avoid water condensation. In preliminary tests, an output voltage of 9 V proves well as the temperature just slightly exceeds 160 °C at equilibrium. Additionally, an overheating protection disconnects the dc supply if the temperature rises above 165 °C. Figure 12 displays the temperature increase at three

different positions after the heat unit with an inserted 9 V chip has been connected. The furnace temperature is set at 800 °C and the *ProboStat* is insulated in the present test. At all measurement points the temperature clearly oversteps 100 °C in the state of equilibrium. The temperature inside the top box rises to approximately 165 °C which can be tolerated. If higher temperatures than 800 °C are required for cell tests, it might be necessary to use the 8 V chip since more heat is conducted from the furnace down to the base unit.

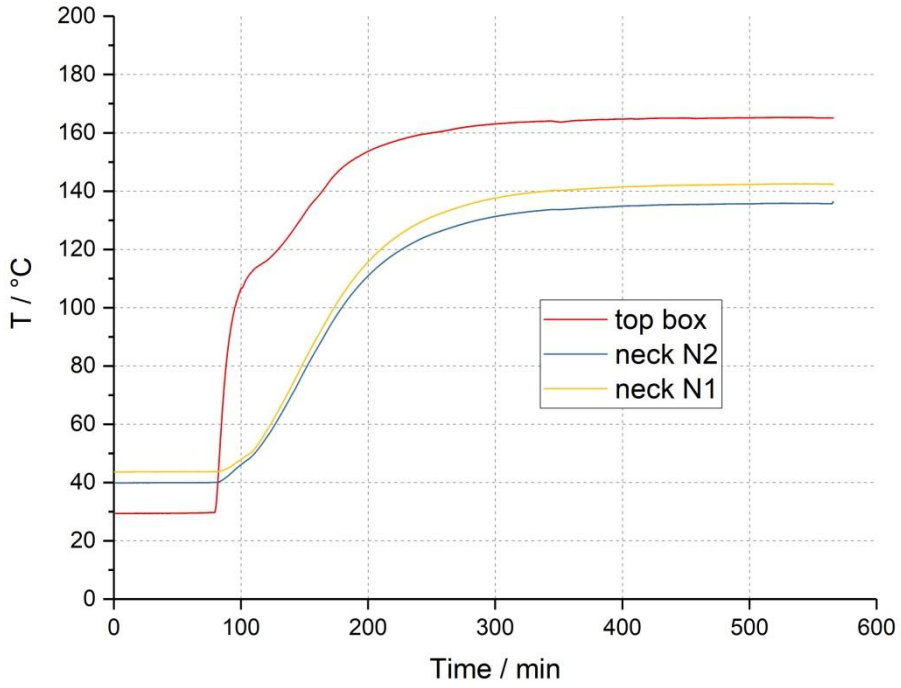

Figure 12: Temperature profile at three points of the base unit (TP, N2, N1) after connecting the heat unit (9 V chip). The furnace temperature is set to 800 °C and the ProboStat is thermally insulated.

In later performed tests it was found that for high water contents (>10%) the insulation and the heating of the base unit do not provide sufficient temperatures in all parts of the base unit. Water condensation and vaporisation highly influence the OCV and thus the measurement results obtained. To solve this problem, an additional heating cord is used at the gas outlets (see section 4.9.2).

3.1.2 Gas tightness of the cell

The preliminary work [40] already investigated the difficulty of sealing the *ProboStat* using a gold gasket. It recommends keeping the temperature at the cell constant at 1055-1060 °C for six hours (melting point of gold is at 1064°C). Moreover, the use of the stronger springs (marked in black colour) for the attachment of the spring load assembly is proposed. Another suggested idea is to glue the gold gasket on the support tube in order to prevent inadvertent movement of the gold gasket during cell mounting. According to the manufacturer, proper sealing is obtained in about 70% of all cases [42].

Building on this knowledge, different configurations (temperatures, use of superglue, dwell time) have been tested before the first cell tests were performed. In contrast to the recommendation of [40] it is observed, that a temperature of 1000 °C is high enough to soften the gold gasket sufficiently in order to prevent high gas leakages. The temperature should only be increased to 1055-1060 °C if large amounts of gas crossing to the other compartment are clearly identified. At temperatures close to 1064 °C, there is always a risk to melt the gold gasket due to temperature control faults of the furnace or local temperature peaks. Fixing the button cell with superglue on the support tube is highly recommended as it facilitates the mounting of the cell and did not show any negative impacts on the cell behaviour. Moreover, the gold gasket should be uniaxially pressed with 2 tons before mounting because this leads to a larger contact area of the gold gasket with the support tube and the cell. Regarding the dwell time, longer intervals are advantageous, but in most cases, keeping the temperature constant for two hours at 1000 °C results in complete gas-tightness of the cell. The recommended sealing procedure is described in section 3.2.2 and 3.3 as a result of these observations.

3.1.3 Insulation

Temperature variations in different parts of the *ProboStat* affect the cell behaviour and distort the obtained results if temperatures are not kept constant over the entire measurement time. Therefore, it is necessary to thermally insulate the *ProboStat*, in particular the outer cladding tube. Reducing the heat losses means higher heat transfer from the furnace down to the base unit, hence higher temperatures prevail in this part of the system. Glass wool is used as insulation material, covered by aluminium foil. Furthermore, the insulation is a safety feature, as it prevents direct contact with hot parts of the outer cladding tube at the furnace outlet. The insulated *ProboStat* with mounted heating cords is shown fully assembled in Figure 13. Here, the space between the top box and the bottom box is also insulated in order to minimize heat radiation. Electrical connections are located in the bottom box which must not be exposed to high temperatures.

Figure 13: ProboStat insulated with glass wool and aluminium foil in operation.

3.2 *ProboStat*

The *ProboStat*, which is the main part of the setup used for fuel cell tests in this thesis, is a device which allows various types of electrical and electrochemical measurements at elevated temperatures up to 1600 °C. It was developed by the Norwegian company NorECs in cooperation with the University of Oslo. Within this work, small button cells with a diameter of approximately 20 mm are investigated and characterized using the *ProboStat* with the base unit heating system, as described in [41]. Due to the fact that humid gas is applied to the *Probostat*, this configuration with internal heating is required.

3.2.1 Construction

The base unit of the *ProboStat* system consists of a hexagonal Ni-brass block, which is split into two parts to avoid overheating of the lower part (bottom box) through cooling by the streaming air. The cooling is necessary because the electrical connectors and switches, which are located in the lower compartment of the base unit, do not tolerate the temperatures needed in the upper compartment (top box) in order to avoid condensation of the water at the inlet and outlet gas lines. There are six connections for thermocouples (three K-type and three S-type thermocouples) and six electrical feedthroughs to contact the sample. Moreover, an electrical connection to power the integrated heater in the top box by a dc power source is installed in the bottom box. The inner and outer gas connection and gas lines are part of the top box, which can be actively heated by a resistor. All cables of the electrodes and thermocouples have to pass the top box on their way down to the electrical feedthroughs, thus the temperature here must not exceed 165°C.

If cooling is necessary, hose stubs for water cooling are located at the neck of the base unit. It is important to firmly fix the *ProboStat*, especially while assembling, to avoid

cracking the brittle ceramic parts of the unit. Therefore, a steel bar can be screwed into one side of the base unit.

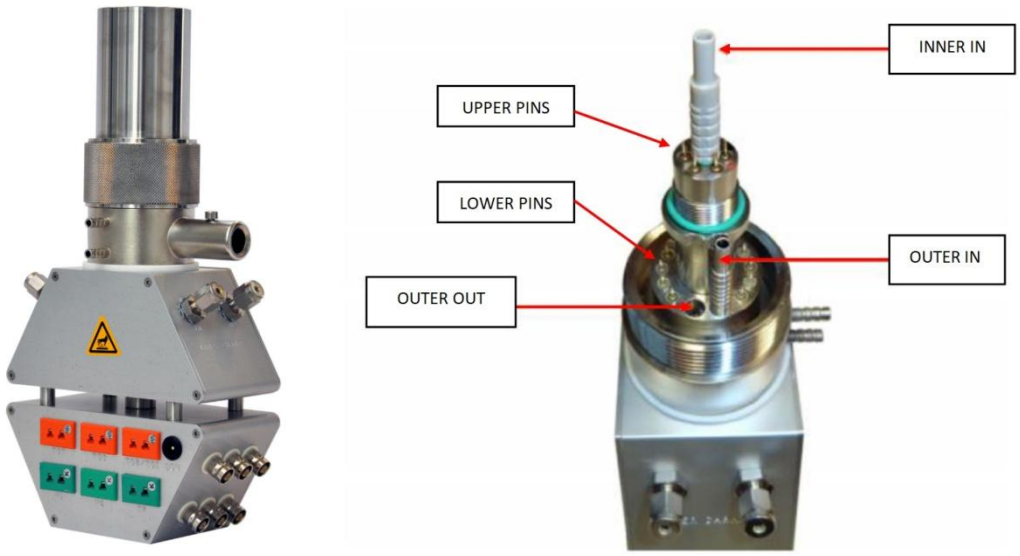

Figure 14: Heated base unit of the ProboStat with split base and mounted metal tube flange (left) [41], view on lower and upper pin levels with gas in- and outlets (right) [41].

At the neck of the base unit, one can find the electrical feedthroughs and the gas in- and outlets of both compartments of the *ProboStat*. There is a lower level for the outside compartment (pins 5-16) and an upper level with fewer pins (1-4) for the inner compartment (Figure 15). The electrical feedthroughs consist of mini-male-contacts, which are all embedded in polyether ether ketone (PEEK) insulation. On the lower level, pins 6 and 8 connect the outer current collector. The inner current collector is attached to the upper level pins 3 and 4. A four-hole capillary tube is screwed into the hole of the gas inlet of the inner compartment to transport the gases directly to the electrode surface. In contrast, the gas in the outer compartment flows via a riser to the top of the *ProboStat* where it is conducted to the outer current collector surface. In cell tests performed within this thesis either a bent silica tube or a thin-walled straight alumina tube are used as risers, depending on the mounting of the cell (see chapter 4).

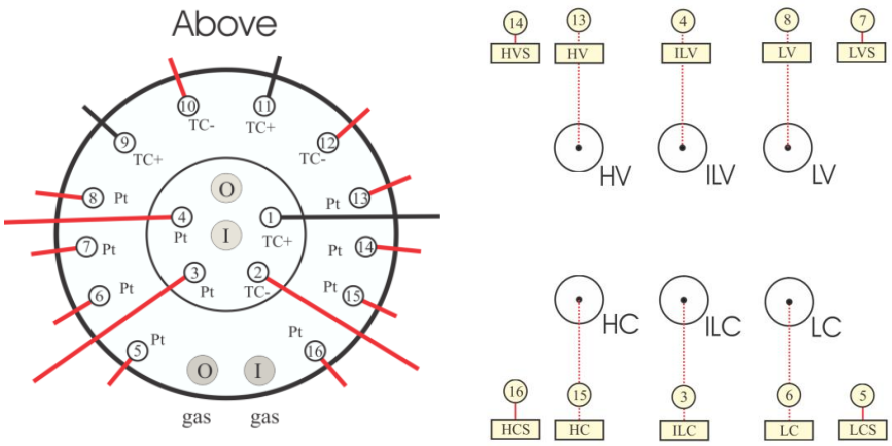

Figure 15: Contact arrangement of the inner chamber (pins 1-4) and the outer chamber (pins 5-16) (left) [41], contact arrangement of the bottom box of the base unit (right) [41].

An alumina support tube (OD = 20 mm, ID = 15 mm) separates the inner and outer compartment. In the setup used, the inner current collector, a thermocouple, and the 4-hole capillary tube are located inside the support tube, while the gold gasket and the cell are placed on the top of the support tube. The outer compartment contains the outer current collector, two thermocouples and the riser. An outer alumina cladding tube with a length of 50 cm and an outer diameter of 40 mm encloses the outer compartment and is tightly mounted with a metal tube flange. To inhibit gas leakage, Viton O-rings are used for both the support tube and the outer cladding tube.

3.2.2 Assembling

Before starting to assemble the *ProboStat*, all parts have to be cleaned with acetone to remove any interfering impurities from the surfaces. Then, the first step is to mount the four-hole capillary tube, the inner current collector and, if required, a thermocouple on the upper level pins. After an O-ring is put on the thread, the support tube can be screwed on. In previous studies on the *ProboStat*, it was a problem to centre the capillary tube, which might insert the edge of the inner current collector between the gold gasket and the cell, thus leading to gas leakage. In order to prevent this problem, a centring ring is put around the capillary tube. Contacts of the metal parts of the centring ring with the electrode wires should be avoided. The inner current collector can be fixed by sticking the small pin in the centre of the electrode area into one hole of the capillary tube.

Special care has to be taken during mounting of the button cell due to the fragility of the thin fuel cell. A slightly pressed gold gasket is first fixed on the support tube with superglue. The capillary tube, with the inner current collector attached on the top, always has to protrude from the support tube and the gasket to guarantee sufficient contact to the SOFC anode side of the button cell. Next, the button cell and the outer current collector are placed centred on the gold gasket and are fixed by the use of a triangular spring load assembly. The cell is normally installed with the SOFC cathode side up. This is the most critical step because any unbalanced pressure on the button cell might cause

fatal cracks in the fuel cell. In order to avoid damages, a small alumina bar is stuck through the hole of the triangular top plate of the spring load assembly to first centre the assembly, and second to apply a counter-pressure to the capillary tube. Three metal springs are clamped underneath the support tube to fix the triangular plate and to prevent slipping of the sample and the electrodes. In case that the cell breaks, the cracking is usually audible. Figure 16 depicts the mounting steps of the button cell in the *ProboStat*.

(a) (b) (c) (d) (e)

Figure 16: Mounting steps of the button cell in the ProboStat showing the inner current collector inside the support tube (a), the fixed gold gasket (b), the centred button cell (c), the outer current collector (d), and the mounted spring load assembly (e).

Next, an S-type thermocouple is mounted to monitor the cell temperature. In contrast to previous recommendations, the thermocouple is now fixed with a thin platinum wire at the spring load assembly. In the past it was clamped beneath the triangular top plate which may have caused minor leakages in preliminary studies. The last step is to mount the riser and to firmly screw down the outer cladding tube with the metal tube flange.

Finally, it should be checked if the two electrical connections of each electrode have contact to each other to ensure that no wire has broken during the assembly. Furthermore, the outer current collector must not be in contact with the ground, which can be checked by connecting it to the chassis screw of the *ProboStat*. Placing the *ProboStat* on a lab jack, the sample thermocouple can be positioned next to the thermocouple of the furnace for improved temperature control (175 mm vertical distance between the desk and the *Probostat* ground plate). The next step is to connect the gas lines to the base unit and to check if there is a leakage when gas is streaming through the system. Finally, all thermocouple connectors can be plugged into the base unit for monitoring on the computer.

3.3 Starting procedure

The trapped air in the chambers must be removed from the *ProboStat*, therefore gas flows from the beginning of the heating through both compartments. On the air electrode side, a gas mixture of 20% oxygen and 80% argon is supplied while pure argon flows on the fuel electrode side. The manufacturer recommends a gas flow of 10-30 ml_n/min [43]. Next, the temperature of the furnace is slowly increased up to 1000 °C at the cell with a heating

rate of 1 K/min. It is possible to use higher ramp rates up to 2.5 K/min, but in general low rate are preferable to avoid cracking of the ceramic layers of the mounted fuel cell. It is necessary to heat up the system to high temperatures to achieve better tightness of the gold gasket. The melting point of gold is 1064°C, getting close to this temperature softens the metal and improves the contact between the gasket and the inner sample tube. When the temperature has reached a constant level of 1000°C, it has to be checked whether the sealing is sufficiently gas-tight. If a gas leak is detected, the furnace temperature has to be increased up to a maximum of 1060 °C. Sometimes, the temperature has to be held constant for a few hours at this high temperature level to achieve sufficient gas-tightness of the cell. If the tightness test detects no leakage, the cell can be cooled down to the testing temperature applying a ramp rate of 2.5 K/min.

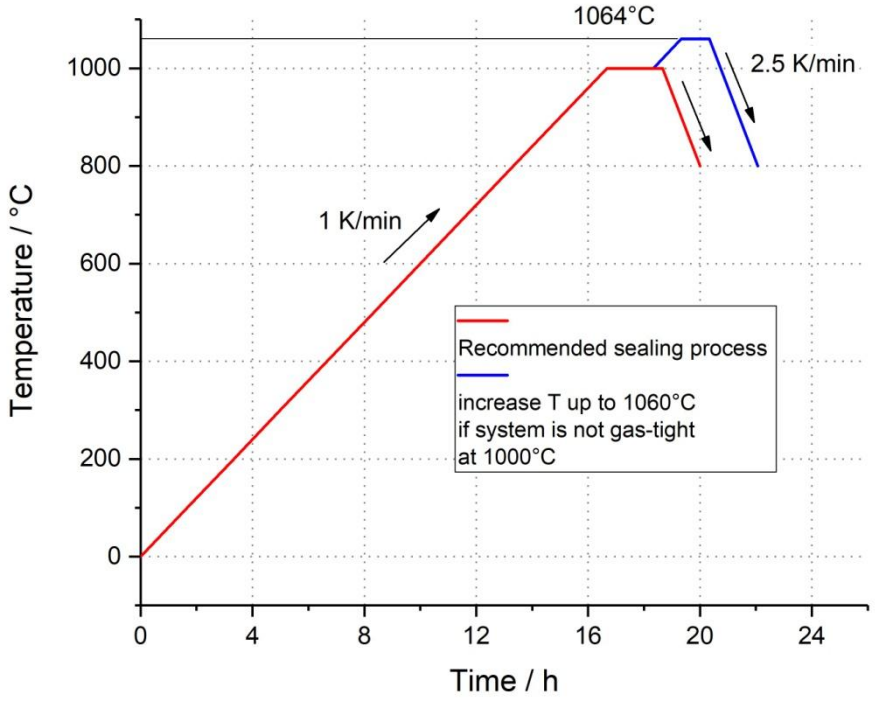

Figure 17: Recommended sealing process for the use of gold gaskets.

3.4 Gas-tightness test

The gas-tightness test provides information about gas leakages between the inner and the outer compartment. Therefore the following procedure, depicted in Figure 18, should always be applied:

1. Immerse both gas outlet lines about 1 cm below the water surface in a measuring cylinder.
2. Turn off the gas flow at the inner chamber.

3. Immerse the outer gas outlet line about 5 cm. Now the outer compartment of the *ProboStat* is exposed to a pressure of about 5 mbar (according to the hydrostatic pressure, an immersion of 1 cm leads to a pressure rise of 1 mbar). If the system is gas-tight, the bubbles only leave the *ProboStat* via the outer gas line. Bubbles escaping from the inner gas outlet line indicate leakage.
4. The same procedure should also be performed in the other direction to examine if the gas is just able to flow in one direction in the case of leakage. Now turn off the gas flow at the outer compartment and supply gas to the inner compartment.
5. Immerse the inner gas outlet line about 5 cm. In this case the system is gas-tight if no bubbles can be detected at the outer gas outlet line.

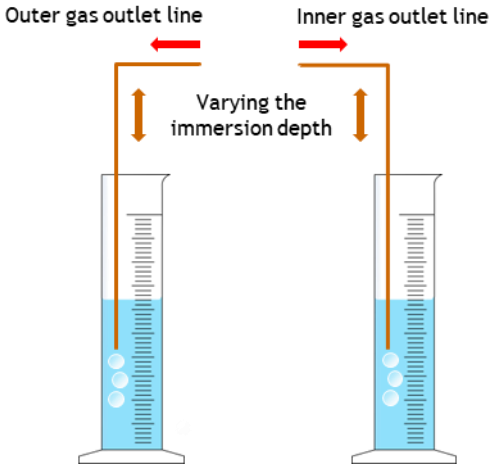

Figure 18: Gas tightness test using two measuring cylinders.

As both the cell and the *ProboStat* are designed to operate at ambient pressure, overpressures of more than 20 mbar should be avoided [43].

3.5 Reduction of the NiO/YSZ anode

After the sealing process, the *ProboStat* is cooled down to 800°C to perform the reduction of the anode from nickel oxide (NiO) to metallic nickel (Ni). Different approaches to reduce the NiO/YSZ cermet anode exist in the literature [44-46]. All of them have in common that the anode is initially not exposed to pure hydrogen, because this can cause cracks in the cell due to fast shrinkage of the anode structure. In the majority of procedures described, gas flows consisting of 4-10% of H_2 in Ar (or in N_2) are applied for various periods of time to the anode side. The H_2-content can then be increased step by step until pure hydrogen flows towards the anode. Monitoring the OCV can indicate the advance of the reduction and should be done over the whole reduction time. Finally, the OCV nearly reaches the Nernst-voltage depending on the tightness of the cell and the possible pressure difference in the inner and outer chamber. A practical implementation of the reduction process is presented for a number of tested cells in chapter 4.

3.6 *HumiStat*

The *HumiStat* is a device that enables the production of mixtures from gases and fluids by precisely measuring their input quantities. It allows the combination of two gases with one liquid. In this thesis argon, hydrogen, and water are the input substances. The *HumiStat* utilises a high accuracy syringe fluid pump and mass flow controllers, which were calibrated with real gases. The retraction of the syringe does not affect the composition of the mixture inside the *ProboStat* owing to the heated gas line, which buffers short-term variations in gas composition at the *HumiStat* outlet [47].

The mixture leaves the *HumiStat* via a heated gas line (HGL) of 122 cm length to the *ProboStat*. On the way through the HGL, the supplied water vaporises at a maximum temperature of 150 °C. The tube itself comprises many nooks and coves that buffer and stabilise the gas mixture at the outlet to the *ProboStat*. Nevertheless, it always takes some time until a newly set gas mixture reaches the fuel cell. Running the *HumiStat* with higher flow rates before setting the operating mass flow, reduces the time required to reach steady state [47].

3.7 Novocontrol Alpha-A mainframe frequency analyser + POT/GAL

All impedance and current-voltage measurements within this thesis were performed with the Novocontrol Alpha-A mainframe frequency analyser and the Novocontrol POT/GAL 15V/10A (potentiostat/galvanostat) as interface. The usage of this system enables ac measurements over a broad frequency range from 3 µHz to 1 MHz and is able to analyse samples with impedances from 0.1 mΩ to 10 TΩ. It allows the investigation of electrochemical materials or components in two-, three- and four-wire circuit configurations and enables the superimposition of applied ac signals with dc voltages up to +/-15 V or currents up to +/-10 A using one of the three possible modes [48]:

(1) ***Direct Voltage mode*** uses direct setting of ac and dc components at the counter electrode (CE) terminal voltage, varying the power analyser output voltage. It allows any combination of ac and dc signals, as long as not exceeding a peak voltage of +/-15 V, by applying a variable resistor. In contrast to potentiostatic and galvanostatic mode, it does not include voltage or current feedback from the sample.

(2) ***Potentiostat mode*** adjusts the CE terminal voltage in such a manner, that the differential voltage amplifier dV signal remains at set values taking into account feedback from the sample. In four-wire mode dV measures the voltage between the positive (RE+) and the negative reference electrode (RE-) terminal.

(3) ***Galvanostat mode*** can be applied to maintain the CE terminal voltage in order to keep the ac and dc components of the resulting current A_{we} applied to the working electrode (WE) terminal at set values, taking into account feedback from the sample.

Within this thesis, the *Direct Voltage mode* is used for electrical impedance measurements and the *Galvanostat mode* for current-voltage measurements, respectively.

It is recommended to calibrate the devices once a month in order to avoid erroneous deviations in the results owing to long-term drift effects. A detailed description of the calibration procedure and further information about the applied devices can be found in [48].

3.7.1 Measurement configuration

All impedance measurements are carried out in four-wire configuration using the software WinDeta (Novocontrol technologies). A frequency range going down from a maximum of 1 MHz to a minimum of 10 mHz is chosen with ten measuring points per decade. Applying these setting, a frequency sweep takes about 37 minutes. In some cases, the impedance values at low frequencies (<1 Hz) do not give relevant information and are thus not considered in further analysis. An ac voltage with amplitude of 20 mV is applied by the system's generator to the cell. Impedance measurements are all performed in *Direct Voltage mode*, therefore the actual dc voltage, which is the OCV in this case, is set at the CE-terminal in order to obtain more precise results. Figure 19 shows all the required settings in the configuration window.

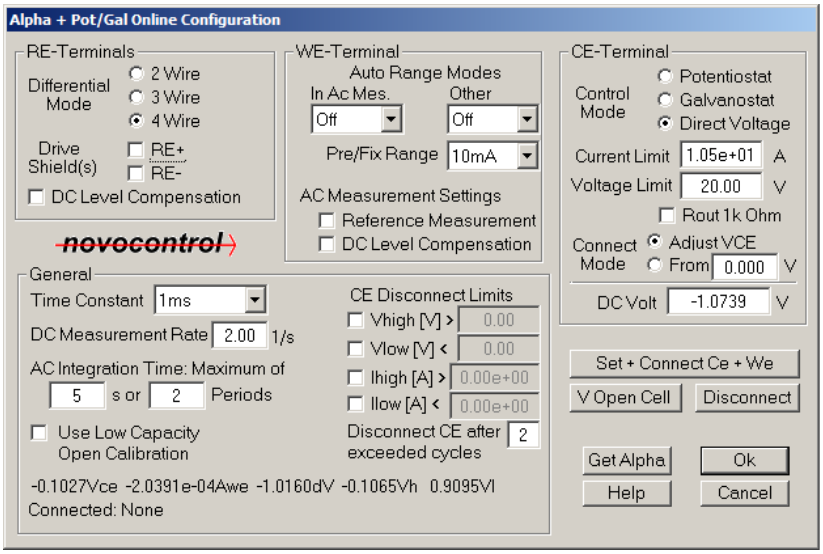

Figure 19: WinDeta configuration of the frequency analyser for impedance measurements in direct voltage mode.

I-U characteristics are recorded using the software WinChem (Novocontrol technologies). All current-voltage measurements are performed in four-wire *Galvanostat mode*. Different current profiles for SOFC and SOEC mode can be applied depending on the performance of the cell. A ramp rate of 1 mA/s is set for all I-U tests. Moreover, it is important to set an adequate current range for each test. If the chosen ranges are too high, it results in higher

measurement errors. Likewise, current ranges have to be considered in WinDeta for impedance measurements.

For SOFC/SOEC-testing with the Novocontrol Alpha-A mainframe and the POT/GAL 15V/10A interface in four-wire mode, the working electrode (WE) and the negative reference electrode (RE-) should be connected to the air electrode (SOFC cathode or SOEC anode), whereas the counter electrode (CE) and the positive reference electrode (RE+) should be attached to the fuel electrode (SOFC anode or SOEC cathode). In this configuration the current is counted positive for SOFC operation (negative for SOEC operation) while the voltage polarity is negative. Do not exchange the current leads only (WE and CE) or the voltage probes only (RE+ and RE-) in order to change the polarity of the respective signal, because this will lead to errors in EIS measurements. Instead, polarities can be changed during data export from WinChem, if necessary. Using the connectivity given above, export with “Current [A]” and “Voltage EC [V]” to keep the current sign (i.e. positive for SOFC operation) and reverse the voltage polarity to obtain positive potential values.

4 Button cell tests

This chapter describes the cell tests of the nine button cells which were examined in the course of this thesis. First the type of the tested cell is explained once for every different cell type used. A detailed description of the test procedure is given in order to present all steps applied in detail. The subchapter *Results* includes a discussion of the measured impedance spectra and current-voltage characteristics. Moreover, XRD and SEM results are analysed for selected cells.

4.1 Data processing

The measured data must be processed for further use in order to achieve better comparability to other fuel cell tests. The first step when interpreting the measurement results, is to remove all points that have resulted from measurement errors because they do not give useful information. All EIS measurements are performed in a frequency range from 1 MHz to 10 mHz. In some cases, the data obtained at low frequencies are not included in the graphic evaluation of the results. The boundary conditions should be held constant during the EIS measurement. But as one single impedance measurement lasts for a few minutes at low frequencies, the OCV is always slightly oscillating, even if the system is completely gas tight and water condensation is prevented. Since it is impossible to always guarantee absolute stability of all boundary conditions in the *ProboStat*, some of the measuring points at low frequencies can deliver deviating results. Moreover, the inductance, which represents the cables connecting the frequency analyser with the cell, is subtracted from the imaginary part of the impedance. To determine this inductance, the equivalent circuit model depicted in Figure 20 is applied in WinFit for each spectrum.

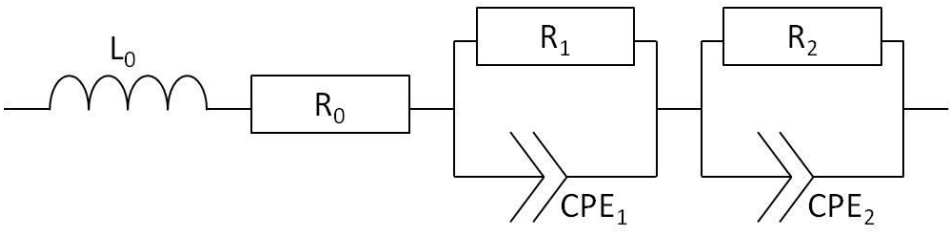

Figure 20: Equivalent circuit used in WinFit to determine the system's inductance.

To ensure comparability, all impedance values are multiplied with the cell area, which is the cathode area (smallest diameter of all layers) for all tested anode-supported cells. The resulting unit of the area specific impedance is Ωcm^2. Also the currents in I-U characteristics should be related to the cell area, thus they are divided by the cathode area. Here the unit used is $mAcm^{-2}$.

4.2 Sample preparation for scanning electron microscopy (SEM)

Seven of the nine tested cells were investigated with SEM for post-test analysis. Therefore, a sample preparation has to be done, which includes embedding, polishing and electrical contacting of the cells or cell fragments.

4.2.1 Embedding

The first step is to mount the cell on a plastic clip in order to fix it in perpendicular position, which is important to obtain correct values for the layers thicknesses in the following analyses. The clip is placed centrally in an embedding mould with a diameter of 30 mm. The used embedding material is a transparent epoxy-resin system (Kulzer Technovit EPOX), which consists of a resin and a hardener component. 12 g of the resin and 6 g of the hardener are mixed in a cup and then poured carefully into the greased embedding form to fix the cell. After 18 hours, the epoxy resin has cured and is ready for further processing.

4.2.2 Polishing

Before polishing, the embedded cell has to be cut into two pieces using a saw with diamond blade (Buehler Precision Saw Isomet 1000). Then, one part of the sample is polished in several steps with a polishing machine (Buehler Grinder-Polisher BETA). As abrasive material, silicon carbide papers (Buehler CarbiMet^{TM}) are used. First, the roughest paper P180 is used for pre-polishing. Afterwards, the papers get increasingly finer (P320, P600, P1200, P4000). After every polishing step, the sample is cleaned in an ultrasonic bath (Elma Elmasonic S 30 H) to remove impurities from the abrasive paper and abraded sample material.

4.2.3 Electrical contacting

For SEM analysis, the polished sample has to be electrically contacted. In our case, the sample is coated with a gold layer of 1 nm thickness using a sputtering device (Bal-Tec Med 020 high vacuum coating system). Moreover, a line of silver paste is painted from the cell to the bottom of the epoxy resin cylinder to provide better electrical contact.

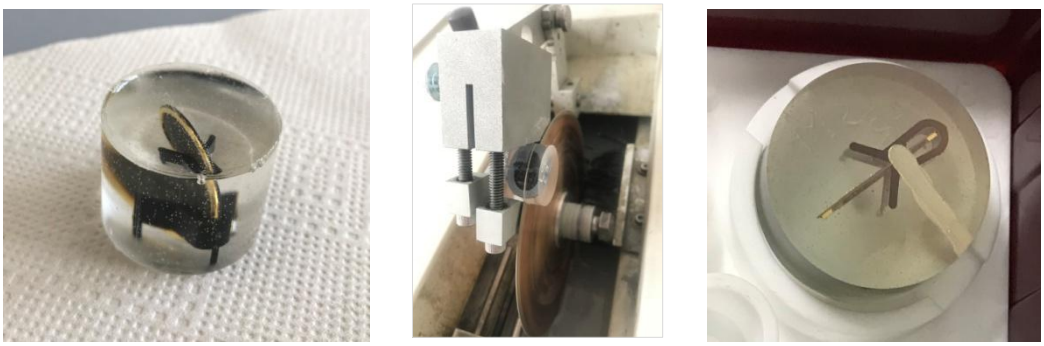

Figure 21: Embedded cell (left), cutting cell with saw (middle), contacted sample (right).

4.3 Cell 1 (LSM)

The first cell tests and their results described in this chapter are performed to examine the measuring system. The emphasis of these measurements is on reviewing the correct operation of all devices, including the handling of the impedance frequency analyser and the potentiostat in real fuel cell tests. As the preliminary tests still reveal problems with gas leakages in the system, special focus is on checking the gas-tightness.

4.3.1 Description of the cell

An anode-supported cell (ASC) manufactured by the company Fuel Cell Materials is mounted in the *ProboStat*. The button cell with an outer diameter of 20 mm consists of a Ni/YSZ anode, a thin YSZ electrolyte and a screen printed LSM cathode with a diameter of 13 mm. This cell is denoted as Cell 1 in the text below. Since the thin cell is very fragile, it must be handled very carefully to avoid damage during mounting in the *ProboStat*.

4.3.2 Test procedure

The first button cell broke into two pieces during mounting, which was detected by an audible noise. Thereafter, a second cell was successfully installed with the cathode side up. After the complete assembling of the system, it was heated up to 1000 °C with a ramp rate of 1.5 K/min. In an attempt to improve the contact of the gold gasket with the support tube, the temperature was further raised to 1060 °C with 1 K/min, which is already very close to the melting point of gold (1064 °C). At this temperature the *ProboStat* exhibited no gas leakages and was thus cooled down to 800 °C with 2.5 K/min.

Finally, the reduction process was carried out supplying pure hydrogen to the anode. After 45 min, the OCV was constant at 1.12 V at gas flow rates of 22.2 ml_n (= 200 µg/min) H_2 and 30 ml_n of the gas mixture containing 20% O_2 and 80% Ar, respectively. The first measurements were executed shortly after the OCV remained constant.

4.3.3 Results

The following results with pure H_2 on the fuel side were obtained without thermally isolating the *ProboStat*. Measurements in a humid atmosphere with 20% H_2O were performed after the isolation was attached to the outer cladding tube and after the heat unit of the top box was switched on.

A variety of impedance spectra is displayed in Figure 22 at temperatures of 750 °C, 800 °C and 850 °C. As expected, the polarisation resistance R_p increases when lowering the temperature but there is also a change in the shape of the spectra. While at 850 °C and 800 °C three semicircles can be clearly identified, a nearly linear slope at high frequencies appears at 750°C. The spectrum shown in light green colour was measured four days after the one marked by dark green symbols, indicating some performance loss due to

degradation, especially at 750°C. In contrast, the spectra which were acquired at 850°C and 800°C show only small time-dependent changes within the duration of the measurements. The series resistance R_s slightly increases at lower temperatures, as well as over time. However, compared to R_p, R_s is very small. The area-specific resistance (ASR) of the measured cell is very high, compared to literature values for the same cell type [49].

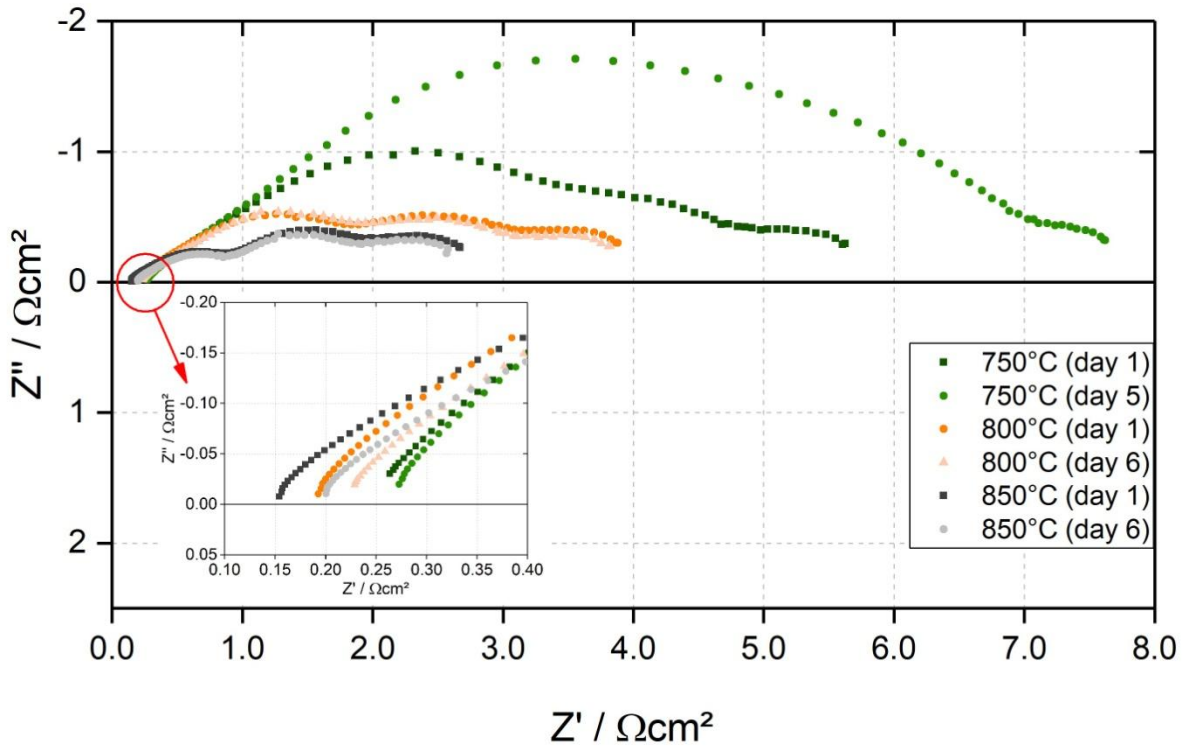

Figure 22: Impedance spectra of Cell 1 at various temperatures in dry H_2 vs. 20% O_2/Ar.

The current-voltage characteristic of Cell 1 verifies the better performance of the cell at higher temperatures due to lower polarisation resistances. Owing to the limited performance, cells with LSM cathode are usually operated in a temperature range of 800 °C to 1000 °C. In order to avoid a possible re-oxidation of the anode, the minimum cell voltage should in general not fall below approximately 0.6 V during operation. Shortly after the H_2O content was increased to 20% on the SOFC anode side, the OCV significantly declines and then keeps oscillating between 0.8 V and 0.9 V. According to the Nernst equation, at this humidity level a voltage of 1.005 V should be obtained at 800 °C (see appendix 7.2). As it can be seen in the red curve of Figure 23, the voltage already drops abruptly at small current densities. The following gas-tightness test reveals no leakage, hence considerable changes in the gas concentration can be excluded. A possible cause might be a change in the material properties of the cell.

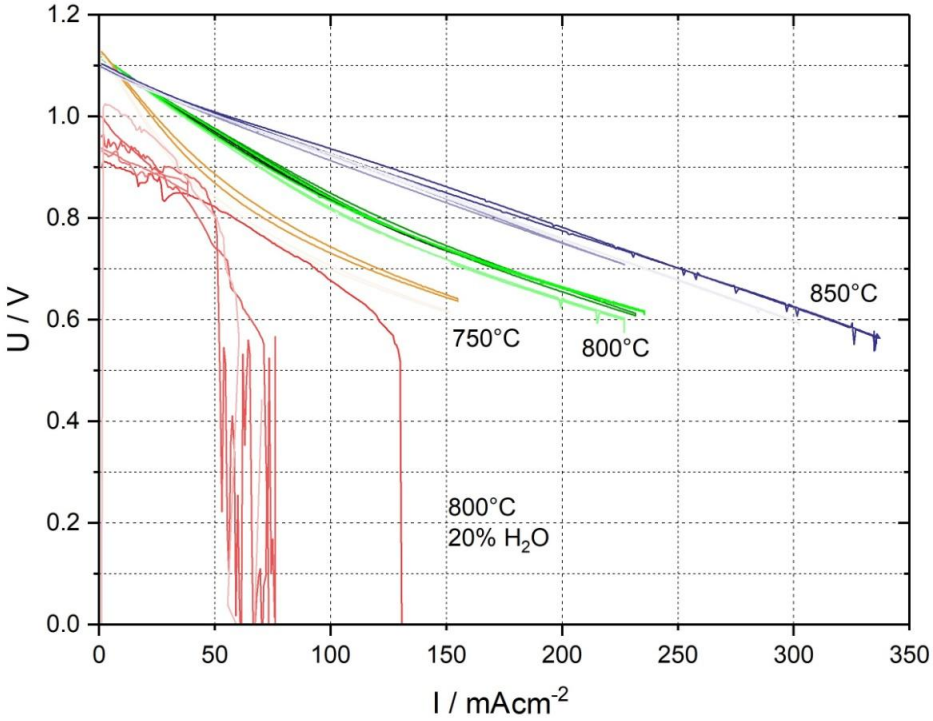

Figure 23: Current-voltage characteristics of Cell 1 at different temperatures in dry and humidified H_2 vs. 20% O_2/Ar.

After the system was cooled down (using Ar instead of H_2 on the fuel side), it could be confirmed, that the cell was still gas-tight from the inside out. The disassembled fuel cell exhibits a small crack between the reduced and the unreduced parts along the outer perimeter of the gold gasket. However, it cannot be determined if the crack is a result of the fast reduction of the anode or if it occurred during cool-down. Moreover, it is rather unlikely that this should be responsible for the failure of the cell in humid atmospheres. Apart from that, neither the cathode nor the anode shows any anomalies. The gold gasket is rigidly connected to the anode due to sintering, which does explain the good gas-tightness of the system.

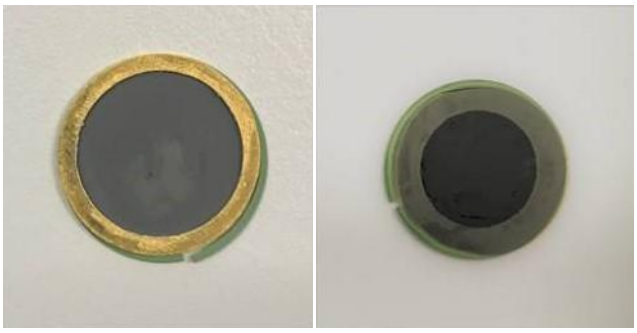

Figure 24: Grey anode of Cell 1 with gold gasket (left) and black cathode (right).

The test setup worked reliably in the first cell tests without any major problems of the electric instruments or other auxiliary devices.

4.4 Cell 2 (LSM)

In order to verify the results obtained from Cell 1, a similar second cell of the same size and type (see section 4.3.1) with LSM cathode was investigated. In the following, this cell is denoted as Cell 2. The aim of the tests performed with Cell 2 was to take a closer look at the variation of humidity at the fuel side in SOEC and SOFC operation. All measurements were recorded at a temperature of 800°C.

4.4.1 Test procedure

The assembling of the *ProboStat* and the installation of the button cell with the cathode side up were carried out without any problems due to the previously gained experience in handling the spring load assembly. The cell was heated up with a ramp rate of 1.5 K/min to 1000 °C. As the cell was not completely gas-tight at this temperature, it was further heated to 1060 °C with 1 K/min and held constant for 30 min. As no more gas leakage could be detected, the cell was cooled down to the test temperature of 800 °C. The reduction process of the anode was performed in the same way as for Cell 1. Argon was substituted by pure H_2 and after 30 min the OCV was constant at a level of 1.14 V.

Shortly after the reduction process, the first tests were performed varying the water content from 0% (dry H_2), to a maximum of 40% H_2O. A 20% O_2/Ar flow of 30 ml_n was set at the air side for all measurements. The mass flows of the gas mixtures on the fuel side are displayed in Table 2. Afterwards, additional tests with dry H_2 and 5% H_2O on the fuel side were performed to check if any degradation effects can be observed.

Table 2: Mass flows of H_2 and H_2O in the fuel feed for different H_2O contents (Cell 2).

H_2O content / vol%	**Mass flow H_2 / µg min^{-1}**	**Mass flow H_2 / ml_n**	**Mass flow H_2O / mg min^{-1}**	**Mass flow H_2O / ml_n**
0	2000	22.2	0	0
5	2000	22.2	1	1.2
10	2000	22.2	2	2.4
20	2220	24.7	5	6.2
40	2000	22.2	12	14.7

The addition of water significantly influences the stability of the OCV, as it is displayed in Figure 25. Different periodic processes appear with deviating periodic duration and amplitude. It is interesting to see that the highest fluctuation occurs at the lowest humidity level of 5% H_2O with the longest period duration and the highest amplitude. Fluctuations of more than hundred mV do not allow meaningful results, but it should also be noted that this form of OCV-oscillation does not always take place in a similar way. For the results presented for Cell 2, the measurements were recorded when the OCV was more stable than shown in Figure 25. In later tests, water condensation at the gas outlets of the

base unit, which is the reason for the observed fluctuations, is prevented by additional heating which stabilizes the OCV especially at high H_2O contents. At a lower humidity (5-20% H_2O) there are also other effects causing the fluctuation of the OCV (see chapter 4.9).

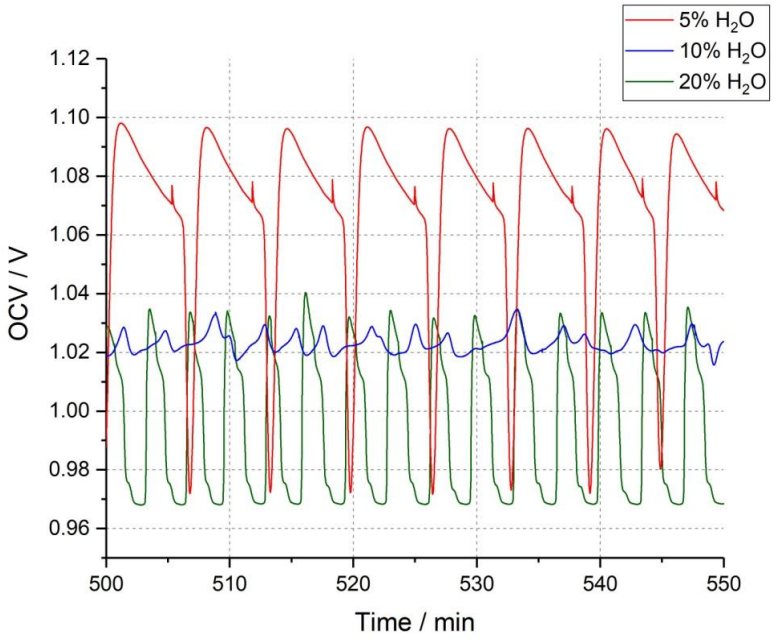

Figure 25: Fluctuations of OCV at different H_2O contents (Cell 2).

4.4.2 Results

The humidification of the H_2 inlet gas flow has a significant impact on the form of the impedance spectra, as can be seen in Figure 26. In the first measurement performed with dry hydrogen, the cell exhibits a much higher polarisation resistance R_P than in the following tests with H_2O in the fuel feed. Even at a H_2O content as low as 5%, R_P strongly declines and keeps decreasing with increasing water contents. By contrast, the series resistance R_s (high frequency intercept on the real axis) slightly rises at higher moisture levels. Moreover, the form of the spectra changes, showing less clear separation of the semicircles upon water addition. Here, the three identified semicircles merge almost completely with each other.

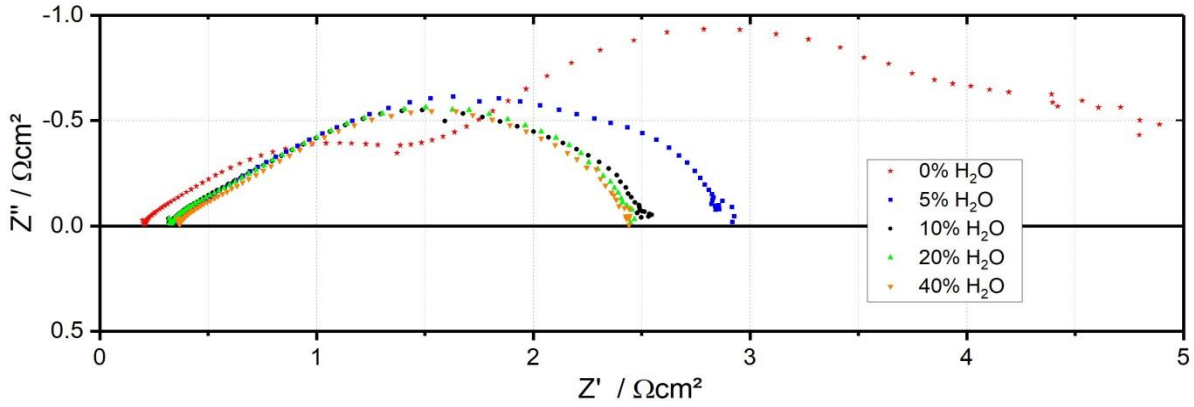

Figure 26: Impedance spectra of Cell 2 at 800° C at different H_2O contents.

The effect of humidification on the performance of the cell is demonstrated in Figure 27. The red curve represents the performance of the fresh cell fed with dry H_2 on the fuel side in SOFC operation mode. At the maximal applied current density of 226 $mAcm^{-2}$ (300 mA total current), the voltage obtained is 655 mV. Especially due to the lower OCV, SOFC tests at higher humidity levels do not attain equal current densities even though the slope of the curves is nearly similar.

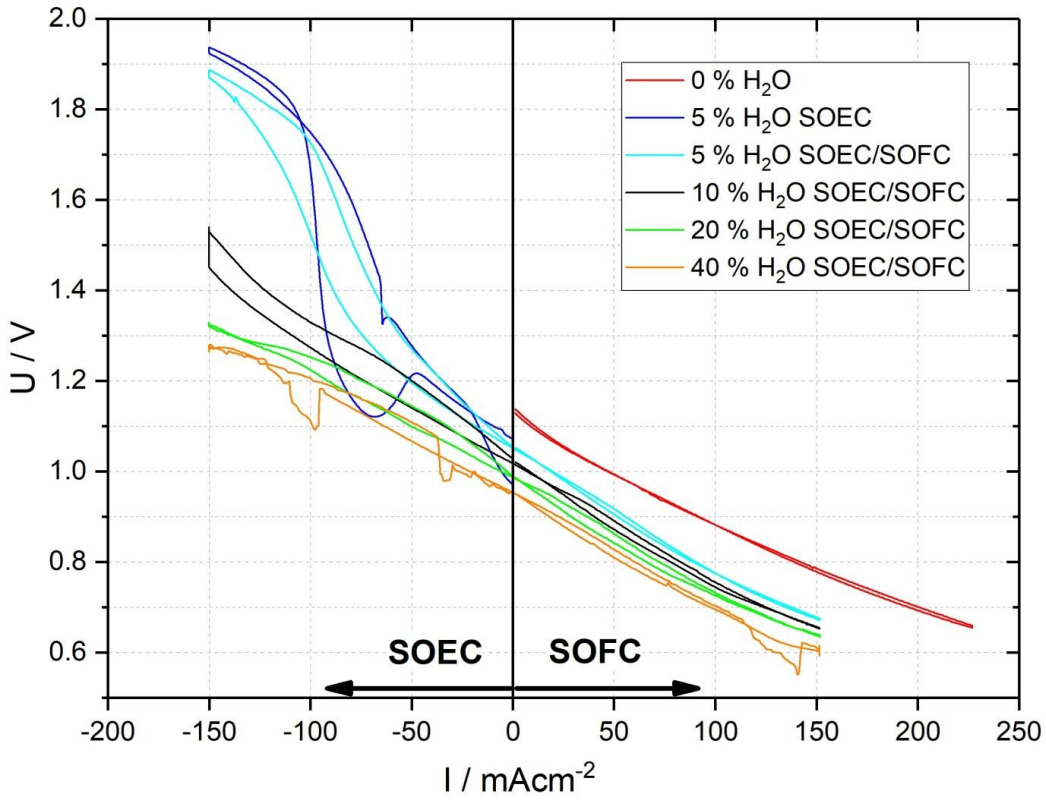

Figure 27: Current-voltage characteristics of Cell 2 at 800 °C at different H_2O contents in SOEC and SOFC operation mode.

On the negative side of the abscissa, the results in SOEC operation mode are pictured. At 5% H_2O, cell performance is affected by H_2O starvation, which is indicated by the voltage

rise at 50 $mAcm^{-2}$ (theoretical limiting current at 5% H_2O: 134.5 $mAcm^{-2}$). The OCV is not steady when H_2O is added to the fuel feed which can explain the fluctuation of the dark blue curve. The voltage drops recorded at 40% H_2O (orange curve) may depict condensation and vaporisation processes at the gas outlet of the *ProboStat*.

Further tests of the cell were performed before cool-down in order to detect possible degradation effects. As the cell was already operating for three weeks (approx. 500 h) it is entirely possible that, especially in small laboratory facilities, materials already reveal performance losses. If there is some gas leakage between the two chambers of the *ProboStat*, the gas from one side might impair the electrode on the other side.

Measurements in dry H_2 and with 5% H_2O clearly show the deterioration of the cell performance with time. Figure 28 depicts the increase of the polarisation resistance R_P. Moreover, it can be seen that in dry H_2 the semicircles merge more deeply with time, similar to the impedance spectra displayed in Figure 22. This might indicate that the water applied to the cell caused an irreversible change in the composition or the microstructure of the cell materials as the identified semicircles of the fresh cell do not reappear in dry H_2.

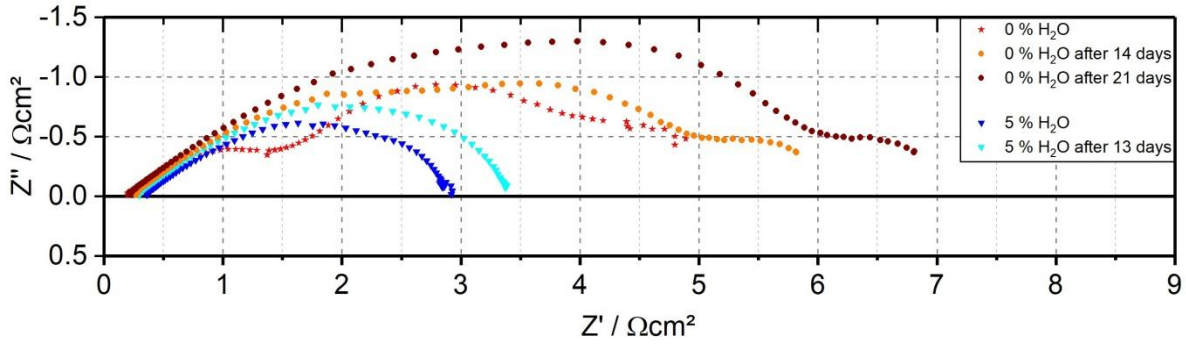

Figure 28: Impedance spectra illustrating degradation effects of Cell 2 at 800° C.

The degradation is even more visible in the I-U characteristics in Figure 29, in particular considering the results obtained in dry H_2 shown in the right diagram. After the cell was exposed to humid gas atmospheres on the fuel side, the original cell performance could not be recovered and remained significantly below the initial performance in pure H_2. Moreover, the OCV was lower at later tests which may be caused by residual steam in the gas chamber or increasing problems with the gas-tightness.

At a H_2O content of 5%, the degradation effect is less discernible in Figure 29 (left) and better visible in the impedance pattern (Figure 28). Nevertheless, the steeper gradient of the red curve at OCV level verifies the rise of the cell resistance with time.

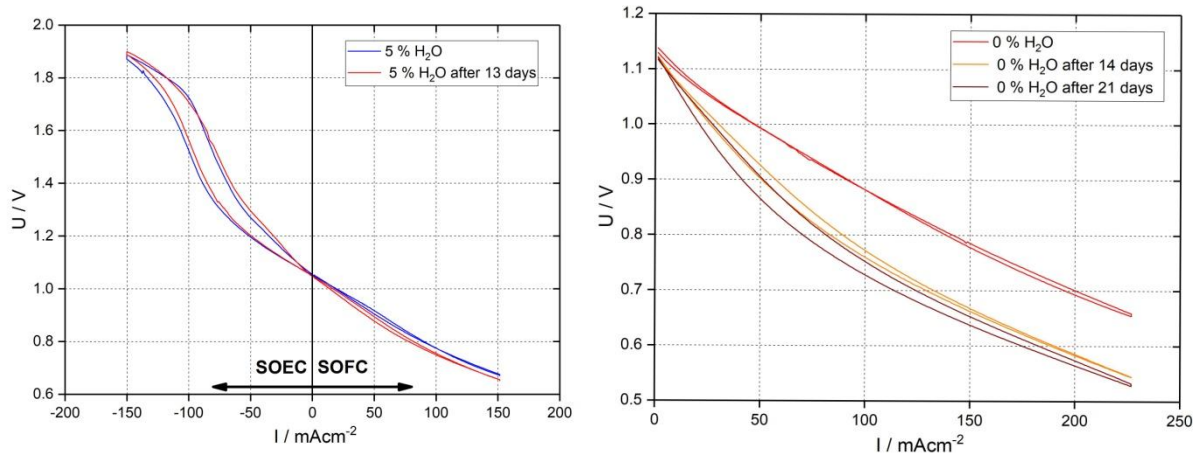

Figure 29: Current-voltage characteristics illustrating degradation effects of Cell 2 in 5% H_2O (left) and dry H_2 (right) at 800°C.

4.4.3 Scanning electron microscopy (SEM)

A cross section of the tested cell was analysed in the SEM. Five different layers could be identified by means of Z-contrast in backscattered electron mode:

(1) Porous LSM as current collector, thickness 33 µm
(2) Cathode functional layer of an LSM/Sm-doped CeO_2 composite, thickness 9 µm
(3) Thin porous diffusion barrier of Sm-doped CeO_2, thickness 5 µm
(4) Densely sintered YSZ electrolyte, thickness 8 µm
(5) Porous Ni/YSZ anode substrate, thickness 240 µm

The thicknesses of the layers are all in the expected range. The La:Sr-ratio of the LSM cathode is determined as 0.8:0.2 using EDX. Comparing the electrode layers in Figure 30, the porosity of the cathode appears to be much higher than the porosity of the anode. The presence of a Sm-doped CeO_2 diffusion barrier is surprising as LSM (usually slightly A-site sub-stoichiometric) is one of the few cathode materials which show sufficient compatibility with YSZ.

No signs of delamination can be observed in the SEM images, which indicate that the applied testing procedure has no negative impact on the mechanical integrity of the cell. EDX-analysis of the electrolyte layer shows the presence of small amounts of hafnium, which is a common impurity in zirconium compounds, from which it is difficult to separate. Further impurities are not identified by EDX.

(a)

(b)

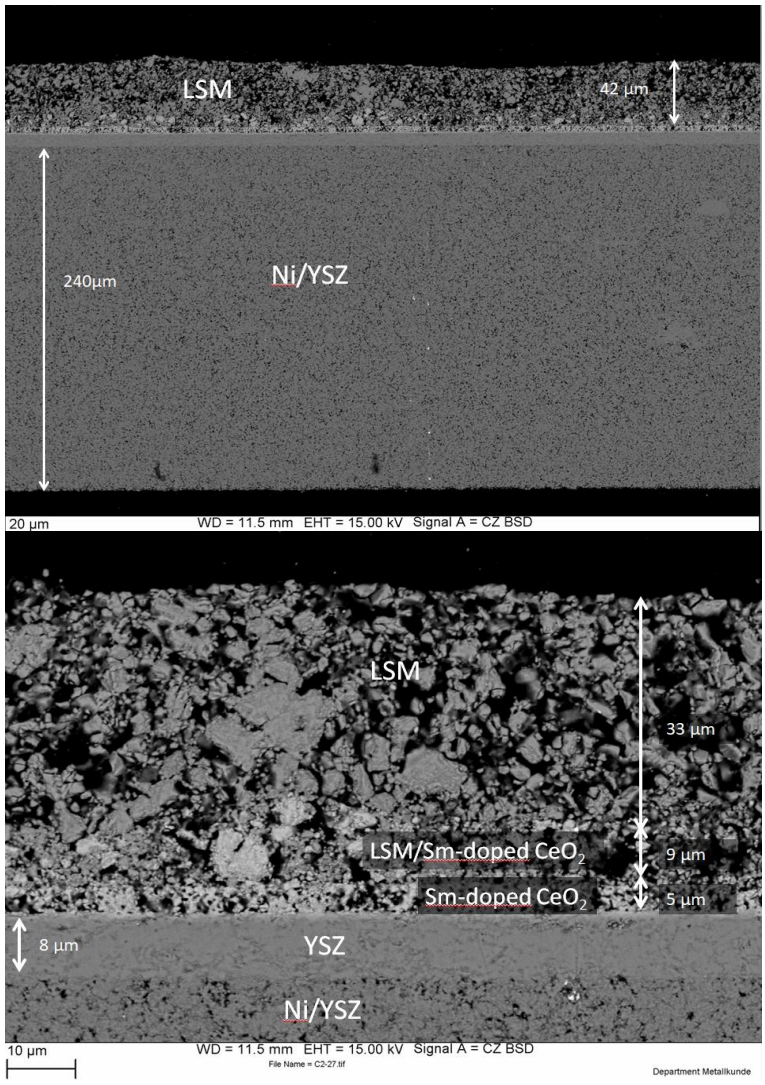

Figure 30: SEM-BSE images of a cross section of Cell 2 showing (a) the whole cell (b) a magnified region with current collector, cathode, diffusion barrier, and electrolyte layers.

4.5 Cell 3 (LSC)

$La_{1-x}Sr_xCoO_{3-\delta}$ (LSC) is one of the most promising cathode materials for reduced temperature SOFCs, as described in section 2.3.3.2. The aim of the following tests is to compare the performance of cells with LSC and LSM cathodes in order to gain a meaningful benchmark for all further tests, especially for those with newly developed cathode materials, performed with the *ProboStat* setup.

4.5.1 Description of the cell

In analogy to Cell 1 and Cell 2, the tested cell is an anode-supported cell produced by Fuel Cell Materials consisting of the same Ni/YSZ cermet for the fuel electrode. The electrolyte is made of YSZ and a diffusion barrier is applied between the electrolyte and the LSC cathode. The outer diameter of the button cell is 20 mm, while the diameter of the screen printed LSC cathode is 12.5 mm. The cell is denoted as Cell 3 in the text below. Table 3 presents the manufacturer's data of the cell [50]:

Table 3: Specification of Cell 3 according to the manufacturer.

Layer	diameter / mm	thickness / µm
Ni/YSZ anode support	20	400
8-YSZ electrolyte	20	3
CGO barrier layer	20	3
LSC cathode	12.5	12

4.5.2 Test procedure

After the cell was successfully mounted with the cathode side up, the assembled *ProboStat* was heated up to 1000 °C with a ramp rate of 1.2 K/min. The cell was already almost gas-tight but there was still a small leak. Thus, the temperature was raised to 1060 °C with 1 K/min and the gas-tightness test was repeated. As no more leakage could be found, the cell was cooled down to 800 °C with 2.5 K/min.

Now for the reduction of the anode, pure H_2 (2 mg/min) was streaming to the anode, which resulted in an abrupt rise of the OCV to 900 mV. Shortly afterwards the voltage rapidly dropped to 200 mV and remained stable at this low level. After the hydrogen feed was turned off, the voltage again increased to 900 mV and was then slightly decreasing. H_2 was once again supplied to the cell, which first led to a voltage rise of 100 mV for less than a minute. Afterwards, the OCV rapidly declined again to 200 mV. The same behaviour of the OCV was observed several times in the same order. Furthermore, it was determined that small amounts of gas were flowing from the inner chamber to the outer chamber, but not

in the reverse direction. Possible causes may be a very small crack owing to the fast reduction of the anode, or a problem with the outer current collector which could probably be in contact with the gold gasket, which would lead to a short circuit of the cell. In order to investigate the problems emerged, the cell was cooled down with 1 K/min to ambient temperature. The disassembling revealed that there was no contact between the outer current collector and the gold gasket. The anode was completely reduced and did not exhibit unreduced areas. Figure 31 demonstrates the optical differences between the oxidised and the reduced anode.

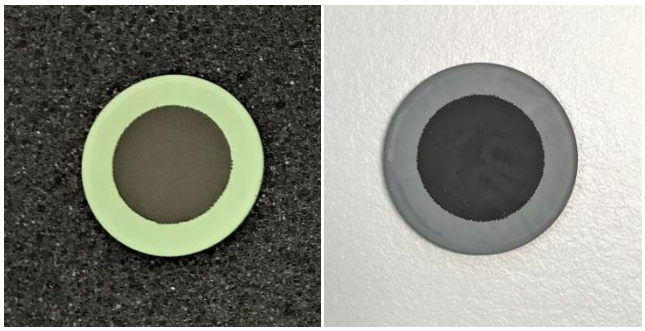

Figure 31: Cell 3, fresh (left) and reduced (right).

4.5.3 X-ray diffraction (XRD)

The reduced button cell was then analysed with X-ray diffraction (XRD) using a Bruker D8 Advance over an angle range from 10° to 100° (2θ). A fresh and unreduced reference cell was also examined. While the fresh cell consisted of the expected phases (LSC64, YSZ, CGO, NiO), different phases were found in the reduced sample. Especially La-Co oxides and other oxides, but no LSC, were discovered. This suggests that hydrogen leakage from the anode to the cathode compartment led to decomposition of the cathode material, which resulted in the total failure of the cell.

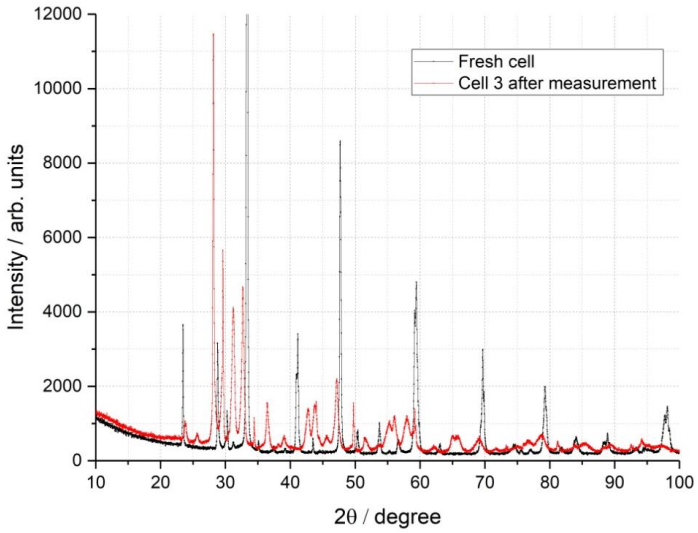

Figure 32: XRD-pattern of the cathode side of Cell 3.

4.5.4 Scanning electron microscopy (SEM)

Additionally, a SEM analysis was performed to determine the microstructure and the composition of the different layers of the cell. The following four layers could be identified by means of Z-contrast in backscattered electron mode:

(1) Porous LSC/CGO composite cathode, thickness 14 µm
(2) Thin porous CGO diffusion barrier, thickness 2 µm
(3) Densely sintered YSZ electrolyte, thickness 2 µm
(4) Porous Ni/YSZ anode functional layer and support, thickness 400 µm

Unlike Cell 1 and Cell 2, there is no current collector layer on top of the cathode in Cell 3. As specified in the manufacturer's data, gadolium-doped ceria (CGO) is used as material for the diffusion barrier. EDX analysis verifies the presence of the layer compounds listed in Table 3. In a rough estimation made with EDX, the ratio of La:Sr is 2:1 and the one of (La+Sr):Co is 1:1, respectively.

The determined thicknesses of the layers correspond to the values stated by the manufacturer. As there is no need for a cathodic current collector due to the high electronic conductivity of LSC, the respective layer in Cell 3 is thinner than the LSM/SDC cathode and LSM current collector layers in Cell 2. In contrast, the anode is thicker and more porous than the one of the cells with LSM cathodes. The high porosity might be the reason why large amounts of H_2 could diffuse through the anode layer to the air side and further decomposed the electrode material. Furthermore, there is an anode functional layer (12 µm) with a higher percentage of YSZ and lower porosity at the anode section next to the electrolyte. The chemical reaction takes place in this section of the anode layer. In general, anode functional layers have similar layer thickness and porosity as cathode layers in anode-supported cells. Impurities cannot be found by EDX, neither on the anode nor on the cathode side.

Figure 33 (c) reveals the very high porosity at the boundaries of the cell. The cell is slightly delaminated from the gold gasket in the outer area but as there is a contact between the cell and the gasket in the inner areas, delamination can be excluded as a reason for the strong H_2 diffusion through the cell.

(a)

(b)

(c)

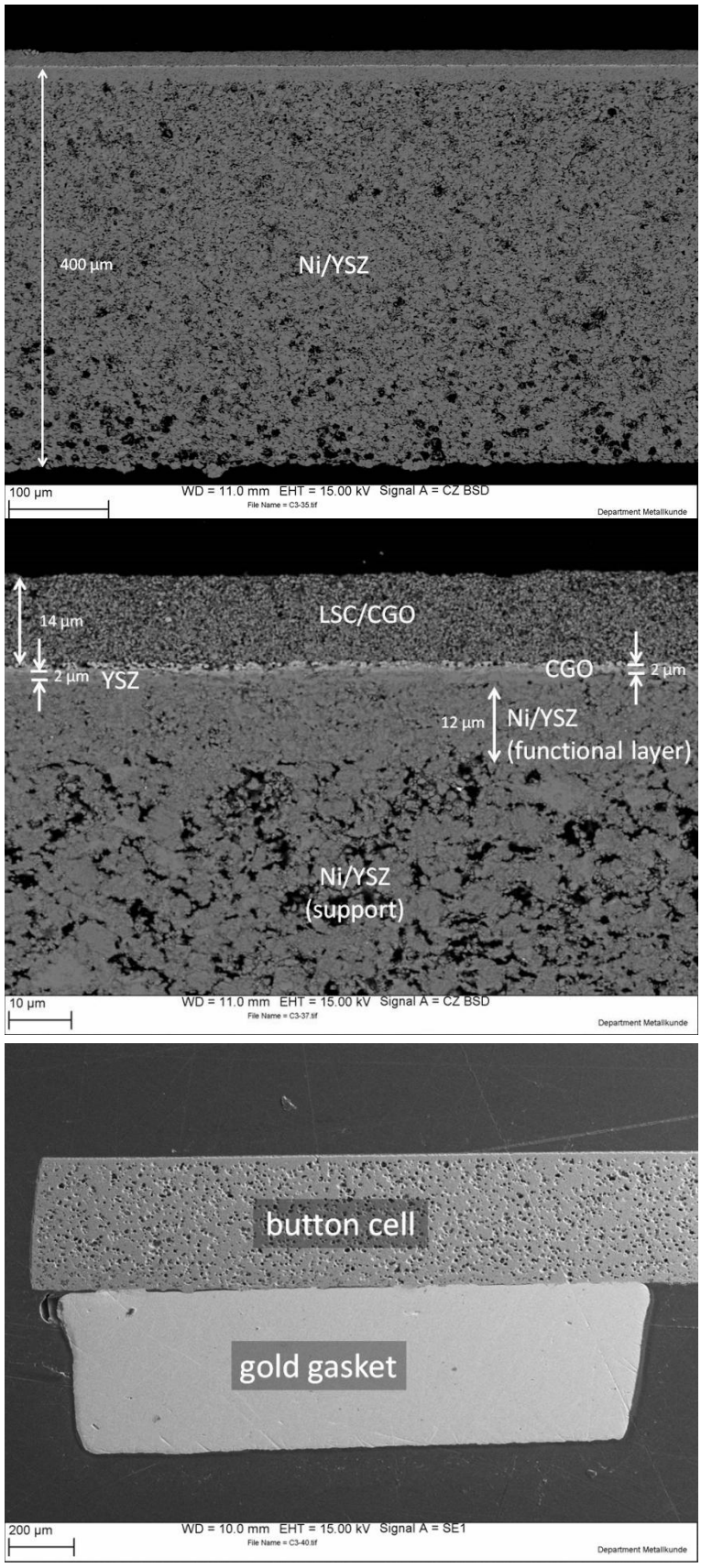

Figure 33: SEM-BSE images of a cross section of Cell 3 showing (a) the whole cell, (b) a magnified region with cathode, diffusion barrier and electrolyte layers, (c) SEM-SE image of the cell boundary with the gold gasket.

4.6 Cell 4 (LSC)

No cell tests could be performed with Cell 3 due to the problematically high hydrogen diffusion across the anode layer towards the cathode. In order to check if it was just a single failing button cell, a second similar cell with LSC cathode was mounted in the same way in the *ProboStat*. The description of the fresh cell can be found in section 4.5.1.

4.6.1 Test procedure

After assembling, Cell 4 was heated up to 1050 °C applying a ramp rate of 1.2 K/min. The gas-tightness test indicated no leakage, neither inside out, nor outside in. For this reason the temperature was not raised to 1060 °C, but directly decreased with 2.5 K/min to the reduction temperature of 800 °C. Another test confirmed that the cell is gas-tight.

The reduction was performed in the same way as for the previous button cells. Pure H_2 (2 mg/min) was supplied to the anode and after a few minutes the OCV rapidly increased. After the OCV had gone above 1 V, it quickly dropped to 200 mV. In this way the behaviour of the cell resembles that of Cell 3. As gas leakage was once again not found, it seemed that H_2 could diffuse from the inside out and reacted with O_2 in the outer gas chamber. If less O_2 was supplied to cell, the OCV further decreased to a level of less than 100 mV while a higher O_2 feed increased the voltage up to a maximum of 800 mV. To rule out the possibility of a tightness problem at the gold gasket, the temperature was again raised to 1050 °C. With this approach, the idea was to seal the reduced cell once again because the reduction might have led to shrinkage of the cell and thus detached the gold sealing from the cell. After the temperature of 1050 °C was reached, the cell was not gas-tight anymore. A temperature peak at 1054 °C was recorded at the cell, which indicated a local exothermal chemical reaction between hydrogen and oxygen. Next, the temperature was raised to 1060 °C, which at first seemed to boost the OCV. But after the temperature had increased up to 1067 °C for a short time, the voltage dropped significantly. It seems that the gold gasket has molten due to the fact that the entire gas left through the outlet gas line where no counter pressure was applied. In order to investigate what has happened, the system was cooled down to ambient temperature with a ramp rate of 2 K/min. A gas mixture of 3.7% H_2 in Ar was supplied to the fuel side of the cell while cooling down.

The disassembling of the *ProboStat* reveals that the gold gasket is completely molten and liquid gold has flown down the support tube where it re-solidified owing to the lower temperature in this part of the system. The cell is firmly sintered to the support tube, thus it is not possible to remove it from the tube without breaking off parts of the cell. The anode is re-oxidised to a large part, which is indicated by the deep green colour of the anode substrate. Only the small metallic grey spot in Figure 34 (left), where the H_2 left the capillary tube, still consists of reduced Ni. The cell does not show continuous cracks throughout the cross section, there are just small circular cracks visible on the outer part of the cell. The cathode faded from a deep black to a dark grey colour. XRD and SEM

analyses are performed to obtain more detailed information of what had happened to the cell.

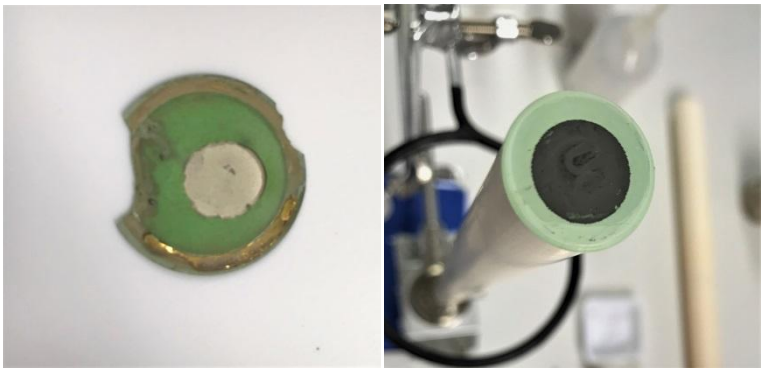

Figure 34: Cell 4 after disassembling with re-oxidised anode (left) and cathode (right).

4.6.2 X-ray diffraction (XRD)

The results of the XRD analysis of Cell 3 clearly prove the decomposition of the cathode in reducing atmospheres. As Cell 4 is re-oxidised it is interesting to find out which compounds can be found now. Despite of a small peak shift to smaller angles, there is hardly any deviation between the fresh and the re-oxidised cell. It is possible that the cathode first reacted with H_2 to secondary phases. But as after the melting of the gold gasket the H_2 gas flow was strongly decreased, there was enough oxygen for the reaction with the diffused hydrogen. As a result, re-oxidation at the cathode presumably took place and the initial composition of the cathode was reconstituted.

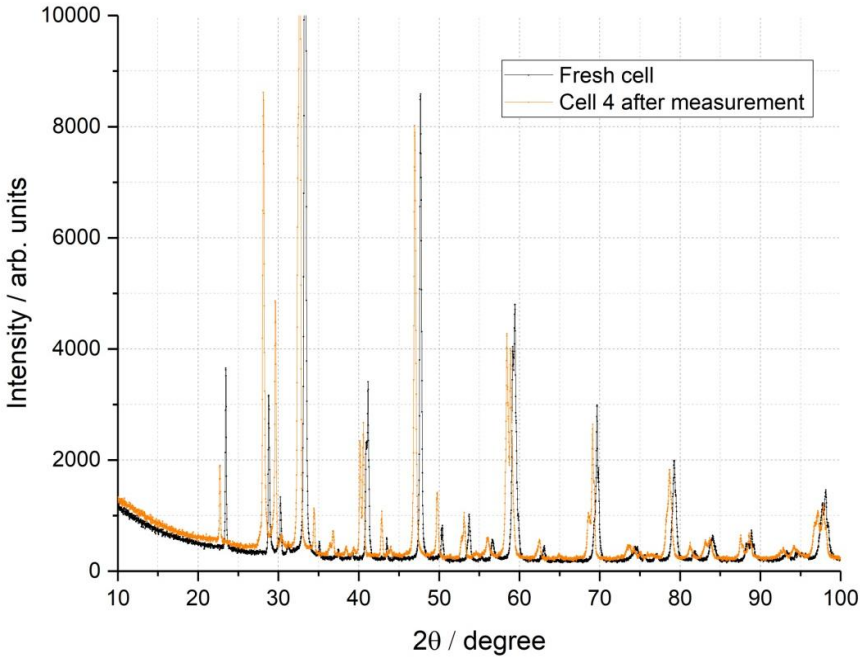

Figure 35: XRD-pattern of the cathode side of Cell 4.

4.6.3 Scanning electron microscopy (SEM)

In order to compare the microstructure of a reduced and a re-oxidised cell, Cell 4 is further analysed with SEM. As Cell 3 and Cell 4 are equal cell types, the identified layer thicknesses of Cell 4 are more or less equal:

(1) Porous LSC/CGO composite cathode, thickness 11 µm
(2) Thin porous CGO diffusion barrier, thickness 2 µm
(3) Densely sintered YSZ electrolyte, thickness 2 µm
(4) Porous Ni/YSZ anode functional layer and substrate, thickness 400 µm

The analysis using SEM gave very interesting information about the microstructure of the cell. Coarsening of the anode microstructure occurred, which can be interpreted as a result of the re-oxidation. In our case the grain growth resulted in a complete delamination of the anode from the other cell layers which caused the failure of the cell [46]. The crack runs along the entire interface between the anode and the thin YSZ electrolyte and CGO diffusion barrier, respectively. Figure 36 (a,b) depicts the detachment of the anode caused by high mechanical stresses. Investigations of different powders showed that fine NiO and YSZ particles exhibit better electrical and mechanical properties than coarser ones [51]. Even if there had been no delamination, a re-oxidation of the anode would have resulted in a failure of the cell due to highly increased pores (loss of percolation).

The molten gold diffused in high quantities into the anode layer, which is illustrated in Figure 36 (c). The gold is identifiable by the bright spots inside the white marked area. With the exception of gold, no further impurities could be found in Cell 4 by means of EDX-analysis.

(a)

(b)

(c)

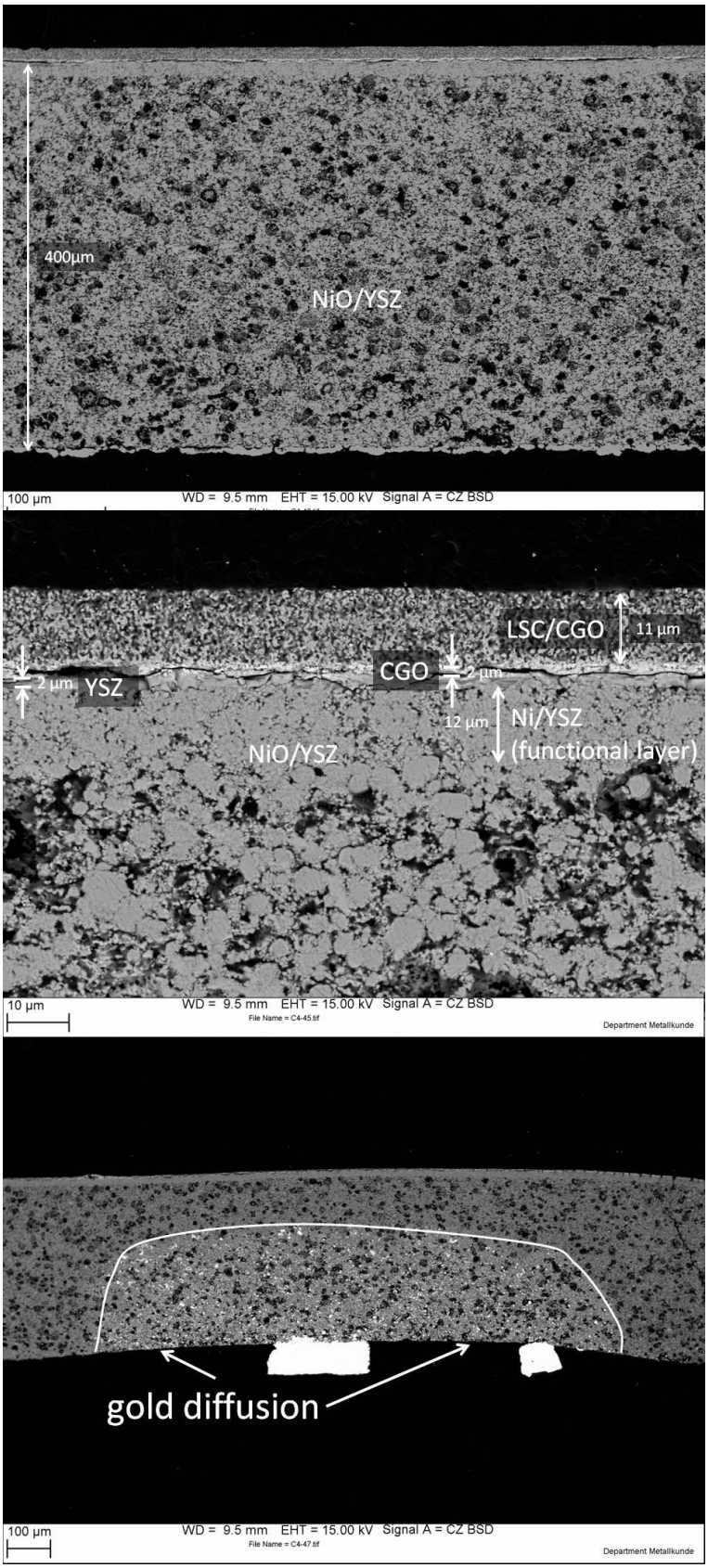

Figure 36: SEM-BSE images of a cross section of Cell 4 showing (a) the whole cell, (b) a magnified region with cathode, diffusion barrier and electrolyte layers, (c) gold diffusion into the porous anode.

4.7 Cell 5 (LCF82)

After two unsuccessful attempts to perform measurements of Cell 3 and Cell 4, the next button cell to be tested is the first with a cathode manufactured in-house (Chair of Physical Chemistry, Montanuniversitaet Leoben).

4.7.1 Description of the cell

The cell consists of a Ni/YSZ anode substrate from Fuel Cell Materials with a YSZ electrolyte and a CGO interface to avoid zirconate formation. According to the manufacturer it is especially designed for the use with perovskite cathodes [52]. In this case a layer of $La_{0.8}Ca_{0.2}FeO_{3-\delta}$ with a diameter of 10 mm was screen printed (55T screen) on the half cell and sintered for 2 h at 1000 °C in air with heating and cooling rates of 3 K min^{-1}.

4.7.2 Test procedure

Cell 5 was successfully mounted with the SOFC cathode side up in the *ProboStat* and heated up to 1000 °C with a ramp rate of 1 K/min. The cell did not show any leakage at this temperature, nevertheless it was raised to 1050 °C with 1 K/min to ensure the gas tightness. As the cell was still gas-tight it was cooled down to the testing temperature of 800 °C with a ramp rate of 2.5 K/min. The first records of the OCV revealed a very strong and unsteady oscillating between 100 mV and 800 mV. It turned out that there was no electrical continuity between the contacts of the outer current collector (WE and RE-). After the system had cooled down with 2.5 K/min to ambient temperature, a broken wire was identified as the reason. For the next assembling, a new outer platinum electrode was applied.

As the cell has already sintered with the gold sealing, the renewed attempt to mount the cell was unproblematic. The *ProboStat* was heated up to 800 °C with 1 K/min. It was not necessary to further increase the temperature due to the fact that the system was already gas-tight. It can therefore be concluded that a good contact between the gold gasket and the cell is essential for the gas-tightness of the whole system.

The next step was to slowly reduce the anode by increasing the H_2 content of the fuel feed step by step. The gas composition and the applied gas flows during the reduction are shown in Table 4. The cumulative time in the very right column of the table gives information about the duration of each reduction step starting from zero at the moment when H_2 was supplied to the cell for the first time. The reduction process was completed after eight hours exhibiting an OCV of 910 mV in pure H_2 (1 mg min^{-1}).

Table 4: Gas composition and mass flows for the fuel feed applied during the reduction process of Cell 5 at 800°C.

H_2 / vol%	H_2 / µg min^{-1}	Ar / vol%	Ar / mg min^{-1}	cumulative time / min
4	80	96	38.5	0
10	215	90	38.5	209
20	378	80	30	303
40	1000	60	30	366
70	1000	30	8.5	424
100	1000	0	0	476

The low OCV might indicate strong hydrogen diffusion as it could already be observed with Cell 3 and Cell 4. To validate this assumption, the gas flows on both the fuel and the air side were varied. A higher H_2 flow of 1.5 mg min^{-1} led to a lower OCV of 750 mV at constant O_2/Ar flow of 25 ml_n. When the H_2 feed was stopped, the OCV quickly increased. A change of the O_2/Ar flow affected the OCV to a lesser extent than the H_2 feed. On the one hand, the gas-tightness test revealed gas leakage from the inside out. On the other hand, the cell was absolutely gas-tight from the outside in. Thus it appeared that the hydrogen could diffuse through the anode layer to the air side. Higher H_2 flow rates caused higher hydrogen diffusion and resulted in a lower OCV as the hydrogen reacted with the oxygen on the fuel side. In addition, water condensation at the gas outlet on the air side verified this assumption.

It seems that the anode substrate of Cell 5 is the same as the one used for Cell 3 and Cell 4 due to the fact that similar hydrogen diffusion was observed. The only difference is that the OCV of Cell 5 does not completely drop and keeps constant between 910 mV and 925 mV over longer periods at gas flow rates of 1 mg min^{-1} (11.1 ml_n) H_2 and 25 ml_n 20% O_2/Ar. For that reason it was possible to perform the tests described in the following chapter.

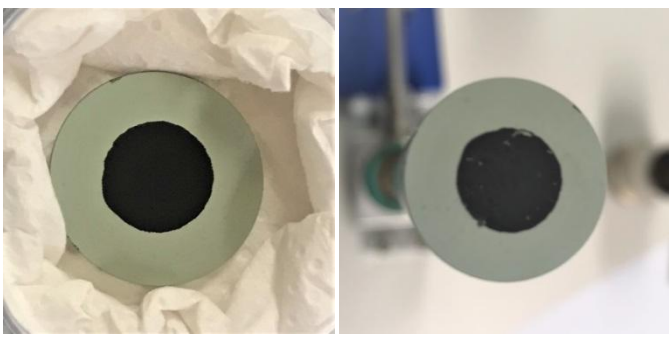

Figure 37: Cell 5, fresh (left) and reduced (right).

4.7.3 Results

A variety of impedance spectra is presented in Figure 38 at different temperatures. As expected, the series resistance R_s and the polarisation resistance R_p increase when lowering the temperature. Moreover, degradation clearly takes place when comparing the measurement results on day 1 with the ones on day 6. Again, R_s and R_p strongly increase within five days. After the tests in dry H_2 on the fuel side had been performed, the *ProboStat* was thermally isolated and 10% H_2O was added to the fuel feed. As it has already been demonstrated in the tests of Cell 2, the presence of water leads to a reduction of the cell resistance. Especially the polarisation resistance declines in humid atmospheres. The measurements recorded on the following day (day 8) show a huge rise of R_p with 10% H_2O as well as in dry H_2. Moreover, the OCV slightly decreases from 890 mV to 880 mV. It is possible that the long-term hydrogen diffusion through the anode has already harmed the cathode and thus causes deterioration of the material properties of the cell. In comparison with the fresh cells, the ASR of Cell 5 is lower than the ones of the LSM cells. However, degradation effects are more pronounced in the tests with the LCF82 cathode.

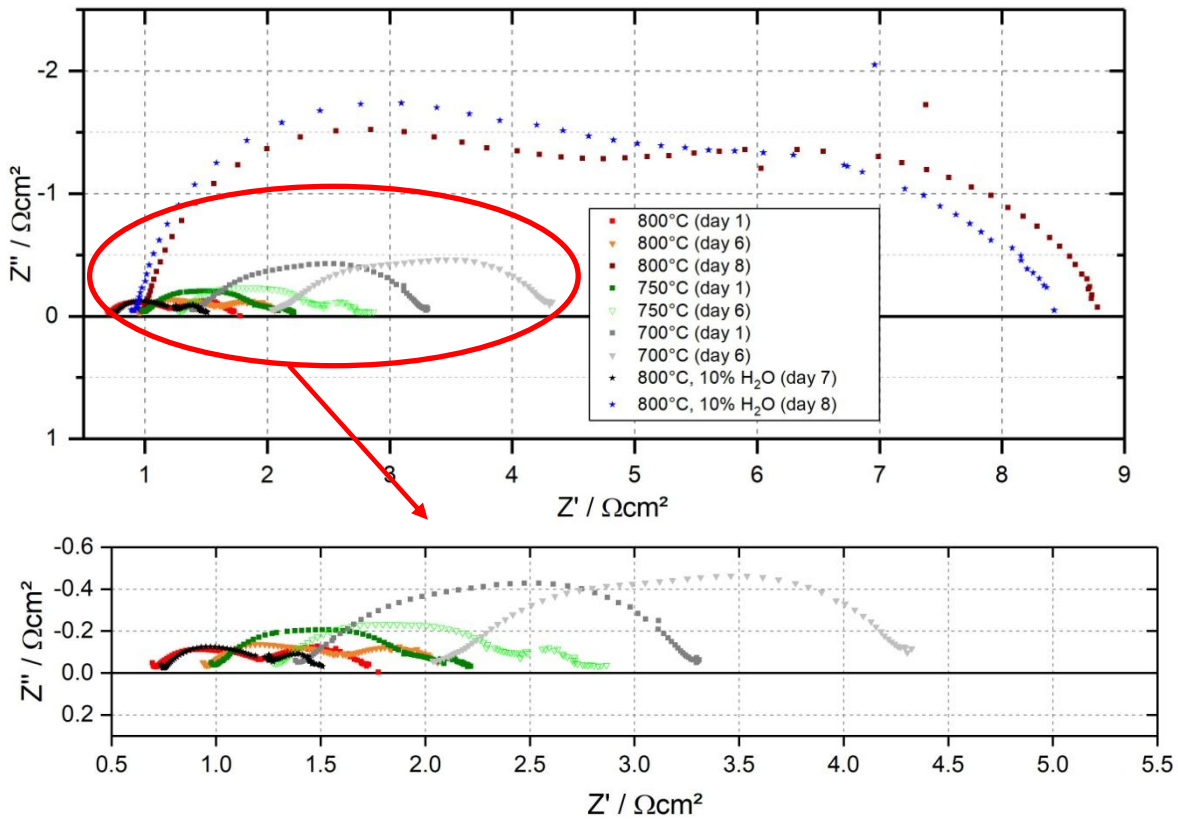

Figure 38: Impedance spectra illustrating degradation effects of Cell 5 at various temperatures.

Current-voltage characteristics are recorded comparing the performance of the fuel cell at different temperatures and observing degradation effects. The variation of the

temperature is depicted in Figure 39. The performance of the cell is insufficient at all temperatures as only low current densities can be applied while staying within a reasonable voltage range. The performance of the cell improves at higher temperatures. The OCV increases at higher temperatures according to the Nernst equation, while it declines with time due to the worsening gas-tightness of the cell. I-U characteristics acquired at the same temperatures at different times show the degradation of the cell.

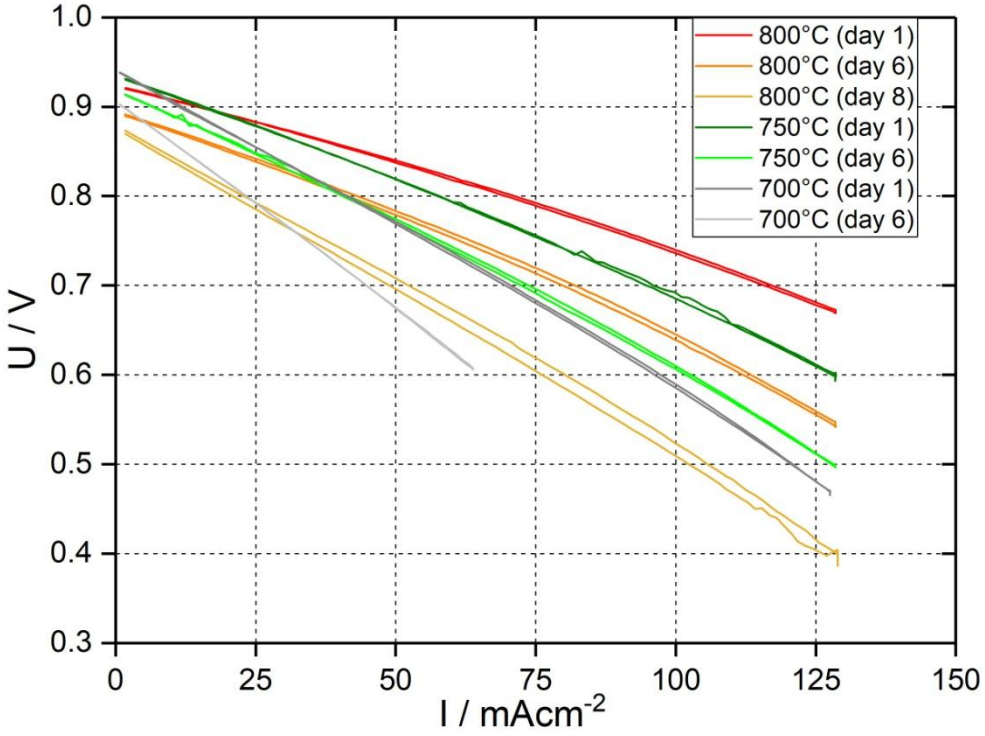

Figure 39: Current-voltage characteristics of Cell 5 at different temperatures showing time-dependent degradation.

Figure 40 depicts the influence of H_2O in the fuel feed in SOFC and SOEC operation mode. To compare the curves recorded in humid atmosphere, the benchmark tests for SOFC mode (red and orange curve) are also drawn in the figure. There is just a small difference between the curves recorded at 10% and 20% H_2O on the same day. The performance in SOEC operation does not reveal large deviations at the applied small current densities. Surprisingly, the measurement at higher humidity in SOFC mode shows better performance than at lower humidity. On the following day the performance of Cell 5 deteriorates considerably. The steeper slope of the curve corresponds to the increasing cell resistance displayed in Figure 38.

All measurements of Cell 5 are performed at a low OCV caused by significant H_2 diffusion through the anode layer to the air side. Therefore, it is not possible to evaluate the performance of the LCF82 cathode material, as the OCV was different at the benchmark tests with LSM cells. The denser anode microstructure had impeded H_2 cross-over. There are three possible solutions to run tests with button cells consisting of the more porous

anode layers. The first possibility is to mount the cell with the SOFC anode side up. In this case, the electrolyte prevents the hydrogen diffusion to the inner chamber (air side) of the *ProboStat*. Second, gold paste could be annularly applied on the support tube and on the outer edge of the cell. As a third option, electrolyte-supported cells (ESC), where hydrogen diffusion should not be a problem, could be used.

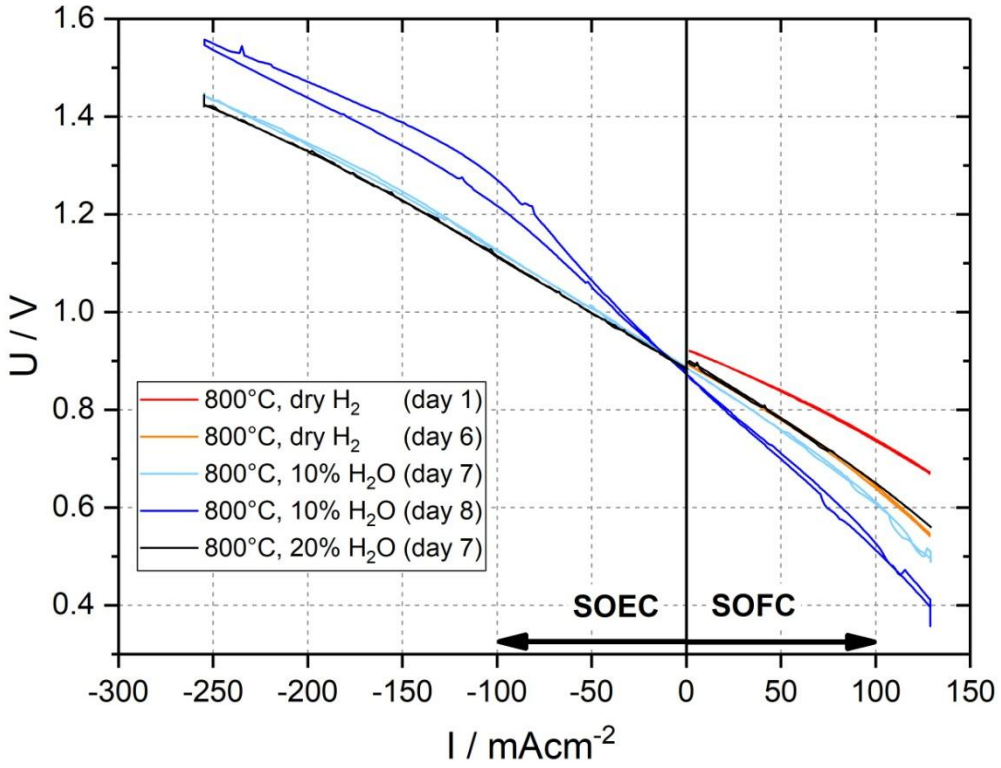

Figure 40: Current-voltage characteristics of Cell 5 at 800°C in dry and humidified H_2 vs. 20% O_2/Ar.

4.7.4 Scanning electron microscopy (SEM)

The tested and embedded button cell was analysed with SEM in order to determine the layer thicknesses and microstructures with special focus on the LCF82 layer. As expected, four different layers could be identified:

(1) Porous LCF82 cathode, thickness 15 µm
(2) Thin porous CGO diffusion barrier, thickness 4 µm
(3) Densely sintered YSZ electrolyte, thickness 6 µm
(4) Porous Ni/YSZ anode substrate, thickness 561 µm

Figure 41 shows that the microstructure of the SOFC cathode is porous and very homogeneous. For all button cells with LCF82 air electrode (Cell 5, 8 and 9) a 55T (meaning 55 threads per cm) screen was applied for screen-printing. The resulting layer thickness after sintering is 15 µm which is in the estimated range. Figure 41 (a) demonstrates that the cathode thickness is not uniform which can be seen in the lower

right corner of the picture where the layer is almost twice as thick. Moreover, the LCF82 layer is completely delaminated from the diffusion barrier over the entire diameter of the cell. Since serious problems with H_2 diffusion occurred during the cell tests, a reaction of hydrogen with the air electrode could be one possible reason for delamination. No signs of detachment are observed between all other cell layers.

In contrast to the assumption mentioned earlier, the Ni/YSZ anode support differs from the one of the LSC cells. Here, the layer thickness was determined as 561 µm, which is significantly thicker than the anode support of the LSC cells (400 µm). Furthermore, the anode support consists of a homogenous microstructure without a functional layer. No impurities are detected in any layer by EDX.

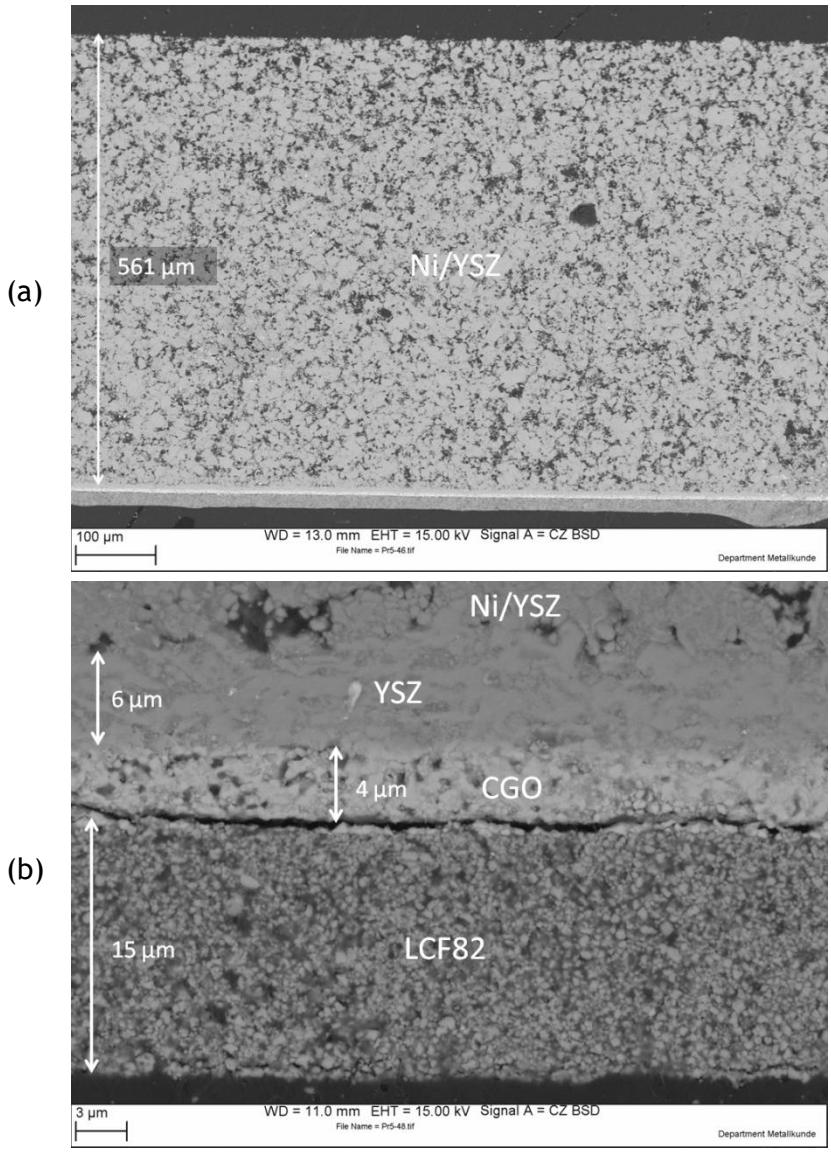

Figure 41: SEM-BSE images of a cross section of Cell 5 showing (a) the whole cell, (b) a magnified region with cathode, diffusion barrier and electrolyte layers.

4.8 Cell 6 (LSC)

The aim of the tests performed with Cell 6 is to investigate the behaviour of the cell with LSC cathode mounted with the SOFC anode side up in order to prevent the problem of hydrogen diffusion through the porous anode. Turning over the cell also means that now the fuel feed rises through the bent silica tube to the fuel electrode. The presence of H_2O leads to enhanced gas phase transport of volatile Si-compounds which can contaminate the *ProboStat* setup, especially the outer compartment. This might be problematic as button cells should be mounted with the SOFC cathode side up in the *ProboStat*. Investigations revealed that Si-poisoning in humid atmospheres is a considerable problem when the cathode material $La_{0.6}Sr_{0.4}CoO_{3-\delta}$ (LSC) is used, because Si-deposition on the surface strongly decreases the surface exchange rate [53]. For this reason, the measurements described in this chapter are just performed in dry gas atmosphere. Cell 6 is the same type of button cell as Cell 3 and Cell 4 (see description of the cell in section 4.5.1).

4.8.1 Test procedure

After mounting the cell in the *ProboStat* with the fuel electrode side up, the cell was heated to 1000 °C with a ramp rate of 1 K/min. As the cell is already gas-tight, it is then cooled down to 800 °C with 2.5 K/min. The anode was reduced in a similar way to Cell 5. The hydrogen content in the fuel feed was slowly increased step by step, as shown in Table 5. The reduction process was completed after more than three hours.

Table 5: Gas composition and mass flows for the fuel feed applied during the reduction process of Cell 6 at 800°C.

H_2 / vol%	H_2 / µg min^{-1}	Ar / vol%	Ar / mg min^{-1}	cumulative time / min
4	80	96	38.5	0
10	215	90	38.5	47
20	485	80	38.5	92
40	1000	60	30	131
70	1000	30	8.5	159
100	1000	0	0	191

The gas-tightness test, performed after cell reduction, exposed a small leak from the outside in, thus H_2 could still diffuse in small amounts to the air side. But since the OCV was constant at 1.15 V, it was not considered to be a problem for further cell tests. The results presented in the next chapter were obtained applying a H_2 flow of 2 mg min^{-1} (22.2 ml_n) and a 20% O_2/Ar flow of 25 ml_n.

After cooling down the cell with a ramp rate of 1 K/min to ambient temperature, the anode exhibited a colourful pattern on the reduced Ni/YSZ anode (Figure 42 (left)). Hence,

Si-deposition was first suspected since existing literature has already revealed colour changes due to silicon poisoning [54]. However, EDX analysis of the anode contradicted this supposition since only Ni, Fe and O were found. The presence of Fe is surprising and could be explained by contaminated Ni powder, which was used for manufacturing the fuel electrode. However, since only 0.33 wt% Fe were found, this should have no effect on the anode performance. Interestingly, neither yttrium nor zirconium could be detected. Moreover, the black colour of the cathode has faded to grey, as it can be seen in Figure 42 (right). XRD indicated platinum deposits, but it could not be clearly demonstrated. Furthermore, small amounts of CoO were identified in addition to the expected compounds (LSC, YSZ, CGO, Ni).

Subsequently, the bent silica tube was substituted by a thin-walled straight alumina tube in order to allow tests in humid atmospheres. As the anode re-oxidised during heating, it was not possible to achieve further results with Cell 6. Figure 42 (middle) shows the green re-oxidised NiO/YSZ anode placed on the support tube. The colourful pattern has largely disappeared after re-oxidation.

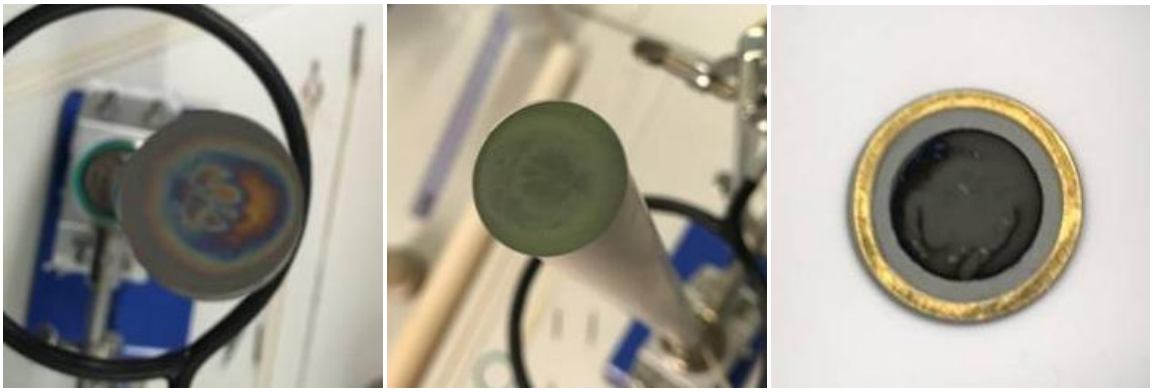

Figure 42: Reduced anode (left), re-oxidised anode (middle) and cathode (right) of Cell 6 after disassembling.

4.8.2 Results

The impedance plot in Figure 43 displays the recorded spectra at five different temperatures. At higher temperatures, the series resistance R_s and the polarisation resistance R_p decrease. The semicircles can be better separated at lower temperatures since they almost completely merge at higher temperatures. Three semicircles can be identified at low temperatures, where the small semicircle at high frequencies is poorly resolved. Compared to the cells discussed in the previous chapters of this thesis, Cell 6 has the lowest ASR at 800 °C.

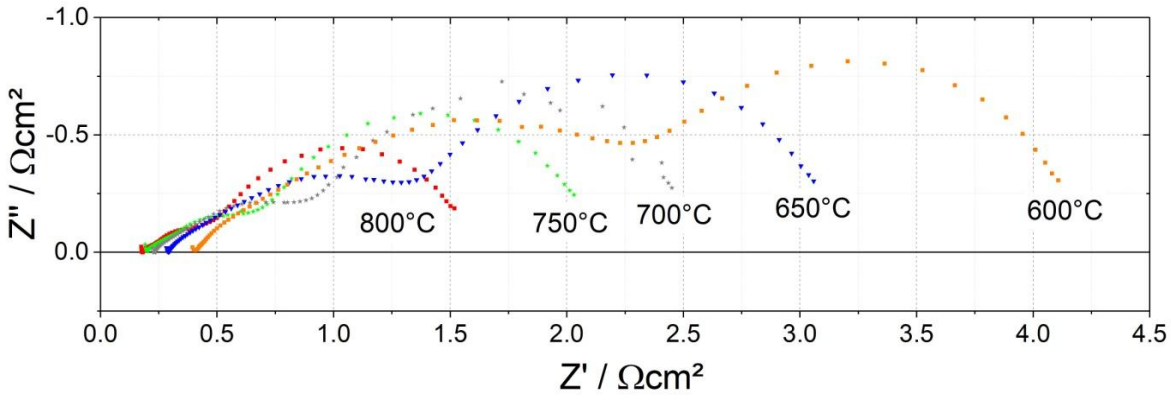

Figure 43: Impedance spectra of Cell 6 at various temperatures in dry H_2 vs. 20% O_2/Ar.

According to the results obtained from EIS, the performance of Cell 6 declines when lowering the temperature. As demonstrated in the current-voltage characteristics in Figure 44, there is a significant deterioration of the cell performance especially at 600 °C and 650 °C in SOFC operation. Compared to all other cells, much higher current densities could be applied since the slope of the characteristic curves is less steep due to a lower ASR. The steeper section of the curve at low current densities might indicate activation polarisation. The small hysteresis occurring in the measurements is caused by accumulation of H_2O in the outer chamber owing to higher water production at higher current densities. This leads to a lower voltage with decreasing current density after the maximal current density was reached.

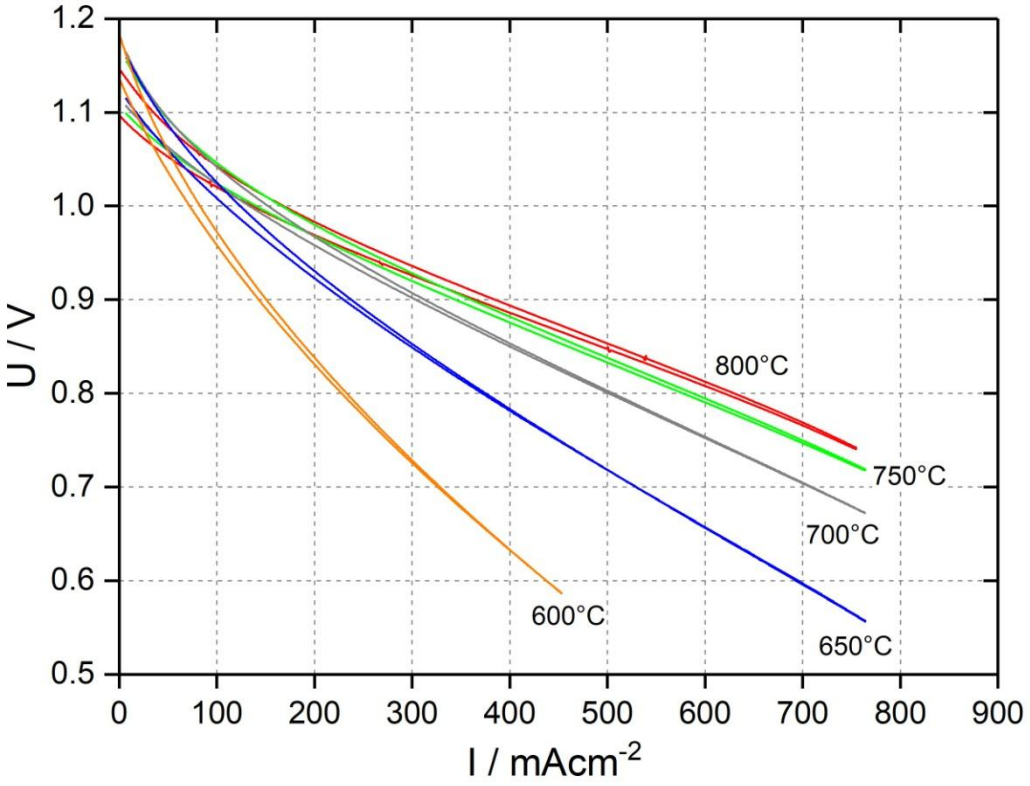

Figure 44: Current-voltage characteristics of Cell 6 at different temperatures in dry H_2 vs. 20% O_2/Ar.

4.9 Cell 7 (LSC)

Another button cell (denoted as Cell 7) with LSC cathode was mounted in the *ProboStat* since it was not possible to perform tests with Cell 6 in humid atmospheres. The data of this cell type can be found in section 4.5.1. In these test series, a thin-walled straight alumina pipe was used as riser for the fuel feed in all measurements. A resistive heating cord was applied for the first time in these tests in order to avoid undesirable water condensation at the gas outlets.

4.9.1 Test procedure

After the assembling of the *ProboStat*, the cell was heated up in Ar on the fuel side to 1000 °C with a ramp rate of 1.5 K/min. The air flow (20% O_2/Ar) was 25 ml_n throughout the entire time of testing. As no gas leakage could be identified, the temperature was decreased to the testing temperature of 800 °C with 2.5 K/min. The system was still gas-tight at this temperature. As the stepwise reduction of the anode had proven to be advantageous in the previous tests, it was also applied for Cell 7. First, a gas feed of 4% H_2 in Ar was supplied to the anode. More and more Ar was then substituted by H_2, as it is set out in Table 6.

Table 6: Gas composition and mass flows for the fuel feed applied during the reduction process of Cell 7 at 800°C.

H_2 / vol%	H_2 / µg min^{-1}	Ar / vol%	Ar / mg min^{-1}	cumulative time / min
4	80	96	38.5	0
10	215	90	38.5	26
20	385	80	30	71
40	1000	60	30	97
70	1000	30	8.5	147
100	2000	0	0	239

The hydrogen content was further increased after the OCV was found to be constant. For reasons of time saving, the increase from 10% to 20% H_2 was carried out while the voltage was still slowly rising. However, this should not adversely affect the cell as long as the intervals between increasing the H_2 content are long enough. Finally, the reduction process was completed after almost 4 hours at an OCV of 1.133 V. A timeline depicts the rise of the OCV with increasing hydrogen contents in Figure 45.

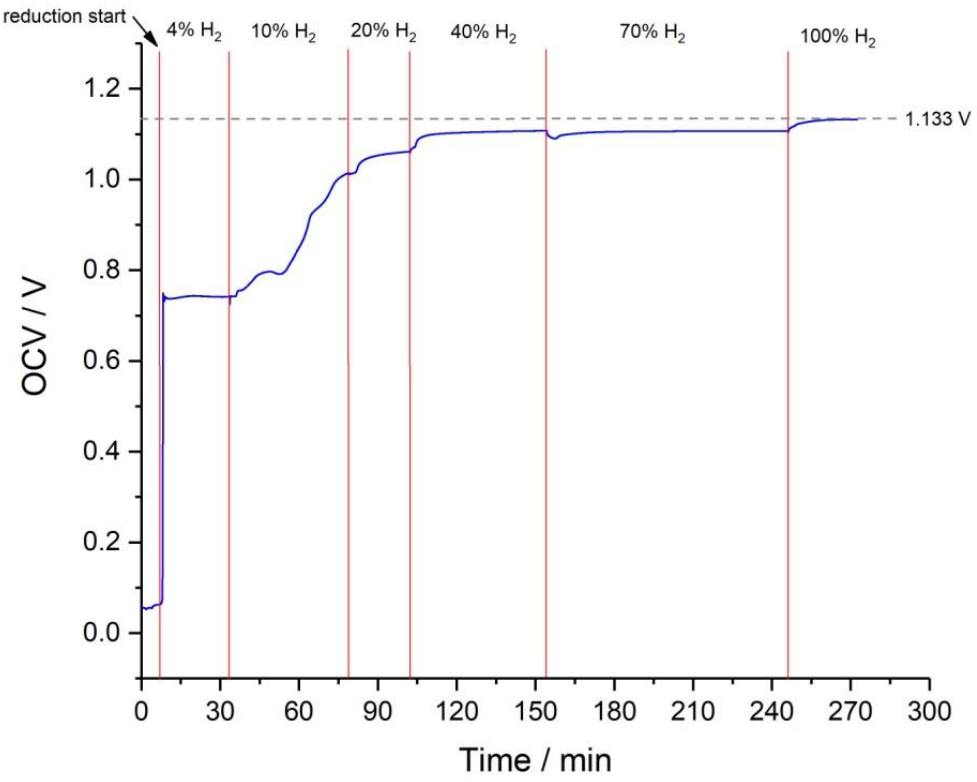

Figure 45: Reduction process of Cell 7 at 800°C.

4.9.2 Resistive heating cord

The previous tests in humid gas atmospheres on the fuel electrode side exhibited problems with water condensation and vaporisation at the gas outlet of the *ProboStat*. The temperature at the inside of the gas outlet tube depends on the heating of the top box, but if the 8 V chip is used in the heat unit, the temperature does not exceed 70 °C. Therefore it is not possible to keep the OCV constant at higher humidity which makes it difficult to obtain meaningful results.

In order to eliminate this problem, a controllable heating cord is used. Passing current through the resistive wire (nickel-chromium alloy) leads to heat production by ohmic heating. The total resistance of the wire with a length of 50 cm is 1028 Ω, thus voltages of approximately 100 V are necessary to attain sufficient heat output. A thermocouple is placed on the surface of the gas outlet pipe to measure the temperature. The results for Cell 7 are obtained while applying a control temperature of 200 °C to 250 °C. These relatively high temperatures are crucial to avoid condensation in all parts of the gas pipe owing to the fact that temperature measurements reveal cold spots not only at the gas outlet but also at tube sections inside the top box. A further increase of the temperature is not recommended due to additional material stresses. Moreover, the 9 V chip is used in the heat unit in order to increase the temperature inside the top box to 150 °C at high humidity levels. The I-U curve in Figure 46 demonstrates the improvement towards less oscillating behaviour due to additional heating of the gas outlet. In this case, a control temperature of 160 °C is sufficient to prevent water condensation at 40% H_2O. If higher water contents need to be applied in the investigations, the control temperature has to be further increased.

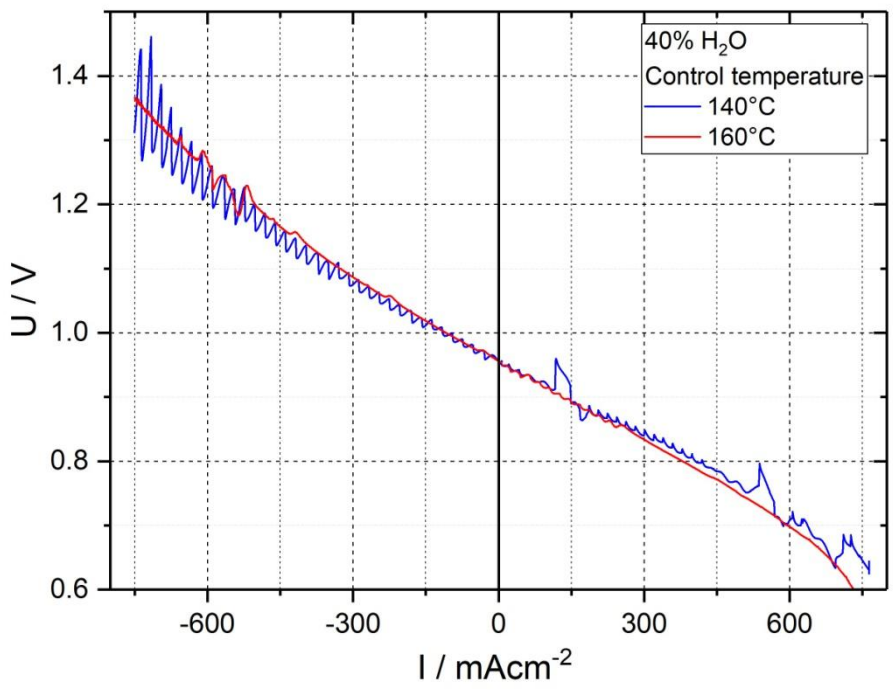

Figure 46: Effect of the control temperature of the gas outlet pipe surface on the current-voltage characteristics at 40% H_2O/H_2 vs. 20% O_2/Ar.

Water condensation mainly takes place at the gas outlet on the fuel side but it can also appear at the inlet section between the heated gas line and the top box of the *ProboStat*. It is therefore advisable to slightly heat and thermally insulate this part of the system as well. Figure 47 shows the mounted heating cord and the insulated gas outlet and inlet.

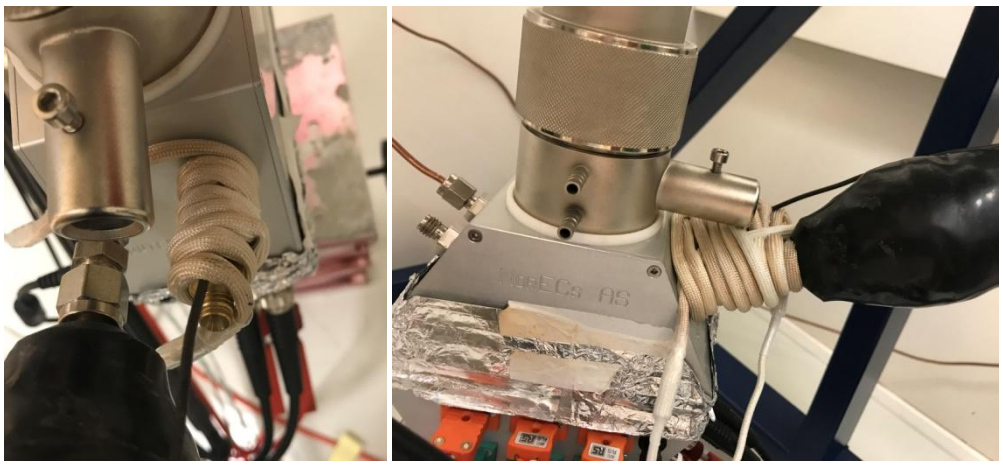

Figure 47: Heating cord mounted at the gas outlet (left), insulation of both the heating cord and the gas inlet (right).

4.9.3 Results

All tests were performed at 800 °C since a temperature variation for this cell type was already done with Cell 6. The button cell was exposed to different gas mixtures on the fuel side in order to set exact levels of moisture. Table 7 displays the applied mass flows at different H_2O contents.

Table 7: Mass flows of H_2 and H_2O in the fuel feed for different H_2O contents (Cell 7).

H_2O content / vol%	Mass flow H_2 / µg min^{-1}	Mass flow H_2 / ml_n	Mass flow H_2O / mg min^{-1}	Mass flow H_2O / ml_n
0	2000	22.2	0	0
5	2000	22.2	1	1.2
10	2000	22.2	2	2.4
20	2220	24.7	5	6.2
40	2000	22.2	12	14.7
50	1430	15.9	13	15.9
70	820	9.1	17	21.3
90	300	3.3	24	30.1

The impedance spectra in Figure 48 demonstrate the influence of water in the fuel feed. The polarisation resistance R_p strongly decreases in presence of H_2O on the fuel side, while the series resistance R_s increases in humid atmosphere. This characteristic is similar to the behaviour of Cell 2. In general, R_p declines with increasing humidity, with the exception of spectra recorded at 50% and 90% H_2O. It is expected that degradation affects the results since the *ProboStat* was operated for 400 hours with Cell 7. In contrast to R_p, the series resistance R_s is lower when dry H_2 is supplied. The effect of different H_2O contents on R_s is not clear, as degradation seems to have a high impact. However, the total ASR of the cell is low, especially when compared to button cells with LSM and LCF82 cathodes. In dry H_2, the semicircle at high frequencies is small compared to the one at low frequencies. Conversely, in high humidity, the semicircle at high frequencies is predominant.

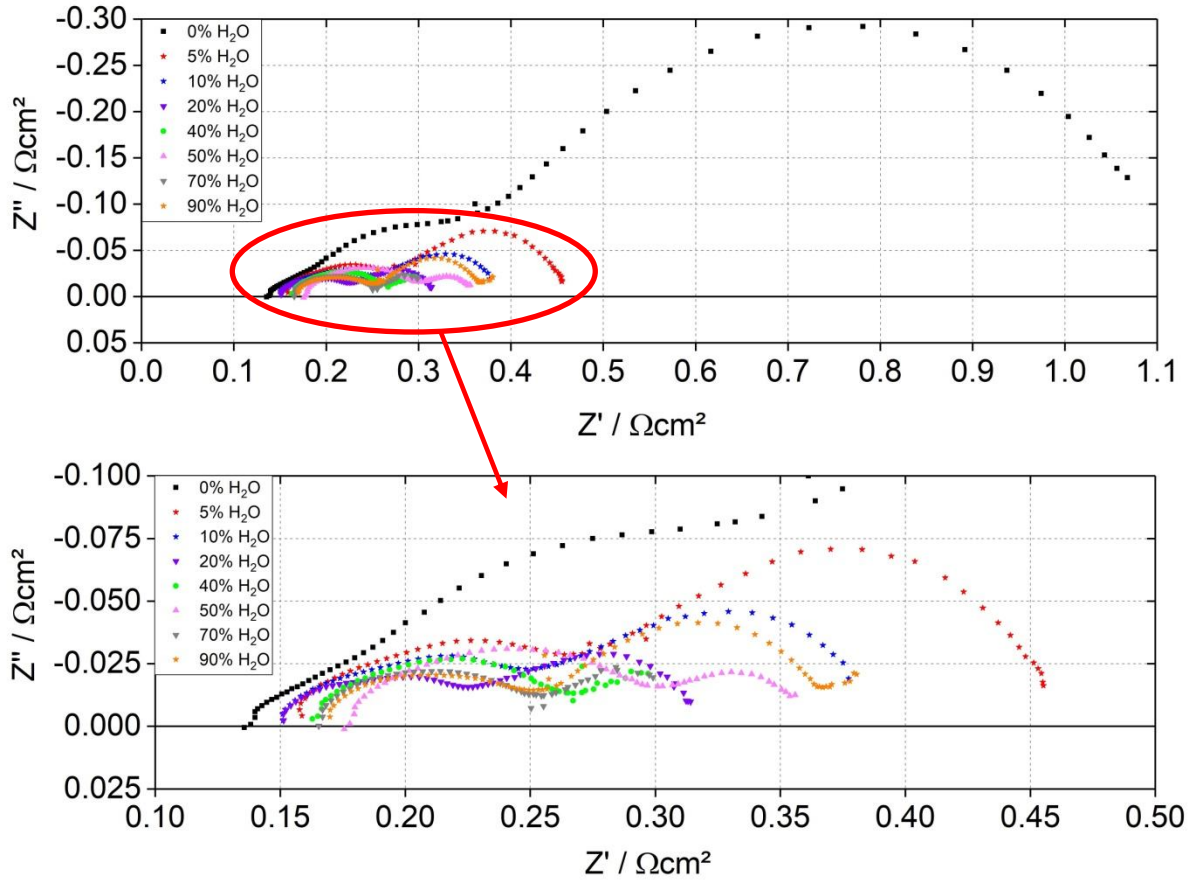

Figure 48: Impedance spectra of Cell 7 at 800° C at different H_2O contents.

The current-voltage characteristics of Cell 7 verify the low ASR gained from the impedance spectra as the cell exhibits good performance. In SOFC operation, high current densities of more than 900 $mAcm^{-2}$ are achieved without falling below 0.7 V for the measurements in dry H_2 and with H_2O contents up to 20%. For a humidity of more than 40%, the hydrogen supply is decreased in order not to exceed the recommended total gas flow of 30 ml_n according to the manufacturer's specification [43]. For this reason, it is not possible to attain the same high current densities. The average slope of the I-U curves with higher water content is only slightly steeper than the one recorded for pure H_2.

SOEC measurements are performed with a varying humidity between 20% and 90%. At lower moisture, H_2O starvation already occurs at low current densities. At 20% H_2O, the maximum attainable current density before starvation is 300 $mAcm^{-2}$. On the contrary, at a humidity of 70% and 90% very high current densities of more than 1100 $mAcm^{-2}$ can be achieved. All displayed measurements in electrolysis mode in Figure 49 are performed up to a maximum current density, where the linear characteristic of the curve changed. At this point, the steam conversion rate is about 50% in all SOEC measurements except from the one at 90% H_2O. It seems that there is already not enough H_2O available to run the electrolysis completely at this rate.

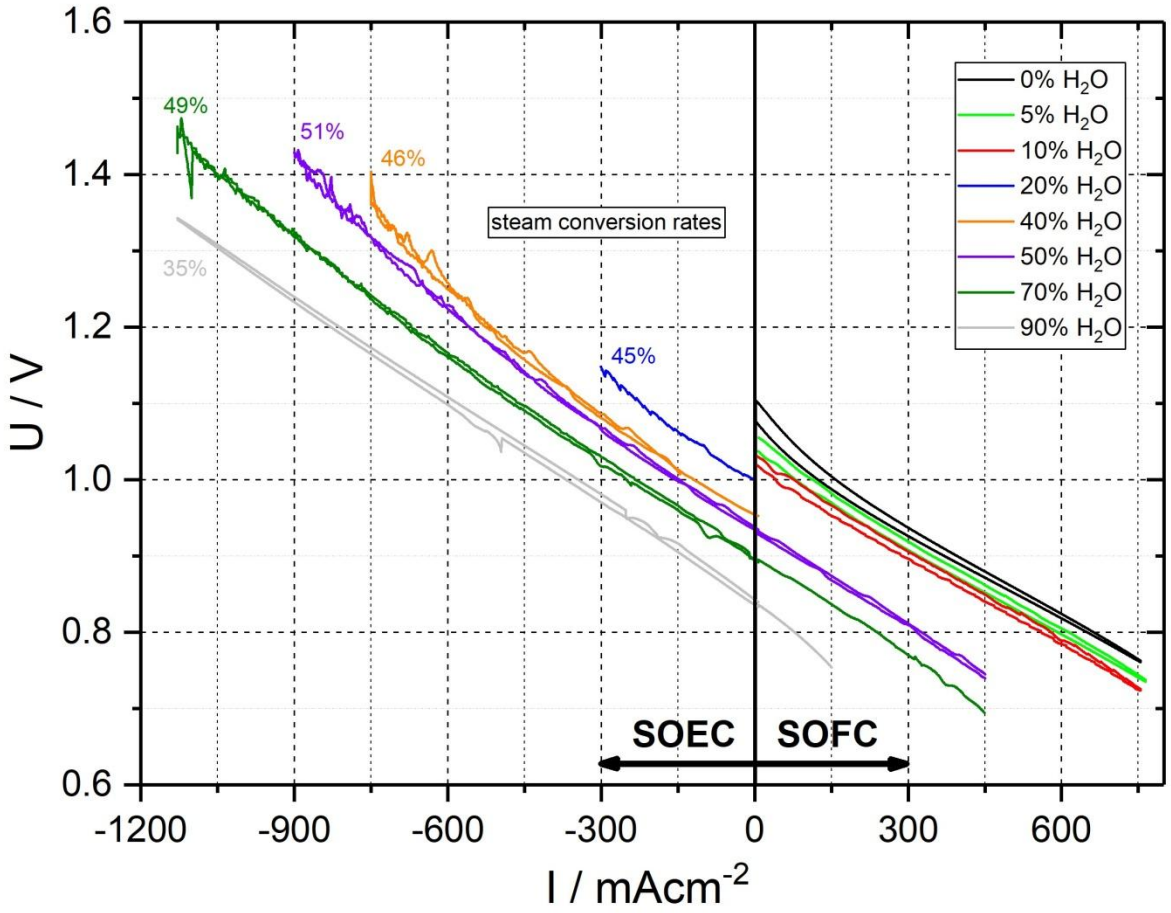

Figure 49: Current-voltage characteristics of Cell 7 at 800 °C at different H_2O contents in SOEC and SOFC operation modes.

It is noteworthy, that the OCV for all applied H_2O contents in the course of the test series of Cell 7 exactly corresponds to the Nernst voltage for this gas composition. This indicates that the cell is highly gas-tight and validates the good functioning of the experimental setup of the *ProboStat* system.

At low H_2O contents, the OCV is still slightly oscillating although water condensation can be excluded because of the heated gas outlets. In order to identify this problem, H_2 was substituted by Ar after all measurements had been performed. Here the risk is to re-oxidise the anode because of the low O_2 partial pressure of about 10^{-5} bar in the Ar feed. Shortly after Ar was supplied to the fuel side of the cell, the OCV drops rapidly to 695.2 mV and remains constant at this level. Increasing the humidity from 10% to 20% does not influence the OCV at all. According to the Nernst equation, the O_2 partial pressure (pO_2) on the fuel side can be calculated with:

$$p_{O_2}(II) = \exp\left(-\frac{OCV}{\frac{RT}{4F}} + \ln\left(p_{O_2}(I)\right)\right) = \exp\left(-\frac{0.6952}{\frac{8.3145 \times (273.15 + 800)}{4 \times 96485}} + \ln(0.2)\right) \quad (22)$$

$$= \mathbf{1.75 \times 10^{-14}}\ \boldsymbol{bar}$$

where $p_{O_2}(II)$ and $p_{O_2}(I)$ represent the O_2 partial pressures on the fuel and air side, respectively. R is the gas constant, T the test temperature and F the Faraday constant.

Thus, the measured O_2 partial pressure is much lower than the one expected of the Ar feed. This is due to the fact that oxygen is consumed to re-oxidise the Ni of the anode to NiO. The equilibrium pO_2 for Ni-NiO coexistence at 800°C has been thermodynamically calculated using the software FactSage 7.2 (Thermfact and GTT-Technologies). As it can be seen from Figure 50, the equilibrium pO_2 is 1.2×10^{-14} bar and thus very close to the partial pressure calculated with the measured OCV. Oscillation of the OCV does not occur anymore without supplying H_2 to the fuel side, which supports the hypothesis that H_2 provokes the high fluctuations of the OCV.

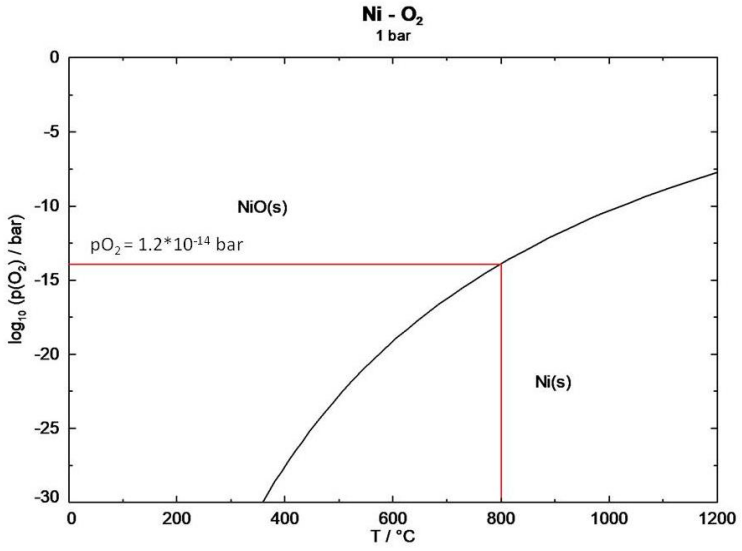

Figure 50: Equilibrium pO_2 for Ni-NiO coexistence as a function of temperature.

Disassembling reveals that the anode is indeed re-oxidised to a large part, as the green colour of the nickel oxide is also visible from the cathode side. This means that re-oxidation took place over the whole cross-section of the button cell. The small amount of oxygen in the supplied Ar is thus sufficient to almost completely re-oxidise the reduced anode. The tested cell is shown in Figure 51 after disassembling.

Figure 51: Cathode (left) and re-oxidised anode (right) of Cell 7 after disassembling.

4.9.4 Scanning electron microscopy (SEM)

Cell 7 was analysed with SEM in order to investigate the effect of slow re-oxidation of the anode. As the cell type is the same as for Cell 3 and Cell 4, the same four layers can be identified:

(1) Porous LSC/CGO composite cathode, thickness 14 µm
(2) Thin porous CGO diffusion barrier, thickness 1.5 µm
(3) Densely sintered YSZ electrolyte, thickness 3 µm
(4) Porous re-oxidised NiO/YSZ anode substrate, thickness 424 µm

It is remarkable, that the layer thicknesses deviate from those of the previously measured Cell 3 and Cell 4. Here, the LSC, YSZ and the YSZ/NiO layers are slightly thicker while the CGO diffusion barrier seems to be somewhat thinner. However, the boundaries especially between the electrolyte and the diffusion barrier cannot clearly be differentiated in Figure 52 (b). For unknown reasons, the polishing quality of Cell 7 is worse than for all other cells which is indicated by deep scratches in Figure 52. The bright spots are identified as gold by EDX which could be an impurity from the polishing papers. No further unexpected elements are detected by EDX.

Compared to the microstructure of Cell 4, coarsening owing to re-oxidation is less pronounced in the SOFC anode layer displayed in Figure 52 (a). Therefore, it can be said that the anode support of Cell 7 only partially re-oxidised, although the colour of the support has changed completely from grey to green. Moreover, the layers are in good contact with each other, without exhibiting any sign of detachment. This is not surprising since the cell showed high performance and low ASR over the entire testing period.

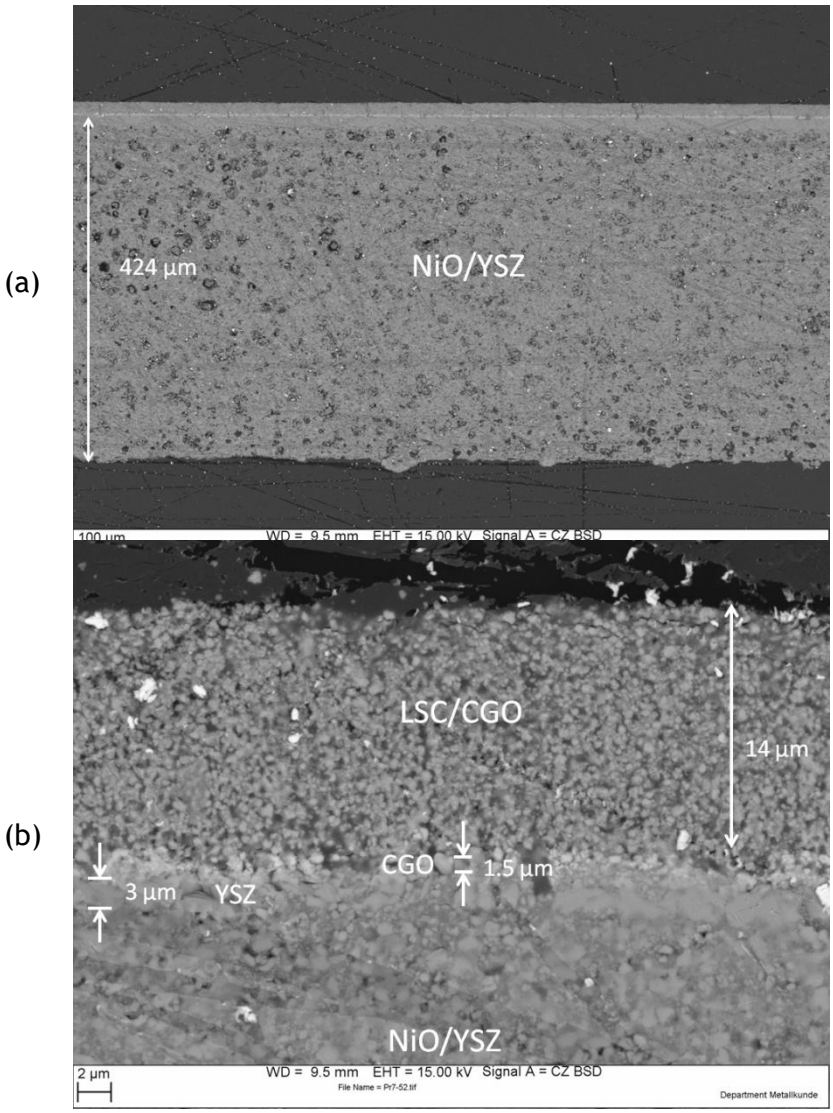

Figure 52: SEM-BSE images of a cross section of Cell 7 showing (a) the whole cell, (b) a magnified region with cathode, diffusion barrier and electrolyte layers.

4.10 Cell 8 (LCF82)

The test results of Cell 5 were influenced by high H_2 diffusion through the anode layer which caused a low OCV. In order to examine how hydrogen diffusion affects the performance for this cell type with LCF82 cathode, another similar cell (denoted as Cell 8 in the text below) is mounted with the SOFC anode side up in the *ProboStat*. The description of the fresh cell is found in section 4.7.1.

4.10.1 Test procedure

Cell 8 was mounted with the fuel electrode side up in the *ProboStat*. As for all cells mounted with the fuel electrode side up, a thin-walled alumina tube was used in place of the bent silica tube to prevent Si-poisoning of the cell. After assembling, the cell was heated up with a ramp rate of 1 K/min to 1000 °C. The cell was gas-tight at this temperature both from the inside out and from the outside in. Therefore, it was cooled down to the testing temperature of 800 °C with 2.5 K/min. The reduction process of the fuel electrode was realised in the same way as with Cell 7, applying the same reduction steps as displayed in Table 6. After five hours, the reduction was completed at an OCV of 1.09 V which is less than the OCV obtained for LSC button cells, but still 180 mV higher than the OCV of Cell 5 after the anode reduction. For all tests performed in humid atmospheres, the heating cord is used with a control temperature of 250 °C at the surface.

4.10.2 Results

The aim of these tests was to determine the effect of different humidity levels on the ASR and the performance of the cell in SOFC and SOEC operation. The testing temperature was set at 800 °C for all measurements with Cell 8, supplying a 20% O_2/Ar flow of 25 ml_n/min throughout all tests recorded. For different H_2O contents, the same mass flows of H_2 and H_2O in the fuel feed as for Cell 7 were supplied to the cell (see Table 7).

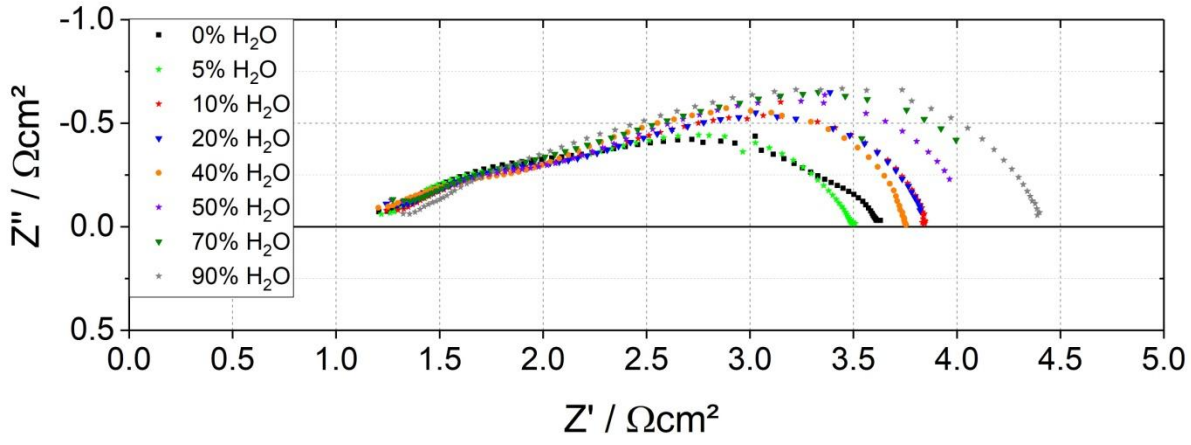

Figure 53: Impedance spectra of Cell 8 at 800°C at different H_2O contents.

The impedance pattern in Figure 53 reveals a high total ASR of the button cell at every humidity level. Particularly noticeable is the very high series resistance R_s which seems to be independent from the water content on the fuel side. Moreover, a slight offset occurs at high frequencies on the y-axis after subtracting the inductive part although the inductivity calculated from the curve fit is in the expected value range. In the previous test series, there was a clear tendency that the polarisation resistance R_p decreases with higher water partial pressure. In contrast, R_p of Cell 8 generally increases with higher humidity, although the spectra at 5% and 40% H_2O do not follow this trend.

Figure 54 displays the I-U characteristics at different humidity levels for Cell 8. Taking into account the higher OCV, the SOFC performance in dry H_2 is relatively similar to Cell 5. The only difference is that here the characteristics exhibit an upwards curved shape while Cell 5 exposes a downwards curved shape. The slopes get steeper with increasing water content which corresponds to the increasing R_p depicted in Figure 53. It is most likely that degradation already affects the cell performance as overlapping of the curves appears in SOEC operation. The overall performance of the cell is worse compared to the cells tested with LSM and LSC cathodes as the maximum current densities are much lower.

It is also striking that the OCV gets closer to the Nernst voltage with rising H_2O content. While it is significantly lower in dry H_2, the OCV nearly perfectly corresponds to the Nernst voltage at higher H_2O content. A plausible explanation therefore is the lower H_2 feed at higher moisture, hence there is less H_2 diffusion through the anode layer to the air side. Moreover, OCV-oscillation still occurs at low humidity levels, which explains the non-perfect curve shape of measurement at 20% H_2O in Figure 54.

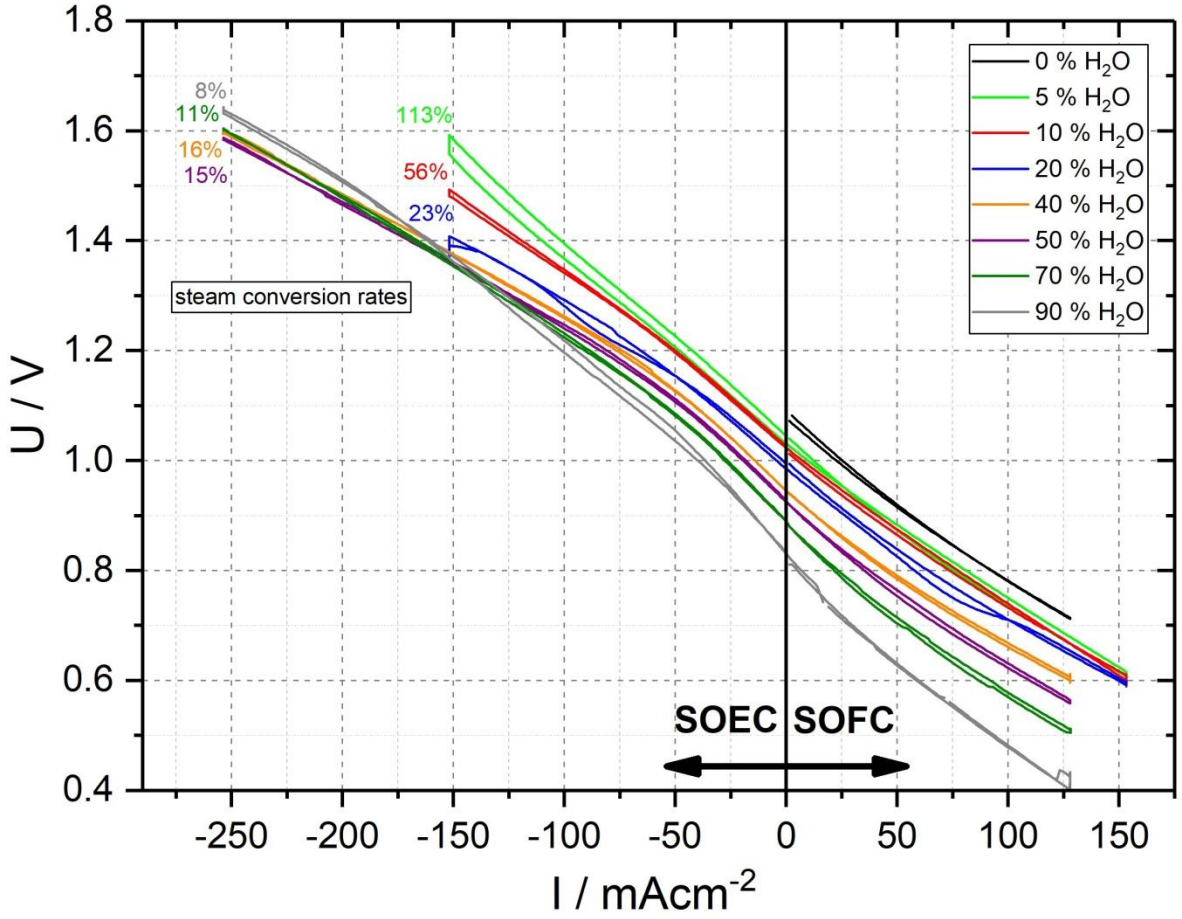

Figure 54: Current-voltage characteristics of Cell 8 at 800 °C at different H_2O contents in SOEC and SOFC operation mode.

Both the anode and the cathode of Cell 8 are shown in Figure 55 after disassembling. The cathode has maintained its black colour and has not faded to grey. Small spots of the cathode layer have sintered to the platinum electrode and were thus detached from the surface of the button cell during disassembly. The grey anode layer is fully reduced and does not exhibit any cracks or other damages.

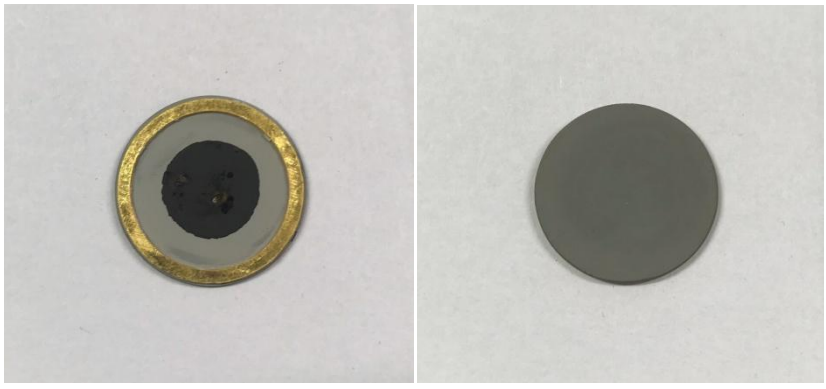

Figure 55: SOFC cathode (left) and fully reduced anode (right) of Cell 8 after disassembling.

4.10.3 Scanning electron microscopy (SEM)

SEM analysis of the button cell with fully reduced fuel electrode was performed to compare the microstructure of the button cells with LCF82 air electrode which were tested with the air and fuel electrode side up, respectively. The thicknesses of the four identified layers approximately correspond to the results of Cell 5:

(1) Porous LCF82 cathode, thickness 21 µm
(2) Thin porous CGO diffusion barrier, thickness 4 µm
(3) Densely sintered YSZ electrolyte, thickness 6 µm
(4) Porous Ni/YSZ anode substrate, thickness 529 µm

The layer characteristics of Cell 8 do not deviate from the ones of Cell 5 with respect to microstructure and porosity. The only significant difference is that no delamination of the SOFC cathode appears, as it can be seen in Figure 56. It is likely that the improved operating procedure reduced high mechanical stresses between the cell layers and thus prevented delamination. Compared to the LCF82 layer of Cell 5, the air electrode layer of Cell 8 is thicker although the screen-printing process was not changed and the same screen (55T) was used. The layer thickness varies slightly over the diameter of the cell but it is more uniform than the LCF82 layer of Cell 5. Moreover, the Ni/YSZ anode support with YSZ electrolyte and CGO diffusion barrier of Cell 5 and Cell 8 are equivalent. Only the expected elements are detected by EDX in all layers.

(a)

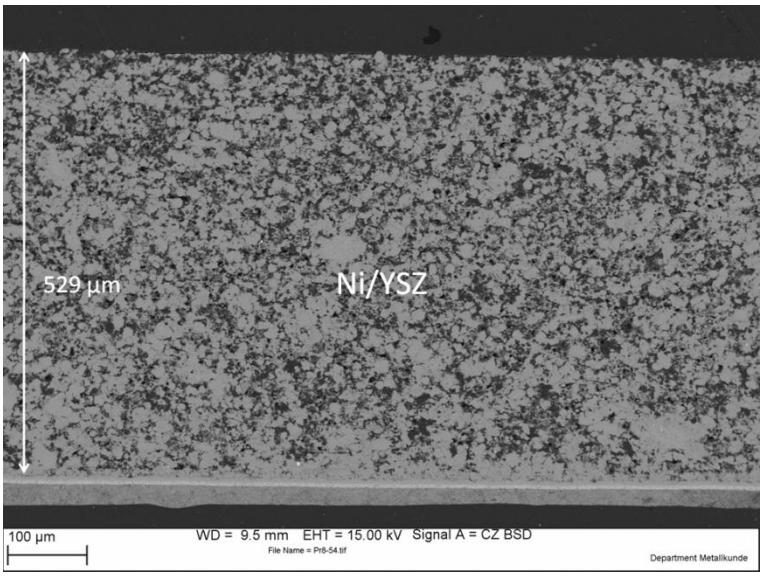

(b)

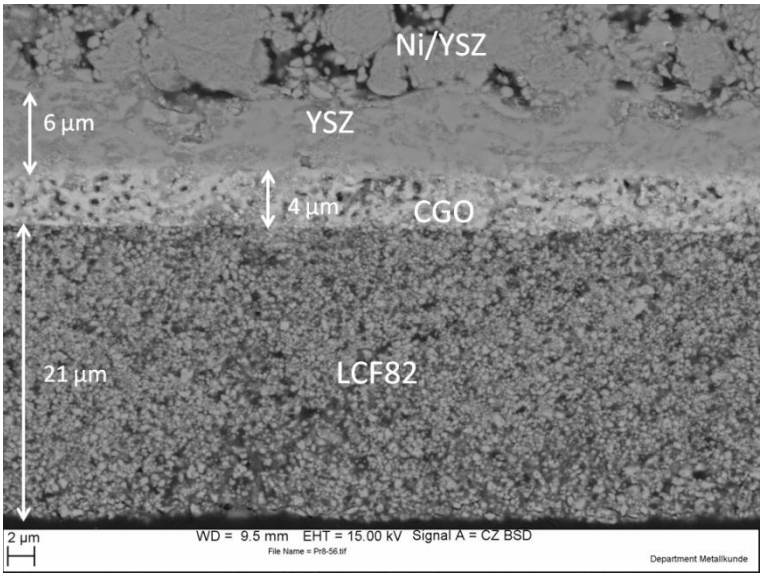

Figure 56: SEM-BSE images of a cross section of Cell 8 showing (a) the whole cell, (b) a magnified region with cathode, diffusion barrier and electrolyte layers.

4.11 Cell 9 (LCF82)

The tests of Cell 8 at different humidity levels were carried out successfully. The results attested the low maximum achievable current densities obtained for Cell 5 owing to a high ASR of the cell. A third similar button cell with LCF82 air electrode (see description of the fresh cell in section 4.7.1) was investigated to ensure reproducibility of the test results. This is especially important for button cells with a cathode manufactured in-house to check the repeatability of the manufacturing process of the cathode material. Moreover, short-term degradation effects were examined. The button cell is denoted as Cell 9 in the text below.

4.11.1 Test procedure

The fuel cell was mounted SOFC anode side up in the *ProboStat* because the cell consists of the same anode substrate that had revealed strong H_2 diffusion through the Ni/YSZ anode support to the air side in the previous tests. A thin-walled alumina tube was again used as riser for the humid fuel feed. The cell was heated up with a ramp rate of 1.2 K/min to 1000 °C. As the gas-tightness test did not reveal gas leakages, the cell was cooled down with 2.5 K/min to the testing temperature of 800 °C. The reduction process was carried out by increasing the H_2 content stepwise in the same way as for Cell 7 and Cell 8 (see Table 6). For Cell 9 the total reduction time until the OCV (1.08 V) was constant in pure H_2 was four hours. The use of the heating cord (surface control temperature 250 °C) prevented water condensation at the gas outlet for every gas humidity. To set different H_2O contents, the same fuel feeds as displayed in Table 7 were applied.

4.11.2 Results

Compared to the EIS-results of Cell 8 (Figure 53), the impedance spectra of Cell 9 (Figure 57) at different humidity levels exhibit higher R_s and lower R_{pol}. Similarities between the two cells (mounted with the LCF82 air electrode side up) are the changes in the spectra at lower frequencies for different H_2O contents. In the medium and high frequency range, the spectra do not strongly differ from each other, except for the spectrum recorded at 90% H_2O, which shows higher polarisation resistance. This presumably results from degradation and not from the higher humidity, as H_2O supply was consecutively increased with time and thus the measurements at higher H_2O contents were performed last.

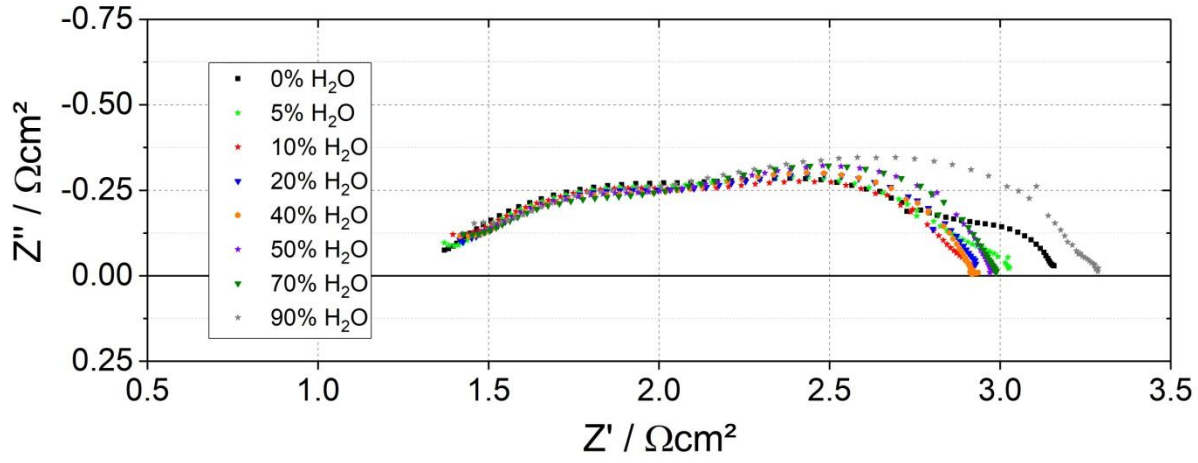

Figure 57: Impedance spectra of Cell 9 at 800°C at different H_2O contents.

Figure 58 presents the I-U characteristics of Cell 9 which are quite similar to the ones of Cell 8 (Figure 54) regarding the OCV at the different humidity levels. According to the lower total ASR shown in Figure 57, the slope of the curves is lower and thus the cell performance of Cell 9 is a little better. At 90% H_2O, a sudden change occurs during the measurement, which is of unknown origin since condensation can be excluded. With regard to the results of Cell 8 and Cell 9, no major deviations are observed, albeit Cell 9 exhibits better performance and lower ASR. The results can therefore be considered as reproducible.

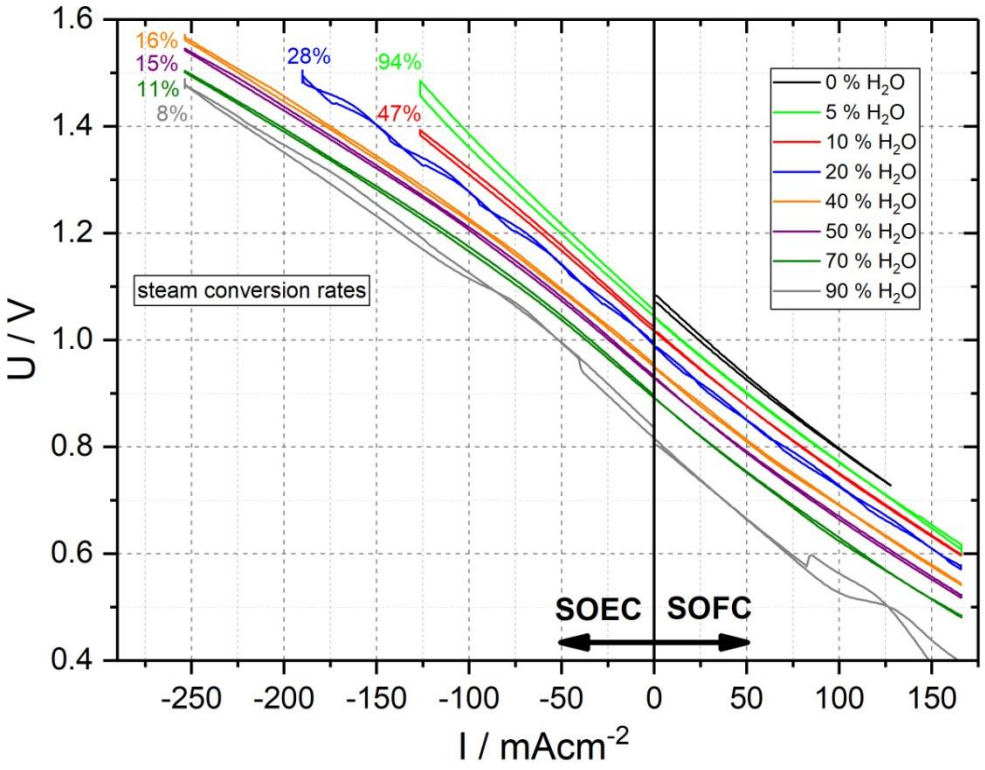

Figure 58: Current-voltage characteristics of Cell 9 at 800 °C at different H_2O contents in SOEC and SOFC operation mode.

After measurements for all humidity levels were performed, the fuel electrode of the cell was exposed to pure H_2 for 100 hours. Initially, tests were carried out in pure H_2 (measurements on days 1-7). Then, the H_2O content was increased to 90% and kept constant for 3 days. Every day, an impedance spectrum and an I-U curve were recorded (measurements on day 7,8 and 9) to observe the increasing degradation of the cell induced by high humidity in the fuel feed. Before cooling down, the H_2O feed was stopped and another measurement (day 9) in pure H_2 was recorded.

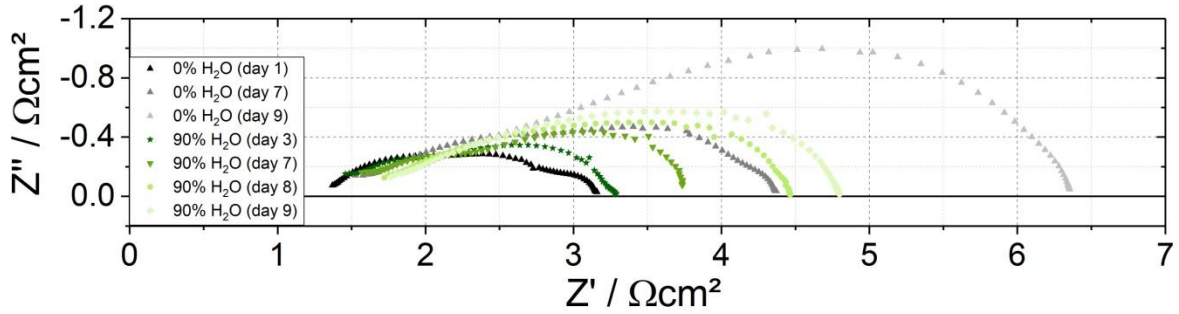

Figure 59: Impedance spectra of Cell 9 at 800°C showing degradation.

Figure 59 shows the increase of the ASR with time when the cell is exposed to a high H_2O content of 90%. Considering the green spectra, which depict the results obtained in 90% H_2O, it is clear that R_p increases significantly, while R_s rises only slightly. Similarly, the ASR increases strongly with time in pure H_2. Here the results for day 1 and day 7 show the spectrum obtained in pure H_2 before and after taking measurements at all different humidity levels which are displayed in Figure 57 and Figure 58. The spectrum in light grey dots (day 9, 0% H_2O) illustrates the deteriorating effect of high humidity on the cell, since the ASR increases tremendously compared to the value before testing in humid atmosphere. The I-U characteristics (Figure 60) underline the negative effect of high humidity. The performance clearly decreases with time, both in 90% H_2O and in pure H_2 on the fuel side.

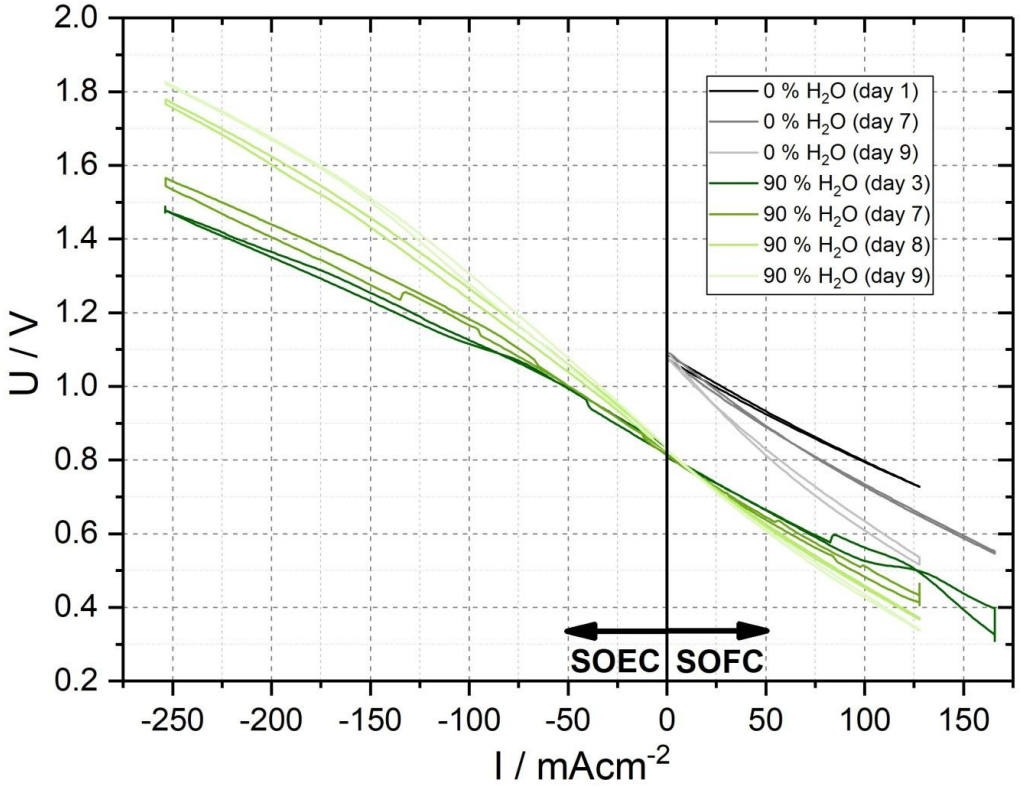

Figure 60: Current-voltage characteristics of Cell 9 at 800 °C showing degradation.

Figure 61 shows the air and the fuel electrode after disassembling. The gold gasket is firmly sintered to the cell. The anode substrate is fully reduced which is indicated by the grey colour of the entire area of the cell. Cell 9 exhibits the same external characteristics as Cell 8 after testing. With the naked eye, no negative effects of the longer exposure in 90% water are recognizable.

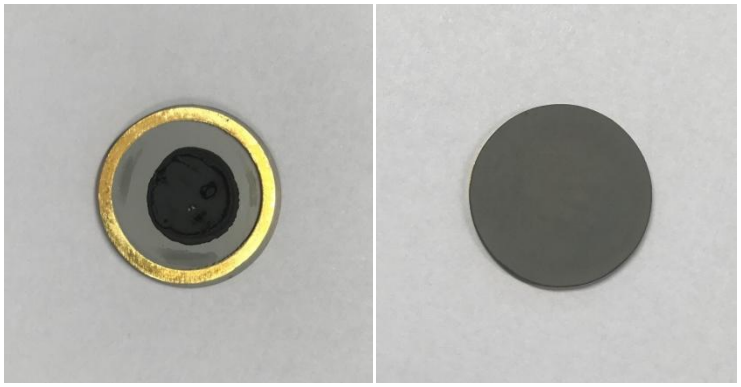

Figure 61: SOFC cathode (left) and fully reduced anode (right) of Cell 9 after disassembling.

4.11.3 Scanning electron microscopy (SEM)

Like the other button cells with LCF82 air electrode, Cell 9 was examined with SEM in order to determine the different layers of the cell. Since the button cell tested is the same model as Cell 5 and Cell 8, the same four layers can be identified in Figure 62:

(1) Porous LCF82 cathode, thickness 40 µm
(2) Thin porous CGO diffusion barrier, thickness 4 µm
(3) Densely sintered YSZ electrolyte, thickness 6 µm
(4) Porous Ni/YSZ anode substrate, thickness 525 µm

It is striking that here the SOFC cathode layer is much thicker compared to the previously analysed LCF82 cells even though it was screen-printed using the same screen (T55) and sintered in the exact same manner. These significant deviations regarding the layer thickness can only be explained with different handling during screen-printing. With respect to the microstructure and the porosity of the different layers, Cell 9 resembles Cell 5 and Cell 8.

Unlike Cell 8, the LCF82 layer appears to be slightly delaminated. Since the cell was exposed to 90% H_2O over a longer period of time and exhibited deteriorating performance with time, it seems obvious that the delamination was caused by long time exposure to a highly humid gas feed. The detachment of the air electrode can thus explain the high degradation observed in 90% H_2O (see Figure 59 and Figure 60). A subsequent EDX analysis validates the presence of the expected elements without detecting any impurities in any cell layer.

(a)

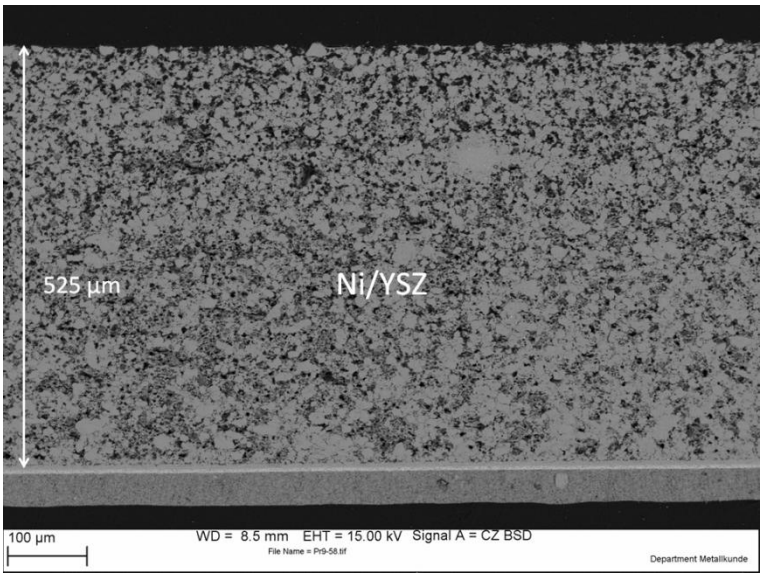

(b)

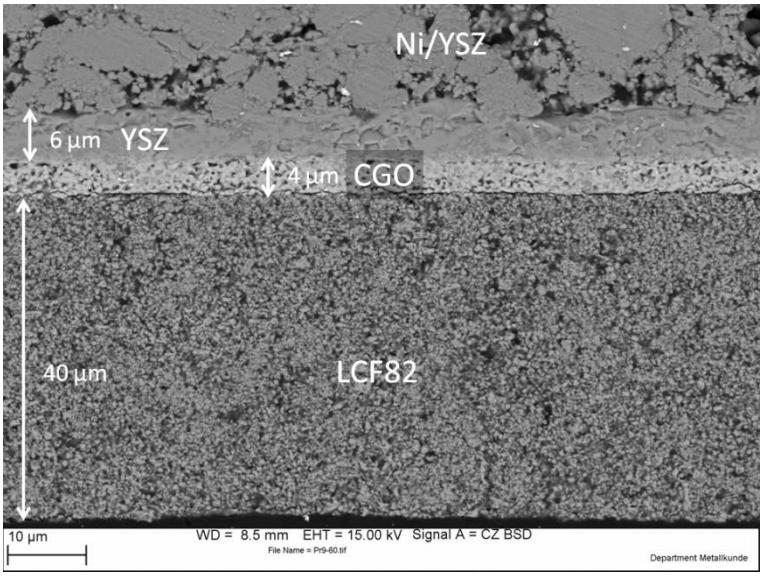

Figure 62: SEM-BSE images of a cross section of Cell 9 showing (a) the whole cell, (b) a magnified region with cathode, diffusion barrier and electrolyte layers.

4.12 Cell comparison

To sum up the research outcome presented in chapter 4, the results of all tested cells are compared. The impedance spectra in Figure 63 illustrate significant differences between the cells. With the first button cell tests performed with LSM air electrode, the testing procedure was not optimised yet, which has to be considered when assessing the results.

It is remarkable, that the series resistance R_s is significantly higher for all cells with LCF82 air electrode than for the commercial cells of Fuel Cell Materials (LSM, LSC). As the material properties of LCF82 are considered to be promising due to high kinetic parameters and good ionic conductivity [33], it is supposed that the interface between electrolyte and cathode is the reason for the poor performance of the cells. Comparing the results of the same cell types separately, it can be noticed that the shape of the curves is quite similar for LSM, LSC and LCF82 cells (except Cell 5). LSC cells exhibit the lowest polarisation resistances and thus the lowest ASR. However, the ASR changes noticeably at similar test conditions for all three cathode materials. It is difficult to identify whether the *ProboStat* setup or the button cells themselves have caused the deviations between the measuring results. Assessment of the characteristics of the impedance spectrum of Cell 5, must always take into account strong hydrogen diffusion through the fuel electrode layer.

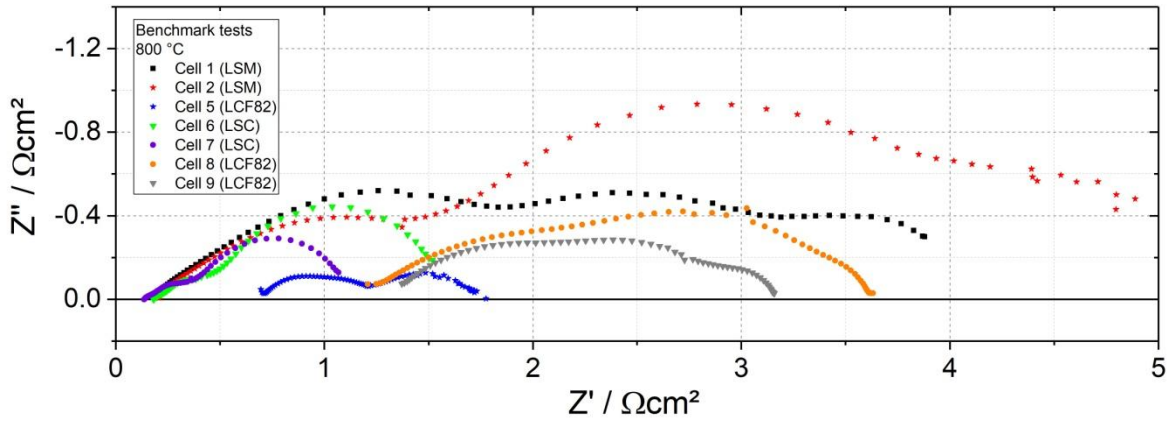

Figure 63: Impedance spectra of all tested cells at 800°C in pure H_2.

In SOFC operation, LSC cells show excellent performance and differ considerably from all other cells, since the current densities at 0.75 V achieved at 800 °C are more than four times higher than for LSM and LCF82 cells. Figure 64 displays the good performance of LSC cells compared to the others. Moreover, it is apparent that the OCV is lower for LCF82 cells, which strengthens the assumption of problems occurring with the cathode-diffusion layer-electrolyte interface.

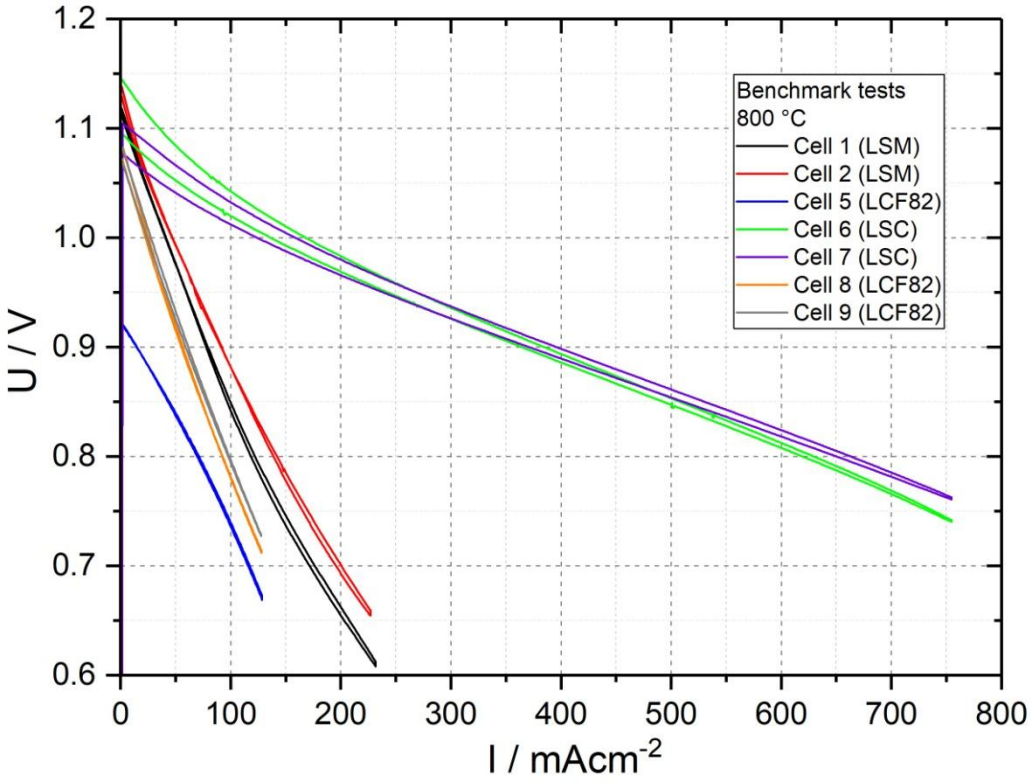

Figure 64: Current-voltage characteristics of all tested cells at 800 °C in pure H_2 (SOFC mode).

5 Summary and conclusions

Within this thesis, the installation and start-up of a testing system for reproducible electrochemical measurements on button cells with ceramic electrolytes in SOFC and SOEC operation was carried out. For this purpose, an experimental setup with the so-called *ProboStat* unit as centrepiece was developed and optimised under consideration of the gained know-how and the achieved results.

Chapter 2 gives an overview of the most important theoretical concepts with respect to SOFCs and SOECs based on a literature survey. After explaining the basic operational principle of these electrochemical and electrolytic cells, a short review of the state-of-the-art materials for SOFC/SOEC applications is given. Moreover, the theory section provides an elementary explanation of electrochemical impedance spectroscopy which is a powerful, but also very challenging, tool for the characterisation and analysis of electrochemical processes.

The devised experimental setup is described in detail in chapter 3 including preliminary investigations regarding the gas-tightness of the cell, which turned out to be one of the main problems at the beginning of the cell tests. Additionally, different approaches for proper thermal insulation and supplementary heating, in order to avoid water condensation at the cool spots of the *ProboStat*, are tested. Precise studies helped to find suitable solutions for these issues, thus the developed testing construction is ready to be used for future investigations at the Chair of Physical Chemistry (MUL).

During this work, tests of nine SOFC anode-supported button cells with different types of electrode materials are performed. A comprehensive description of the testing procedure, as well as a graphical interpretation of the measurement results, is carried out in chapter 4. The two principal methods applied for the electrochemical characterisation of the button cells are electrochemical impedance spectroscopy and current-voltage characteristics. Apart from that, OCV-monitoring is another meaningful instrument to elucidate the occurring processes in the fuel cell. A large number of measurements was recorded in order to compare the cell behaviour in different gas environments with special focus on the effect of the humidity level in the fuel feed.

With regard to the analysed cells, there is a tendency that the series resistance R_s increases, while the total ASR and especially the polarisation resistance R_p decrease at higher water contents in the fuel feed for all applied air electrode materials. I-U curves demonstrate that the cell performance decreases at higher humidity levels, which is on the one hand due to the lower OCV according to the Nernst equation, and on the other hand to stronger degradation at higher moisture contents. As expected, the measurement results show that both the series resistance R_s and the polarisation resistance R_p increase with decreasing temperatures.

Moreover, the three studied air electrode materials (LSM, LSC, LCF82) are compared with each other throughout the text. In general, it was found that the performance of cells with

the new air electrode material LCF82 is lower than that of the button cells with LSM and LSC air electrodes. The high ASR of LCF82-based cells results in low maximum current densities in both SOFC and SOEC operation. This is somewhat surprising since previous investigations with respect to the basic material properties of LCF82 attest high suitability for the use as air electrode material. As expected, cells with LSC air electrodes show the best performance exhibiting low ASRs at all humidity levels operating as fuel cell as well as electrolyser cell.

Finally, post-test analysis of the button cells using SEM was performed in order to determine the thicknesses and the microstructure of the different layers. The results indicate that prolonged exposure to highly humidified fuel feeds might increase the risk of delamination, which is a fatal damage mode for fuel cells and electrolysers.

5.1 Outlook

The developed setup is ready to use for future investigations especially for anode-supported solid electrolyte fuel cells. Investigations of very thin electrolyte-supported fuel cells (ESCs) seem in principle possible, but also pose a particular challenge with regard to cell mounting. First attempts to mount ESCs failed because the fragile button cells could not withstand the applied clamping force. For this reason, the idea now is to design a mounting jig which enables a more controlled installation of the cell with an enhanced distribution of the effective forces.

Although the evolved experimental setup seems well-engineered, it is always advisable to implement further developments. It is conceivable to upgrade the system with additional appropriate technical devices, such as a gas analysing system which consists of a gas chromatograph and a detector. This would help to detect gas-leakages and could provide more detailed information about the conversion rates of the supplied gases in the *ProboStat* unit.

6 References

[1] United Nations Framework Convention on Climate Change, Paris Agreement: essential elements, URL: https://unfccc.int/process-and-meetings/the-paris-agreement/the-paris-agreement (retrieved on 10.09.2018).

[2] P.P. Edwards, V.L. Kuznetsov, W.I.F. David, N.P. Brandon, Hydrogen and fuel cells: Towards a sustainable energy future, Energy Policy 36 (2008) 4356–4362.

[3] K. Huang, J.B. Goodenough, Solid oxide fuel cell technology: Principles, performance and operations, Woodhead Pub; CRC Press, Cambridge, Boca Raton, 2009.

[4] J. Karl, Dezentrale Energiesysteme: Neue Technologien im liberalisierten Energiemarkt, 3rd ed., Oldenbourg, München, 2012.

[5] J. Larminie, A. Dicks, Fuel cell systems explained, 2nd ed., Wiley, Chichester, 2003.

[6] R. Zahoransky (Ed.), Energietechnik: Systeme zur Energieumwandlung, 6th ed., Springer Vieweg, Wiesbaden, 2013.

[7] P. Kurzweil, Brennstoffzellentechnik: Grundlagen, Komponenten, Systeme, Anwendungen, 2nd ed., Springer Vieweg, Wiesbaden, 2013.

[8] J.T.S. Irvine, P. Conner, Solid oxide fuels cells: Facts and figures, Springer, Berlin, 2013.

[9] I. Dincer, C.O. Colpan, Introduction to Stationary Fuel Cells, in: M. Ni, T.S. Zhao (Eds.), Solid Oxide Fuel Cells, Royal Society of Chemistry, Cambridge, 2013, pp. 1–25.

[10] G. Kaur, Solid Oxide Fuel Cell Components: Interfacial Compatibility of SOFC Glass Seals, 1st ed., Springer International Publishing, Cham, 2016.

[11] W. Sitte, Vorlesungsunterlagen zu Elektrochemische Energiespeicherung und -umwandlung, 2015.

[12] S.C. Singhal, K. Kendall (Eds.), High-temperature solid oxide fuel cells: Fundamentals, design and applications, Elsevier Advanced Technology, Oxford, 2003.

[13] M. Boaro, A.S. Aricò (Eds.), Advances in medium and high temperature solid oxide fuel cell technology, Springer, Cham, 2017.

[14] O. Schmidt, A. Gambhir, I. Staffell, A. Hawkes, J. Nelson, S. Few, Future cost and performance of water electrolysis: An expert elicitation study, International Journal of Hydrogen Energy 42 (2017) 30470–30492.

[15] J.B. Hansen, Solid oxide electrolysis - a key enabling technology for sustainable energy scenarios, Faraday discussions 182 (2015) 9–48.

[16] J.P. Stempien, Sunc Qiang, S.H. Chan, Solid Oxide Electrolyzer Cell Modeling: A Review, Journal of Power Technologies 93 (2013) 216–246.

[17] M. Kotisaari, O. Thomann, D. Montinaro, J. Kiviaho, Evaluation of a SOE Stack for Hydrogen and Syngas Production: a Performance and Durability Analysis, Fuel Cells 17 (2017) 571–580.

[18] C. Graves, S.D. Ebbesen, M. Mogensen, Co-electrolysis of CO_2 and H_2O in solid oxide cells: Performance and durability, Solid State Ionics 192 (2011) 398–403.

[19] J. Garche (Ed.), Encyclopedia of electrochemical power sources, Elsevier Acad. Press, Amsterdam, 2009.

[20] J.W. Fergus, Electrolytes for solid oxide fuel cells, Journal of Power Sources 162 (2006) 30–40.

[21] N. Mahato, A. Banerjee, A. Gupta, S. Omar, K. Balani, Progress in material selection for solid oxide fuel cell technology: A review, Progress in Materials Science 72 (2015) 141–337.

[22] T. Talebi, M.H. Sarrafi, M. Haji, B. Raissi, A. Maghsoudipour, Investigation on microstructures of NiO–YSZ composite and Ni–YSZ cermet for SOFCs, International Journal of Hydrogen Energy 35 (2010) 9440–9447.

[23] A. Sanson, P. Pinasco, E. Roncari, Influence of pore formers on slurry composition and microstructure of tape cast supporting anodes for SOFCs, Journal of the European Ceramic Society 28 (2008) 1221–1226.

[24] S.P. Jiang, S.H. Chan, A review of anode materials development in solid oxide fuel cells, Journal of Materials Science 39 (2004) 4405–4439.

[25] J. Richter, P. Holtappels, T. Graule, T. Nakamura, L.J. Gauckler, Materials design for perovskite SOFC cathodes, Monatsh Chem 140 (2009) 985–999.

[26] C. Yunphuttha, S. Porntheeraphat, A. Wongchaisuwat, S. Tangbunsuk, D.W.M. Marr, P. Viravathana, Characterization of $La_{1-x}Sr_xMnO_3$ perovskite catalysts for hydrogen peroxide reduction, Physical chemistry chemical physics PCCP 18 (2016) 16786–16793.

[27] C. Sun, R. Hui, J. Roller, Cathode materials for solid oxide fuel cells: a review, J Solid State Electrochem 14 (2010) 1125–1144.

[28] B. Ahmed, S.-B. Lee, R.-H. Song, J.-W. Lee, T.-H. Lim, S.-J. Park, Development of novel LSM/GDC composite and electrochemical characterization of LSM/GDC based cathode-supported direct carbon fuel cells, J Solid State Electrochem 18 (2014) 435–443.

[29] H.J. Ko, J.-h. Myung, S.-H. Hyun, J.S. Chung, Synthesis of LSM–YSZ–GDC dual composite SOFC cathodes for high-performance power-generation systems, J Appl Electrochem 42 (2012) 209–215.

[30] S.J. Skinner, Recent advances in Perovskite-type materials for solid oxide fuel cell cathodes, International Journal of Inorganic Materials 3 (2001) 113–121.

[31] R. Knibbe, J. Hjelm, M. Menon, N. Pryds, M. Søgaard, H.J. Wang, K. Neufeld, Cathode-Electrolyte Interfaces with CGO Barrier Layers in SOFC, Journal of the American Ceramic Society 93 (2010) 2877–2883.

[32] R.D. Shannon, Revised effective ionic radii and systematic studies of interatomic distances in halides and chalcogenides, Acta Crystallographica A 32 (1976) 751–767.

[33] C. Berger, E. Bucher, A. Windischbacher, A.D. Boese, W. Sitte, Strontium-free rare earth perovskite ferrites with fast oxygen exchange kinetics: Experiment and theory, Journal of Solid State Chemistry 259 (2018) 57–66.

[34] Q.-A. Huang, R. Hui, B. Wang, J. Zhang, A review of AC impedance modeling and validation in SOFC diagnosis, Electrochimica Acta 52 (2007) 8144–8164.

[35] J.R. Macdonald (Ed.), Impedance spectroscopy: Emphasizing solid materials and systems, Wiley, New York, 1987.

[36] C. Gabrielli, Identification of Electrochemical Processes by Frequency: Technical Report No004/83, 1998.

[37] A. Leonide, SOFC modelling and parameter identification by means of impedance spectroscopy. dissertation, Hannover, Karlsruhe, 2010.

[38] Lehrstuhl für Physikalische Chemie Leoben, Tutorial: Impedanzspektroskopie, 2016.

[39] R. Barfod, M. Mogensen, T. Klemenso, A. Hagen, Y.-L. Liu, P. Vang Hendriksen, Detailed Characterization of Anode-Supported SOFCs by Impedance Spectroscopy, J. Electrochem. Soc. 154 (2007) B371-B378.

[40] T. Herbst, NorECs AS ProboStat A-7: Inbetriebnahme und Durchführung diverser Versuche an Festoxidbrennstoffzellen, 2016.

[41] NorECs Norwegian Electro Ceramics AS, ProboStat™ Base Unit Heating Systems Manual, Oslo, 2017.

[42] NorECs Norwegian Electro Ceramics AS, What sealing material can be used?, URL: http://www.norecs.com/index.php?page=148&faq=36 (retrieved on 31.08.2018).

[43] NorECs Norwegian Electro Ceramics AS, ProboStat™ Manual, Oslo, 2013.

[44] N.M. Tikekar, T.J. Armstrong, A.V. Virkar, Reduction and Reoxidation Kinetics of Nickel-Based SOFC Anodes, J. Electrochem. Soc. 153 (2006) A654.

[45] D. Fouquet, A.C. Müller, A. Weber, E. Ivers-Tiffée, Kinetics of oxidation and reduction of Ni/YSZ cermets, Ionics 9 (2003) 103–108.

[46] J. Malzbender, E. Wessel, R. Steinbrech, Reduction and re-oxidation of anodes for solid oxide fuel cells, Solid State Ionics 176 (2005) 2201–2203.

[47] NorECs Norwegian Electro Ceramics AS, HumiStat Manual, Oslo.

[48] Novocontrol Technologies, Alpha-A High Resolution Dielectric, Conductivity, Impedance and Gein Phase Modular Measurement System: User's Manual, 2012.

[49] T. Tsai, Effect of LSM-YSZ cathode on thin-electrolyte solid oxide fuel cell performance, Solid State Ionics 93 (1997) 207–217.

[50] Fuel Cell Materials, Anode Supported Button Cell, URL: https://fuelcellmaterials.com/products/cells/anode-supported-button-cell (retrieved on 03.07.2018).

[51] J.H. Yu, G.W. Park, S. Lee, S.K. Woo, Microstructural effects on the electrical and mechanical properties of Ni–YSZ cermet for SOFC anode, Journal of Power Sources 163 (2007) 926–932.

[52] Fuel Cell Materials, Anode Electrolyte Button Bi-Layer, URL: https://fuelcellmaterials.com/products/equipment/anode-electrolyte-button-bi-layer (retrieved on 09.07.2018).

[53] N. Schrödl, E. Bucher, A. Egger, P. Kreiml, C. Teichert, T. Höschen, W. Sitte, Long-term stability of the IT-SOFC cathode materials $La_{0.6}Sr_{0.4}CoO_{3-\delta}$ and $La_2NiO_{4+\delta}$ against combined chromium and silicon poisoning, Solid State Ionics 276 (2015) 62–71.

[54] M. Viitanen, R. v. Welzenis, H. Brongersma, F. van Berkel, Silica poisoning of oxygen membranes, Solid State Ionics 150 (2002) 223–228.

7 Appendix

7.1 R_s, R_p and ASR_{total}

7.1.1 Cell 1 – dry H_2 vs. 20% O_2

Measurement	R_s / Ωcm²	R_p / Ωcm²	ASR_{total} / Ωcm²
750 °C (day 1)	0.26	5.37	5.63
750 °C (day 5)	0.27	7.35	7.62
800 °C (day 1)	0.19	3.69	3.88
800 °C (day 6)	0.23	3.58	3.81
850 °C (day 1)	0.15	2.52	2.67
850 °C (day 6)	0.20	2.38	2.58

7.1.2 Cell 2 - 800 °C

Measurement	R_s / Ωcm²	R_p / Ωcm²	ASR_{total} / Ωcm²
0% H_2O	0.20	4.68	4.88
5% H_2O	0.35	2.57	2.92
10% H_2O	0.32	2.18	2.50
20% H_2O	0.33	2.13	2.46
40% H_2O	0.37	2.08	2.45

7.1.3 Cell 2 - 800 °C, degradation

Measurement	R_s / Ωcm²	R_p / Ωcm²	ASR_{total} / Ωcm²
0% H_2O	0.20	4.68	4.88
0% H_2O after 14 days	0.27	5.55	5.82
0% H_2O after 21 days	0.22	6.59	6.81
5% H_2O	0.35	2.57	2.92
5% H_2O after 13 days	0.29	3.07	3.36

7.1.4 Cell 5

Measurement	R_s / Ωcm²	R_p / Ωcm²	ASR_{total} / Ωcm²
800 °C, dry H_2 (day 1)	0.72	1.06	1.78
800 °C, dry H_2 (day 6)	0.95	1.07	2.02
800 °C, dry H_2 (day 8)	0.99	7.79	8.78
750 °C, dry H_2 (day 1)	0.98	1.24	2.22
750 °C, dry H_2 (day 6)	1.27	1.60	2.87
700 °C, dry H_2 (day 1)	1.38	1.92	3.30
700 °C, dry H_2 (day 6)	2.04	2.28	4.32
800 °C, 10% H_2O (day 7)	0.74	0.77	1.51
800 °C, 10% H_2O (day 8)	0.91	7.52	8.43

7.1.5 Cell 6 - dry H_2 vs. 20% O_2

Measurement	R_s / Ωcm²	R_p / Ωcm²	ASR_{total} / Ωcm²
800 °C	0.18	1.34	1.52
750 °C	0.20	1.83	2.03
700 °C	0.23	2.22	2.45
650 °C	0.29	2.77	3.06
600 °C	0.41	3.70	4.11

7.1.6 Cell 7 – 800 °C

Measurement	R_s / Ωcm²	R_p / Ωcm²	ASR_{total} / Ωcm²
0% H_2O	0.14	0.94	1.08
5% H_2O	0.16	0.30	0.46
10% H_2O	0.15	0.23	0.38
20% H_2O	0.15	0.16	0.31
40% H_2O	0.17	0.13	0.30
50% H_2O	0.18	0.17	0.35
70% H_2O	0.17	0.15	0.32
90% H_2O	0.17	0.19	0.36

7.1.7 Cell 8 – 800 °C

Measurement	R_s / Ωcm²	R_p / Ωcm²	ASR_{total} / Ωcm²
0% H_2O	1.21	2.40	3.61
5% H_2O	1.22	2.29	3.51
10% H_2O	1.24	2.60	3.84
20% H_2O	1.24	2.58	3.82
40% H_2O	1.20	2.55	3.75
50% H_2O	1.27	2.69	3.96
70% H_2O	1.27	2.73	4.00
90% H_2O	1.32	3.07	4.39

7.1.8 Cell 9 – 800 °C

Measurement	R_s / Ωcm²	R_p / Ωcm²	ASR_{total} / Ωcm²
0% H_2O	1.37	1.79	3.16
5% H_2O	1.40	1.63	3.03
10% H_2O	1.40	1.53	2.93
20% H_2O	1.42	1.51	2.93
40% H_2O	1.42	1.50	2.92
50% H_2O	1.42	1.55	2.97
70% H_2O	1.43	1.56	2.99
90% H_2O	1.46	1.82	3.28

7.1.9 Cell 9 - 800 °C, degradation

Measurement	R_s / Ωcm²	R_p / Ωcm²	ASR_{total} / Ωcm²
0% H_2O (day 1)	1.37	1.79	3.16
0% H_2O (day 7)	1.53	2.84	4.37
0% H_2O (day 9)	1.77	4.59	6.36
90% H_2O (day 3)	1.46	1.83	3.29
90% H_2O (day 7)	1.57	2.17	3.74
90% H_2O (day 8)	1.72	2.75	4.47
90% H_2O (day 9)	1.77	3.02	4.79

7.2 Nernst voltage at different gas compositions and temperatures

Gas compositions													
O_2 / vol%		20	20	20	20	20	20	20	20	20	20	20	20
H_2 / vol%		99.00	97.00	95.00	90.00	80.00	70.00	60.00	50.00	40.00	30.00	20.00	10.00
H_2O / vol%		**1.00**	**3.00**	**5.00**	**10.00**	**20.00**	**30.00**	**40.00**	**50.00**	**60.00**	**70.00**	**80.00**	**90.00**
T / °C	**E_0 / V**	**Nernst voltage / V**											
25	1.185	1.233	1.219	1.212	1.202	1.192	1.185	1.179	1.174	1.169	1.163	1.156	1.146
50	1.179	1.232	1.216	1.209	1.198	1.187	1.179	1.173	1.168	1.162	1.156	1.148	1.137
75	1.173	1.230	1.213	1.205	1.194	1.182	1.173	1.167	1.161	1.155	1.148	1.140	1.128
100	1.167	1.228	1.210	1.201	1.189	1.176	1.168	1.160	1.154	1.147	1.140	1.132	1.119
125	1.161	1.226	1.207	1.197	1.185	1.171	1.161	1.154	1.147	1.140	1.132	1.123	1.109
150	1.155	1.224	1.203	1.194	1.180	1.165	1.155	1.147	1.140	1.133	1.124	1.115	1.100
175	1.148	1.222	1.200	1.190	1.175	1.160	1.149	1.141	1.133	1.125	1.116	1.106	1.090
200	1.142	1.219	1.197	1.186	1.170	1.154	1.143	1.134	1.126	1.117	1.108	1.097	1.081
225	1.136	1.217	1.193	1.182	1.166	1.148	1.137	1.127	1.118	1.110	1.100	1.089	1.071
250	1.129	1.215	1.189	1.177	1.161	1.142	1.130	1.120	1.111	1.102	1.092	1.080	1.062
275	1.123	1.212	1.186	1.173	1.156	1.137	1.124	1.113	1.104	1.094	1.084	1.071	1.052
300	1.116	1.210	1.182	1.169	1.151	1.131	1.117	1.106	1.096	1.086	1.075	1.062	1.042
325	1.110	1.207	1.179	1.165	1.146	1.125	1.111	1.099	1.089	1.078	1.067	1.053	1.032
350	1.103	1.205	1.175	1.160	1.140	1.119	1.104	1.092	1.081	1.071	1.059	1.044	1.022
375	1.096	1.202	1.171	1.156	1.135	1.113	1.098	1.085	1.074	1.063	1.050	1.035	1.013
400	1.090	1.200	1.167	1.152	1.130	1.107	1.091	1.078	1.066	1.055	1.042	1.026	1.003
425	1.083	1.197	1.163	1.147	1.125	1.100	1.084	1.071	1.059	1.046	1.033	1.017	0.993
450	1.076	1.194	1.159	1.143	1.119	1.094	1.077	1.064	1.051	1.038	1.025	1.008	0.983
475	1.069	1.191	1.155	1.138	1.114	1.088	1.071	1.056	1.043	1.030	1.016	0.999	0.973
500	1.062	1.189	1.151	1.134	1.109	1.082	1.064	1.049	1.036	1.022	1.007	0.989	0.962
525	1.056	1.186	1.147	1.129	1.103	1.076	1.057	1.042	1.028	1.014	0.999	0.980	0.952
550	1.049	1.183	1.143	1.124	1.098	1.069	1.050	1.034	1.020	1.006	0.990	0.971	0.942
575	1.042	1.180	1.139	1.120	1.093	1.063	1.043	1.027	1.012	0.997	0.981	0.962	0.932
600	1.035	1.177	1.135	1.115	1.087	1.057	1.036	1.020	1.004	0.989	0.972	0.952	0.922
625	1.028	1.174	1.131	1.110	1.081	1.050	1.029	1.012	0.996	0.981	0.964	0.943	0.911
650	1.021	1.171	1.127	1.106	1.076	1.044	1.022	1.005	0.989	0.972	0.955	0.933	0.901
675	1.013	1.168	1.123	1.101	1.070	1.037	1.015	0.997	0.981	0.964	0.946	0.924	0.891
700	1.006	1.165	1.118	1.096	1.065	1.031	1.008	0.990	0.973	0.956	0.937	0.915	0.881
725	0.999	1.162	1.114	1.091	1.059	1.024	1.001	0.982	0.965	0.947	0.928	0.905	0.870
750	0.992	1.159	1.110	1.086	1.054	1.018	0.994	0.975	0.957	0.939	0.919	0.896	0.860
775	0.985	1.156	1.106	1.082	1.048	1.011	0.987	0.967	0.949	0.930	0.910	0.886	0.849
800	0.978	1.153	1.101	1.077	1.042	1.005	0.980	0.959	0.941	0.922	0.901	0.877	0.839
825	0.971	1.150	1.097	1.072	1.037	0.998	0.973	0.952	0.933	0.913	0.892	0.867	0.829
850	0.963	1.147	1.093	1.067	1.031	0.992	0.965	0.944	0.924	0.905	0.883	0.857	0.818
875	0.956	1.144	1.088	1.062	1.025	0.985	0.958	0.936	0.916	0.896	0.874	0.848	0.808
900	0.949	1.141	1.084	1.057	1.019	0.978	0.951	0.929	0.908	0.888	0.865	0.838	0.797
925	0.942	1.137	1.080	1.052	1.014	0.972	0.944	0.921	0.900	0.879	0.856	0.829	0.787
950	0.934	1.134	1.075	1.047	1.008	0.965	0.937	0.913	0.892	0.871	0.847	0.819	0.776
975	0.927	1.131	1.071	1.042	1.002	0.958	0.929	0.906	0.884	0.862	0.838	0.809	0.766
1000	0.920	1.128	1.066	1.037	0.996	0.952	0.922	0.898	0.876	0.853	0.829	0.800	0.755

7.3 Equipment

7.3.1 *ProboStat* measurement setup

Figure A-1: Novocontrol Alpha-A mainframe frequency analyser and Novocontrol POT/GAL 15V/10A.

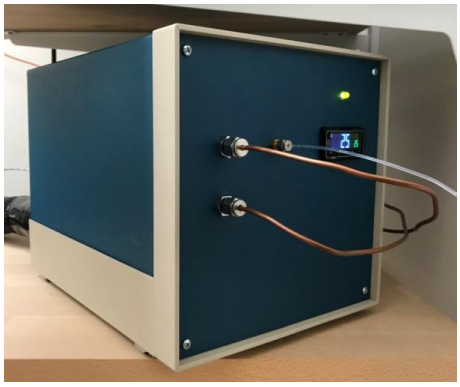

Figure A-2: NorECs HumiStat.

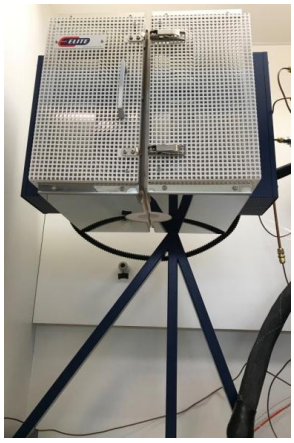

Figure A-3: Elite Vertical Single Zone Split Furnace.

Figure A-4: Elite furnace controller TSVH12/45/305/2216e.

Figure A-5: Thermocouple Digital Thermometer TME MM2000.

Figure A-6: Vögtlin V100 Flow Meter.

7.3.2 Equipment for SEM sample preparation

Figure A-7: Buehler Grinder-Polisher BETA.

Figure A-8: Buehler Precision Saw Isomet 1000.

Figure A-9: Elma Elmasonic S 30 H.

Figure A-10: Bal-Tec Med 020 high vacuum coating system.

7.3.3 Additional devices

Figure A-11: Bruker 8D Advanced X-ray diffractometer.

Figure A-12: Medlin Naber N3R furnace.

Figure A-13: Specac Manual Hydraulic Press (25 tons).